creative commons
COMMONS DEED

저작자표시-비영리-변경금지 2.0 대한민국

이용자는 아래의 조건을 따르는 경우에 한하여 자유롭게

- 이 저작물을 복제, 배포, 전송, 전시, 공연 및 방송할 수 있습니다.

다음과 같은 조건을 따라야 합니다:

저작자표시. 귀하는 원저작자를 표시하여야 합니다.

비영리. 귀하는 이 저작물을 영리 목적으로 이용할 수 없습니다.

변경금지. 귀하는 이 저작물을 개작, 변형 또는 가공할 수 없습니다.

- 귀하는, 이 저작물의 재이용이나 배포의 경우, 이 저작물에 적용된 이용허락조건을 명확하게 나타내어야 합니다.
- 저작권자로부터 별도의 허가를 받으면 이러한 조건들은 적용되지 않습니다.

저작권법에 따른 이용자의 권리는 위의 내용에 의하여 영향을 받지 않습니다.

이것은 이용허락규약(Legal Code)을 이해하기 쉽게 요약한 것입니다.

Disclaimer

dCollection

이학박사 학위논문

Radio and Infrared Studies of Supernova Remnants Interacting with Molecular Clouds

전파 및 적외선을 이용한 분자운과 상호작용하는 초신성 잔해의 연구

2015년 08월

서울대학교 대학원
물리천문학부 천문학전공
정 일 교

Radio and Infrared Studies of Supernova Remnants Interacting with Molecular Clouds

전파 및 적외선을 이용한 분자운과 상호작용하는 초신성 잔해의 연구

지도교수 구 본 철

이 논문을 이학박사 학위논문으로 제출함

2015년 04월

서울대학교 대학원

물리천문학부 천문학전공

정 일 교

정 일 교의 이학박사 학위논문을 인준함

2015년 06월

위 원 장 _____

부 위 원 장 _____

위 원 _____

위 원 _____

위 원 _____

Radio and Infrared Studies of Supernova Remnants Interacting with Molecular Clouds

by

Il-Gyo Jeong
(igjeong@astro.snu.ac.kr)

A dissertation submitted in partial fulfillment of the requirements for the degree of

Doctor of Philosophy

in

Astronomy

in

Astronomy Program
Physics and Astronomy department
Seoul National University

Committee:

Professor	Hyung Mok Lee
Professor	Bon-Chul Koo
Professor	Yong-Sun Park
Doctor	Do-Young Byun
Doctor	Jae-Joon Lee

To Father, Mother, and My Family, for all of your support, patience, and endless love.

ABSTRACT

Supernova (SN) explosion is one of the most energetic events in a galaxy, which injects enormous energy (10^{51} erg) into the interstellar medium and supplies heavy elements and possibly dust grains. Because massive stars are formed by the gravitational collapse of molecular clouds (MCs), there is a good possibility that a supernova remnant (SNR) interacting with its parental MC. The evolution and physical characteristics of its remnant, i.e., the SNRs, are strongly governed by the environment. Also, the SNR shock wave propagating into the MC compresses, accelerates, heats, and even destroys the cloud. It can also change the chemical evolution of the cloud, and possibly can trigger star formation. In this thesis, I have carried out radio and infrared studies to understand the characteristics of the interaction between SNRs and MCs.

In the first part, I present the results of ^{12}CO $J = 1-0$ line observations of eleven Galactic SNRs obtained using the Seoul Radio Astronomy Observatory (SRAO) 6-m radio telescope. The observation is made as a part of the SRAO CO survey of SNRs between $l = 70^{\circ}$ and 190°, which is intended to identify SNRs interacting with MCs. The mapping areas for the individual SNRs are determined to cover their full extent in the radio continuum. I use half-beam grid spacing ($60''$) for 9 SNRs and full-beam grid spacing ($120''$) for the rest. I detect CO emission towards most of the remnants. In six SNRs, MCs showed a good spatial relation with their radio morphology, although no direct evidence for the interaction was detected. Two SNRs are particularly interesting: G85.4+0.7, where there is a filamentary molecular cloud along the radio shell, and 3C434.1, where a large molecular cloud appears to block the western half of the remnant.

In the second part, I present a detailed follow-up study of the semicircular Galactic SNR 3C434.1 (G94.0+1.0). I observe an area covering the whole SNR in the ^{12}CO $J = 1$–0 emission line using the SRAO 6-m telescope, and find a large molecular cloud superposed on the faint western part of the SNR. The cloud is elongated

along the north-south direction and shows a very good spatial correlation with the radio features of the SNR. I carry out ^{12}CO $J = 2$–1 line observations of this cloud using the Kölner Observatorium für Sub-Millimeter Astronomie (KOSMA) 3-m telescope and detect a region in which the ^{12}CO $J = 2$–1 to $J = 1$–0 ratio was high ($\sim$ 1.6). This higher excitation together with the morphological relation, strongly suggest that the molecular cloud have interacted with the SNR. Based on the systematic velocity of the molecular cloud (-13 km s^{-1}), I estimate a kinematic distance of 3.0 kpc to the SNR-molecular cloud system and derive the physical parameters of the SNR. I examine the variation of the radio spectral index over the remnant and find that it is flatter in the western part, wherein the SNR is interacting with the molecular cloud. I therefore propose that 3C434.1 is the remnant of a supernova explosion that occur just outside the boundary of a relatively thin, sheet-like molecular cloud. I present a hydrodynamic model showing that its asymmetric radio morphology can result from its interaction with this blocking molecular cloud.

In the third part, I present far-infrared (far-IR) studies of Galactic SNRs. The new high-resolution data from *AKARI* FIS (version 2.0) and *Herschel* PACS/SPIRE reveals detailed far-IR features that we have not seen before. Comparing the *AKARI* and *Herschel* images with the radio continuum and X-ray images, I have found that 59 out of 294 known SNRs have far-IR counterpart by visual inspection method. Most far-IR detected SNRs show shell, clump, or filament structures. I derive the far-IR fluxes of the detected SNRs and carry out statistical studies of the far-IR SNRs.

Keywords: ISM: supernova remnants – ISM: kinematics and dynamics – ISM: molecules – ISM: clouds – ISM: dust, extinction – radio lines: ISM – infrared: ISM

Student Number: 2006-30122

Contents

ABSTRACT **i**

List of Figures **ix**

List of Tables **xi**

1 Introduction **1**

1.1 Supernova and Supernova Remnants 1

1.2 Interacting SNRs with molecular clouds 2

1.3 Evidence of SNR interaction with MCs 3

1.4 CO and IR Surveys of Galactic SNRs 4

1.4.1 CO survey 4

1.4.2 IR survey 5

1.5 Motivation & Overview of the Thesis 6

Bibliography 8

2 SRAO CO Observation of 11 Supernova Remnants in $l = 70^\circ$ to 190° **10**

2.1 Introduction 10

2.2 Observations 12

2.3 Results 16

2.3.1 G73.9+0.9 16

2.3.2 G76.9+1.0 . . . 18
2.3.3 G84.2−0.8 . . . 21
2.3.4 G85.4+0.7 . . . 21
2.3.5 G85.9−0.6 . . . 23
2.3.6 G93.3+6.9 (DA530) . . . 25
2.3.7 G94.0+1.0 (3C434.1) . . . 25
2.3.8 G166.2+2.5 (OA184) . . . 27
2.3.9 G179.0+2.6 . . . 30
2.3.10 G180.0−1.7 (S147) . . . 30
2.3.11 G182.4+4.3 . . . 34
2.4 Summary . . . 36
Bibliography . . . 37

3 CO *J*=1−0 and *J*=2−1 Line Observations of the Molecular Cloud - Blocked Supernova Remnant 3C434.1 41
3.1 Introduction . . . 41
3.2 Observations . . . 44
3.3 Results . . . 46
3.3.1 SRAO ^{12}CO $\boldsymbol{J} = 1$–0 . . . 46
3.3.2 KOSMA ^{12}CO $\boldsymbol{J} = 2$–1 . . . 49
3.4 Discussion . . . 53
3.4.1 New Distance to 3C434.1 and Its Physical Parameters . . . 53
3.4.2 Variation of Radio Spectral Index . . . 55
3.4.3 Interaction with the Molecular Cloud and Radio Morphology 61
3.5 Conclusion . . . 66
Bibliography . . . 68

4 AKARI/Herschel Far-Infrared Survey of Galactic Supernova Remnants 71
4.1 Introduction . . . 71

4.2 AKARI and Herschel Data 73
4.3 Results 75
4.3.1 SNR Identifications 75
4.3.2 Distributions of Detected SNRs 83
4.3.3 Flux measurement 83
4.3.4 Far-IR Correlations between Spitzer, AKARI, and Herschel Data 90
4.3.5 Far-IR Color-Color Diagrams 96
4.3.6 Far-IR and Radio Flux Correlations 102
4.4 Discussion 106
4.4.1 Far-IR Characteristics of Galactic SNRs 106
4.4.2 Far-IR and Radio Relations of Interacting SNRs with Molecular Clouds 108
4.4.3 Possible correlations between radio and far-IR bands in interacting SNRs with MCs 109
4.5 Summary 110
Bibliography 112

5 Summary and Conclusion **116**

요 약 **119**

감사의 글 **121**

List of Figures

2.1 Average ^{12}CO $J = 1-0$ spectra of 11 supernova remnants 15
2.2 ^{12}CO $J = 1-0$ average intensity maps of G73.9+0.9 17
2.3 ^{12}CO $J = 1-0$ average intensity maps of G76.9+1.0 19
2.4 ^{12}CO $J = 1-0$ average intensity maps of G84.2−0.8 20
2.5 ^{12}CO $J = 1-0$ average intensity maps of G85.4+0.7 22
2.6 ^{12}CO $J = 1-0$ average intensity maps of G85.9−0.6 24
2.7 ^{12}CO $J = 1-0$ average intensity maps of G93.3+6.9 26
2.8 ^{12}CO $J = 1-0$ average intensity maps of G94.0+1.0 28
2.9 ^{12}CO $J = 1-0$ average intensity maps of G166.2+2.5 29
2.10 ^{12}CO $J = 1-0$ average intensity maps of G179.0+2.6 31
2.11 ^{12}CO $J = 1-0$ average intensity maps of G180.0−1.7 32
2.12 ^{12}CO $J = 1-0$ average intensity maps of G182.4+4.3 33

3.1 Radio continuum image of 3C434.1 at 1420 MHz data 42
3.2 SRAO ^{12}CO $J = 1-0$ average spectrum of 3C434.1. 45
3.3 SRAO ^{12}CO $J = 1-0$ contoured channel maps of prominent velocity components 47
3.4 Detailed SRAO ^{12}CO $J = 1-0$ channel maps of 3C434.1 from −10.0 to −15.6 km s^{-1} 48
3.5 ^{12}CO $J = 2-1/1-0$ ratio map 50
3.6 CO molecular line spectra of SRAO $J = 1-0$ and KOSMA $J = 2-1$ at region A 51

3.7 CGPS HI distribution of 3C434.1 from −9.7 to −15.5 km s^{-1} 54
3.8 Spectral index map of 3C434.1 56
3.9 Convolved 1420 MHz radio continuum image of 3C434.1 57
3.10 $T-T$ plot results of four regions obtained by pixel-to-pixel comparison of CGPS 408 and 1420 MHz radio continuum images. 58
3.11 Hydrodynamic evolution model for 3C434.1 62
3.12 Schematic diagram of the SNR 3C434.1 64

4.1 Distributions of known and detected SNRs 84
4.2 Images of *Spitzer* 24 μm, *Herschel* 70, 160, 250, 350 μm, X-ray, and radio continuum data of the selected SNRs (Kepler, G8.3−0.0, G10.6−0.0, G11.1−1.0, G11.1+0.1, and G11.2−0.3) 85
4.3 Images of *Spitzer* 24 μm, *Herschel* 70, 160, 250, 350 μm, X-ray, and radio continuum data of the selected SNRs (G15.9+0.2 , G20.4+0.1, G27.4+0.0, 3C391, W44, and 3C396) 86
4.4 Images of *Spitzer* 24 μm, *Herschel* 70, 160, 250, 350 μm, X-ray, and radio continuum data of the selected SNRs (W49B, G54.1+0.3, Cygnus Loop, Cassiopeia A, Tycho, and Crab Nebula) 87
4.5 Images of *Spitzer* 24 μm, *Herschel* 70, 160, 250, 350 μm, X-ray, and radio continuum data of the selected SNRs (IC443, Puppis A, G292.0+1.8, Kes 17, G311.5−0.3, and G349.7+0.2) 88
4.6 Correlation between *AKARI* 65 μm and *Herschel* 70 μm fluxes . . 91
4.7 Correlation between *AKARI* 65 μm and *Spitzer* 70 μm fluxes . . . 92
4.8 Correlation between *Spitzer* 70 μm and *Herschel* 70 μm fluxes . . . 93
4.9 Correlation between *AKARI* 160 μm and *Herschel* 160 μm fluxes . 94
4.10 *AKARI* and *Herschel* color-color diagrams. 98
4.11 Color-color diagrams from the detected SNRs using *Spitzer*, *AKARI*, and *Herschel* fluxes 99
4.12 Color-color diagrams from the detected SNRs using *AKARI* and *Herschel* fluxes 100

4.13 SEDs of 24 selected SNRs 101
4.14 Relation of $Herschel$ 60 μm and $AKARI$ 65 μm fluxes with 1 GHz radio fluxes. 103
4.15 Relation of $Herschel$ 160 μm and $AKARI$ 160 μm fluxes with 1 GHz radio fluxes. 104

List of Tables

2.1 List of Supernova Remnants between l=70° and 190° 14
2.2 Mapping Parameters of SNRs 16
2.3 Summary of Results 35

3.1 Physical parameters of SNR 3C434.1 59

4.1 Instrument characteristics of *AKARI* and *Herschel* 74
4.2 FIR Detected SNRs in AKARI and Herschel Survey 76
4.2 FIR Detected SNRs in AKARI and Herschel Survey 77
4.2 FIR Detected SNRs in AKARI and Herschel Survey 78
4.2 FIR Detected SNRs in AKARI and Herschel Survey 79
4.2 FIR Detected SNRs in AKARI and Herschel Survey 80
4.2 FIR Detected SNRs in AKARI and Herschel Survey 81
4.2 FIR Detected SNRs in AKARI and Herschel Survey 82
4.3 Far-IR Fluxes of 24 Selected Galactic SNRs 89
4.4 Relation of fluxes between far-IR and 1 GHz radio continuum . . . 105

Chapter 1

Introduction

1.1 Supernova and Supernova Remnants

Supernova (SN) explosions are one of the most energetic events in a galaxy, which release enormous energy (E $\sim 10^{51}$ erg) to the interstellar medium and supply heavy elements and possibly dust grains. Supernovae (SNe) can be divided into two large groups according to the existence of the hydrogen emission lines in their spectra. Type Ia SNe result from a white dwarf exceeding a critical mass by mass accretion from a companion star in a binary system. These SNe show no hydrogen and no compact source remains. Type II SNe, on the other hand, result from the core-collapse of massive stars, greater than 8 $M_{\odot}$. They have hydrogen lines in their spectra and leave a compact stellar object, a neutron star or a black hole (Woosley & Weaver 1986).

Supernova remnants (SNRs) are structure resulting from SN explosions and normally identified by their nonthermal radio emission from the synchrotron process. According to the morphology at radio wavelengths, SNRs are generally classified into shell, filled-centre, and composite types (Case & Bhattacharya 1996). Shell remnants are characterized by a ring-like and limb-brighten morphology with a steep radio spectral index ($\alpha \sim 0.5$), which is defined as a power law relation between

flux density (S_ν) at a given frequency (ν) of $S_\nu \propto \nu^{-\alpha}$. Filled center remnants (also called plerions, or Crab-like remnants) show centrally brighten morphology with a flat radio spectrum ($\alpha \sim 0.1$). The central emission is believed to be powered by a central compact source such as a pulsar wind nebulae or a neutron star with a highly polarized radio emission. Composite remnants have characteristics of both shell and centrally brighten morphology. These SNRs show a flat spectrum emission at centrally brighten regions and a steeper spectral index at shell-brighten regions. If remnants are modified by inhomogeneities in the distribution of the surrounding interstellar matter, these can be shown as irregular-shaped features.

1.2 Interacting SNRs with molecular clouds

The interaction between SNRs and molecular clouds (MCs) plays a crucial role in a part of Galactic ecology. Supernova explosions strongly affect the environment, and at the same time, the evolution of a SNR is strongly governed by the environment itself. Because massive stars are formed by the gravitational collapse of MCs, there are many possibilities that a SN explodes in the vicinity of its parental MCs. The SNR shock waves propagate into the MCs as they compressed, accelerated, heated, and even destroyed the clouds. Also, they not only change the chemical evolution of the cloud, but possibly trigger star formation (Yusef-Zadeh et al. 2003). About 70-80 % of Galactic SNRs (∼294; Green 2014) are supposed to be core-collapse SNRs from massive stars ($> 8M_\odot$), which are born in dense molecular clouds (Huang & Thaddeus 1986; Smith et al. 2011). Among these, theoretically, early B type stars (8-12$M_\odot$) could be a progenitor of interacting SNRs with molecular clouds (MCs) rather than O-type stars which have adequate photoionizing radiation and strong stellar wind to clear a region in radius of molecular clumps (Chevalier 1999).

For this reason, especially, CO and infrared (IR) data are an excellent tracer and commonly used for studying of the SNRs. CO molecules are sensitive diagnostics to determine the density, temperature, and velocity structure of the shocked

environment. The associations between SNRs with MCs provide an important tool for estimating the kinematic distance of the SNR using the radial velocity of the CO molecular gas. The CO emission is also useful method to estimate the physical property by excitation analyses. Comparisons between CO J = 2–1 and CO J = 1–0 emission intensities are used to probe denser and warmer gas by ultraviolet radiation originated from the SN explosions. The numerical simulation can be used to understand the formation and evolution of the SNR morphology, the location of SNR explosion, and so on. SNRs interacting with molecular clouds are usually centrally-brightened in X-ray while they appear shell-like in far-IR. The far-IR emissions in these SNRs are probably from radiately-heated dust grains in dense ambient medium. Using the far-IR data, a systematic study of interacting SNRs with molecular clouds can be useful to understand the heating mechanisms and the far-IR characteristics of these SNRs. Therefore, the CO and IR studies at shocked environment provide an important clue to understand these physical and kinematic processes associated with the shocks.

1.3 Evidence of SNR interaction with MCs

The SNRs interacting with MCs have several important astrophysical implications: 1. determination of SNR distance, 2. influence of shock physics, 3. dynamical evolution of SNR, and 4. thermal dust emission in dust heating process. About 20∼30 % out of the 294 Galactic SNRs (Green 2014) are known to be interacting or associating with molecular clouds (Jiang et al. 2010). Half of them are detected direct evidences for shocked molecular clouds, and the rest of them are revealed the spatial correlation or the morphological agreement with nearby molecular cloud without striking evidence.

As the direct evidence of the interaction of SNRs with MCs, molecular line broadening or asymmetric profile is one of the important evidence to identify the shocked region. IC443 is a representative object with direct evidence from shocked

atomic and molecular gases (Snell et al. 2005; Lee et al. 2012, and references therein). Also, high CO $J = 2$–1 and CO $J = 1$–0 line ratio (> 1) strongly indicates that the presence of warm and dense gas, presumably heated by the shock driven by the SNR (Seta et al. 1998). The 1720-MHz OH maser as a signpost of SNR-MC interactions is another important kinematic evidence. From SNRs W28, W44, and IC443, OH maser emissions were detected behind the leading edge of the shock (Claussen et al. 1997). According to theoretical calculations (Lockett et al. 1999; Wardle 1999), the masers arise only in slow, non-dissociative C-shocks with a large OH column density, which can be met only when the shock is observed tangentially (see the review by Wardle & Yusef-Zadeh 2002). Strong SNR shocks interacting with molecular clouds may produce high-energy gamma-ray emission due to enhanced pion decay emission from the collision of cosmic ray protons accompanied with efficient kinematic energy conversion in a dense molecular environment. The gamma-ray emission detected towards the SNRs CTB 37B, IC 443, and W51C indeed show an extended spatial distribution coincident with dense molecular clouds (Aharonian et al. 2008; Acciari et al. 2009; Abdo et al. 2009). This also could be the direct evidence for the production of cosmic ray protons by SNR shocks. The spatial correlation or correspondence of molecular features with SNR morphology are the suggestive and indirect evidence to determine the interacting SNRs with MCs.

1.4 CO and IR Surveys of Galactic SNRs

1.4.1 CO survey

About 294 SNRs are known in our Galaxy (Green 2014), and presently, about 70 of them are known to be interacting with MCs (Jiang et al. 2010). In previous CO survey, Huang & Thaddeus (1986) studied a molecular environment of Galactic SNRs and showed observational results of the distribution of molecular clouds with SNRs in the outer Galaxy. They used 1.2 meter telescope, and covered 26 SNRs from $l = 60^\circ$ to 210°. About half of them showed spatially coincident with large

molecular cloud complexes. They suggested that the progenitor stars of these SNRs could be born in the neighboring molecular complexes, and a spatial correlation between an SNR and a MCs support a significant meaning for origin of the SNRs from the core-collapse SNe. Their results were useful for studying the distributions of large molecular cloud complexes near the SNRs, but have a limitation in studying individual SNRs in detail due to the low angular resolution ($\sim 8'.7$) of the telescope. More recently, large-scale CO surveys of the galactic plane have been conducted such as the Outer Galaxy Survey ($l = 102^\circ \sim 141^\circ.5$) or the Galactic Ring Survey (GRS) using the 14-m telescope of the Five College Radio Astronomy Observatory with an FWHM of $50''$ (Taylor et al. 2003; Jackson et al. 2006). There have been studies on individual SNRs in this survey area; however, no systematic studies have been conducted.

1.4.2 IR survey

Since *IRAS* was launched, various IR studies on Galactic SNRs have been carried out by using large number of samples in 10 to 100 μm bands. Arendt (1989) and Saken et al. (1992) examined $\sim$160 Galactic SNRs and could find clear IR emission from about 30 remnants. Their study also revealed that dust grains in older SNRs are colder and more massive, so they suggested that the correlation between the age of SNRs and the effect of dusty environment on SNRs. However, IRAS study had a limitation for the analysis of small SNRs ($< 30'$) because of low resolution. Additionally, the longest wavelength band of 100 μm was not enough to define the spectral energy distributions for the estimation of dust properties of SNRs.

Almost two decades later, the *Spitzer* GLIMPSE survey data in IRAC (3.6, 4.5, 5.8, and 8.0 μm) and MIPS (24 and 70 μm) bands has been used to explore inner galactic SNRs ($10^\circ < |l| < 65^\circ$, $|b| < 1^\circ$) with high resolution. Reach et al. (2006) and Lee (2005) detected near-IR emission from 18 and 16 interacting SNRs with molecular clouds out of 95 and 100 SNRs within the GLIMPSE field. Pinheiro Gonçalves et al. (2011) searched for mid-IR counterpart from the SNRs and identified

spatially correlated features from 39 out of 121 SNRs in the MIPS data. Among the interacting SNRs with MCs, a few targets showed bright far-infrared (far-IR) emission. In color-color diagrams from *Spitzer* data, the ratio of [F70/F24] is larger than 1. The interacting SNR with MCs located at upper-right part of color-color diagrams (Pinheiro Gonçalves et al. 2011). In spite of higher angular resolution and sensitivity, no data of outer Galactic SNRs is one of its limitations.

1.5 Motivation & Overview of the Thesis

My research has been conducted in order to understand physical and dynamical evolution of interacting SNRs with MCs and their ambient medium. To study physical and morphological characteristics for the interacting SNRs with MCs, radio and infrared studies have provided the helpful information. For detailed studies, however, we need systematic study for Galactic SNRs with high resolution and wide *l*-*b* coverage in CO and IR. Recently, far-Infrared (far-IR) data of all-sky survey (*Spitzer*, *AKARI*, and *Herschel*) are available for the study of the correlation between CO and IR in SNR-MC association. The photometric data of *AKARI* FIS and *Herschel* PACS/SPIRE are especially quite useful in statistical and systematic studies for Galactic SNRs. *AKARI* provides all sky survey data to reveal large scale far-IR structures, and *Herschel* supports Galactic plane data with high resolution and wide-band coverage. So, these two data enable us to reveal the detailed structures that we have not seen before. So, the purpose of this study is to study SNRs interacting with MCs systematically with CO and IR survey, to reveal the physical and morphological correlations among the radio continuum, CO, and dust emissions around SNRs, and to derive physical properties and dust heating mechanism of SNRs interacting SNRs with MCs.

In this thesis, I have studied interacting SNRs with MCs using CO and far-IR data. More specifically, in chapter 2, I present the results of ^{12}CO $J = 1 - 0$ line observations of 11 Galactic SNRs using the Seoul Radio Astronomy Observatory

6-m radio telescope. In chapter 3, I report more detailed study about SNR 3C434.1, which reveals the evidence of interaction between molecular clouds with the remnant. In chapter 4, I show a complete far-IR catalog of Galactic SNRs and study far-IR properties of interacting SNRs with MCs. A summary of this thesis is shown in Chapter 5.

Bibliography

Abdo, A. A., Ackermann, M., Ajello, M., et al. 2009, ApJ, 706, L1

Acciari, V. A., Aliu, E., Arlen, T., et al. 2009, ApJ, 698, L133

Aharonian, F., Akhperjanian, A. G., Barres de Almeida, U., et al. 2008, A&A, 490, 685

Andersen, M., Rho, J., Reach, W. T., Hewitt, J. W., & Bernard, J. P. 2011, ApJ, 742, 7

Arendt, R. G. 1989, ApJS, 70, 181

Case, G., & Bhattacharya, D. 1996, A&AS, 120, 437

Chevalier, R. A. 1999, ApJ, 511, 798

Claussen, M. J., Frail, D. A., Goss, W. M., & Gaume, R. A. 1997, ApJ, 489, 143

Green, D. A. 2014, Bulletin of the Astronomical Society of India, 42, 47

Huang, Y.-L., & Thaddeus, P. 1986, ApJ, 309, 804

Jackson, J. M., Rathborne, J. M., Shah, R. Y., et al. 2006, ApJS, 163, 145

Jiang, B., Chen, Y., Wang, J., et al. 2010, ApJ, 712, 1147

Lee, H.-G. 2005, JKAS, 38, 385

Lee, J.-J., Koo, B.-C., Snell, R. L., et al. 2012, ApJ, 749, 34

Lockett, P., Gauthier, E., & Elitzur, M. 1999, ApJ, 511, 235

Pinheiro Gonçalves, D., Noriega-Crespo, A., Paladini, R., Martin, P. G., & Carey, S. J. 2011, AJ, 142, 47

Reach, W. T., Rho, J., Tappe, A., et al. 2006, AJ, 131, 1479

Saken, J. M., Fesen, R. A., & Shull, J. M. 1992, ApJS, 81, 715

Seta, M., Hasegawa, T., Dame, T. M., et al. 1998, ApJ, 505, 286

Smith, N., Li, W., Filippenko, A. V., & Chornock, R. 2011, MNRAS, 412, 1522

Snell, R. L., Hollenbach, D., Howe, J. E., et al. 2005, ApJ, 620, 758

Taylor, A. R., Gibson, S. J., Peracaula, M., et al. 2003, AJ, 125, 3145

Wardle, M. 1999, ApJ, 525, L101

Wardle, M., & Yusef-Zadeh, F. 2002, Science, 296, 2350

Woosley, S. E., & Weaver, T. A. 1986, ARA&A, 24, 205

Yusef-Zadeh, F., Wardle, M., Rho, J., & Sakano, M. 2003, ApJ, 585, 319

Chapter 2

SRAO CO Observation of 11 Supernova Remnants in $l = 70^\circ$ to 190°

2.1 Introduction

[1] Supernova (SN) explosions are one of the most energetic events that can occur in a galaxy. SN explosions strongly modify the environment, and at the same time, the evolution of a supernova remnant (SNR) is governed primarily by the environment itself. As stars are formed due to the gravitational collapse of molecular clouds, there is a large possibility that a SN explodes adjacent to its parental molecular cloud (MC). Thus, an environment with molecular clouds may not be unusual during a SNR evolution.

There are indeed SNRs that show direct evidence of SNR interaction with molecular clouds (e.g., see Koo 2003; Jiang et al. 2010). IC443 is a prototypical object from which high-velocity, broad emission lines from shocked atomic and molecular gases have been detected (DeNoyer 1979; Snell et al. 2005; Lee et al. 2008, 2012, and ref-

[1] This chapter is published in the Astrophysics and Space Science, 2012, 342, 389

erences therein). Shock-excited infrared emission lines from H_2 and other molecules have been detected as well. On the other hand, it is proposed that centrally enhanced thermal X-ray emissions or the spatial coincidence of molecular clouds can serve as an indirect indication of SNR-MC interaction. SNR 3C391 belongs to this category, having break-out morphology in radio emission (Reach et al. 1999; Chen et al. 2004).

SNR-MC interactions have several important astrophysical implications. Strong SNR shocks interacting with molecular clouds may produce high-energy gamma-ray emission due to enhanced pion decay emission from the collision of cosmic ray protons accompanied with efficient kinematic energy conversion in a dense molecular environment. The gamma-ray emission detected towards the SNRs CTB 37B, IC 443, and W51C indeed show an extended spatial distribution coincident with dense molecular clouds (Aharonian et al. 2008; Acciari et al. 2009; Abdo et al. 2009). This could be the first direct evidence for the production of cosmic ray protons by SNR shocks. The shocked, dense molecular gas could provide a physical condition for maser emission, e.g., 1720-MHz maser line ($^2\Pi_{3/2}$, $J = \frac{3}{2}$, $F = 2 \rightarrow 1$) of the OH molecule. From SNRs W28, W44, and IC443, OH maser emissions were detected behind the leading edge of the shock (Claussen et al. 1997), and according to theoretical calculations (Elitzur 1976; Lockett et al. 1999; Wardle 1999), the masers arise only in slow, non-dissociative C-shocks with a large OH column density, which can be met only when the shock is observed tangentially (see the review by Wardle, M., & Yusef-Zadeh 2002).

About 270 SNRs are known in our Galaxy (Green 2009), and presently, about 20% – 30% of them are known to be interacting with molecular clouds (Jiang et al. 2010). However, insufficient effort has been made to conduct systematic searches. Huang & Thaddeus (1986) studied a molecular environment of galactic SNRs in $l = 70^\circ$ to 210°. However, due to the insufficient angular resolution ($\sim 8'.7$) of the telescope, the results were only useful for studying the distributions of large molecular cloud complexes near SNRs. More recently, large-scale CO surveys of the galactic

plane have been conducted such as the Outer Galaxy Survey (l = 102°.5 – 141°.5) or the Galactic Ring Survey using the 14-m telescope of the Five College Radio Astronomy Observatory with an FHWM of 50″ (Taylor et al. 2003; Jackson et al. 2006). There have been studies on individual SNRs in this survey area; however, no systematic studies have been conducted.

On the basis of the above background, we decided to carry out a systematic CO study of SNRs using the Seoul Radio Astronomy Observatory (SRAO) 6-m telescope. We limited the targets to the SNRs in $l = 70°$ to 190°. The targets in the inner galaxy were excluded because of the ambiguity in determining the association. We observed most of the SNRs listed the Green's 2004 catalog (Green 2004). Some results of the survey were reported previously by Byun (2004) and Byun et al. (2006). They observed 9 SNRs having bright X-ray emissions and large angular sizes. They detected broad-line CO emissions from two SNRs (HB 21 and HB 3) and also found a morphological correlation between the CO and radio continuum distribution for two other SNRs (γ-Cygni and HB 9). For the remaining five SNRs, no evidence of SNR-MC interaction was observed. In this paper, we present the results obtained for eleven other SNRs.

This paper is organized as follows. In § 2.2, the observation details and target selection are explained. In § 2.3, the results for individual SNRs are presented. Section 2.4 summarizes the main results of this paper.

2.2 Observations

^{12}CO J=1−0 (115.271204 GHz) observations were carried out from October 2003 to May 2005 using SRAO 6-m telescope. The telescope has an FWHM beam size of 120″ and a main beam efficiency of 0.70 at 115 GHz (Koo et al. 2003). We used a 100 GHz SIS mixer receiver with a single-side band filter (Lee et al. 2002) and a 1024-channel auto-correlator with 50 MHz bandwidth, corresponding to a velocity coverage of 130 km s^{-1} (Choi et al. 2003). The system temperature ranged from

500 to 800 K depending on the elevation and weather conditions. Typical *rms* noise level on T_{mb} scale was ∼0.3 K at a 1 km s^{-1} velocity resolution. In order to check the system performance, we regularly observed the bright standard source near the target at one or two hour intervals. Pointing accuracy was better than 20″. The data were reduced by using the CLASS[2] software in the Gildas package developed by IRAM.

The targets were selected as follows. First, the Galactic longitudes of the SNRs are limited to $l = 70°$ to 190°. Toward the inner Galactic region, many clouds are superposed along the line-of-sight, and hence, it is difficult to confirm the association of SNRs with molecular clouds. On the other hand, the SNRs beyond 190° are at low declinations due to which we have a rather limited observing time for them. According to the Green's SNR catalog (Green 2004), there are 35 SNRs in this longitude range, and they are listed in Table 2.1[3]. Second, the angular sizes of the SNRs are limited to ≥10′ and ≤180′, considering the beam size of the SRAO 6-m telescope. If the angular size is excessively small, the morphological comparison between the SNR and the molecular cloud becomes difficult, whereas if it is excessively large, the observation becomes highly time-consuming. Third, the SNRs in the area considered by the Five College Radio Astronomy Observatory Outer Galaxy Survey (FCRAO OGS) are excluded because the survey was performed with an adequate angular resolution (60″) and sensitivity. The FCRAO OGS survey covered the region $102°.5 < l < 141°.5$ and $-3° < b < 5°.4$ (Taylor et al. 2003). Finally, we excluded the SNRs observed by previous SRAO ^{12}CO $J = 1-0$ observations (Byun 2004, Byun et al. 2006). In the last column of Table 2.1, we list the references on the CO observations of individual SNRs.

The mapping areas for the individual SNRs are determined to cover their full extents in the radio continuum. Nine SNRs were observed with half-beam grid spacing (60″), whereas the two remaining SNRs were observed with full-beam grid spacing

[2]http://www.iram.fr/IRAMFR/GILDAS

[3]In the Green's 2009 catalog (Green 2009), the number has increased to 37.

Table 2.1 List of Supernova Remnants between l=70° and 190°

Galactic Coordinates	Name(s)	α(J2000) (h m s)	δ(2000) (° ′)	Size (arcmin)	Type[a]	CO[b] Observation
73.9 +0.9		20 14 15	+36 12	22?	S?	This paper
74.0 −8.5	Cygnus Loop	20 51 00	+30 40	230×160	S	—
74.9 +1.2	CTB87	20 16 02	+37 12	8×6	F	4
76.9 +1.0		20 22 20	+38 43	12×9	?	This paper
78.2 +2.1	γ Cygni SNR	20 20 50	+40 26	60	S	1, 5
82.2 +5.3	W63	20 19 00	+45 30	95×65	S	1
84.2 −0.8		20 53 20	+43 27	20×16	S	This paper, 6
84.9 +0.5[c]		20 50 30	+44 53	6	S	—
85.4 +0.7		20 50 40	+45 22	24	S	This paper
85.9 −0.6		20 58 40	+44 53	24	S	This paper
89.0 +4.7	HB21	20 45 00	+50 35	120×90	S	1, 2
93.3 +6.9	DA530	20 52 25	+55 21	27×20	S	This paper
93.7 −0.2	CTB104A	21 29 20	+50 50	80	S	3
94.0 +1.0	3C434.1	21 24 50	+51 53	30×25	S	This paper
106.3 +2.7		22 27 30	+60 50	60×24	?	3, 7
109.1 −1.0	CTB109	23 01 35	+58 53	28	S	3, 8
111.7 −2.1	Cassiopeia A	23 23 26	+58 48	5	S	3
114.3 +0.3		23 37 00	+61 55	90×55	S	3
116.5 +1.1		23 53 40	+63 15	80×60	S	3
116.9 +0.2	CTB 1	23 59 10	+62 26	34	S	1, 3
119.5 +10.2	CTA 1	00 06 40	+72 45	90?	S	1
120.1 +1.4	Tycho	00 25 18	+64 09	8	S	3
126.2 +1.6		01 22 00	+64 15	70	S?	3
127.1 +0.5	R5	01 28 20	+63 10	45	S	3
130.7 +3.1	3C58	02 05 41	+64 49	9×5	F	3
132.7 +1.3	HB3	02 17 40	+62 45	80	S	1, 3
156.2 +5.7		04 58 40	+51 50	110	S	1
160.9 +2.6	HB9	05 01 00	+46 40	140×120	S	1
166.0 +4.3	VRO 42.05.01	05 26 30	+42 56	55×35	S	1
166.2 +2.5[c]	OA 184	05 19 00	+41 55	90×70	S	This paper
179.0 +2.6		05 53 40	+31 05	70	S?	This paper
180.0 −1.7	S147	05 39 00	+27 50	180	S	This paper
182.4 +4.3		06 08 10	+29 00	50	S	This paper
184.6 −5.8	Crab Nebula	05 34 31	+22 01	7×5	F	—
189.1 +3.0	IC443	06 17 00	+22 34	45	C	3, 9

[a] Type of the SNR (S: Shell, F: Filled-Centre, C: Composite) (Green 2004)

[b] References are: (1) Byun (2004), (2) Byun et al. (2006), (3) FCRAO Survey (Taylor et al. 2003), (4) Kothes et al. (2003), (5) Higgs et al. (1983), (6) Feldt & Green (1993), (7) Kothes et al. (2001b), (8) Sasaki et al. (2006), (9) Snell et al. (2005).

[c] G84.9+0.5 and G166.2+2.5 (OA184) have been identified as HII regions (Foster et al. 2006, 2007) and removed in the Green's 2009 catalog.

Note. — The parameters of the SNRs are from the Green's 2004 catalog (Green 2004).

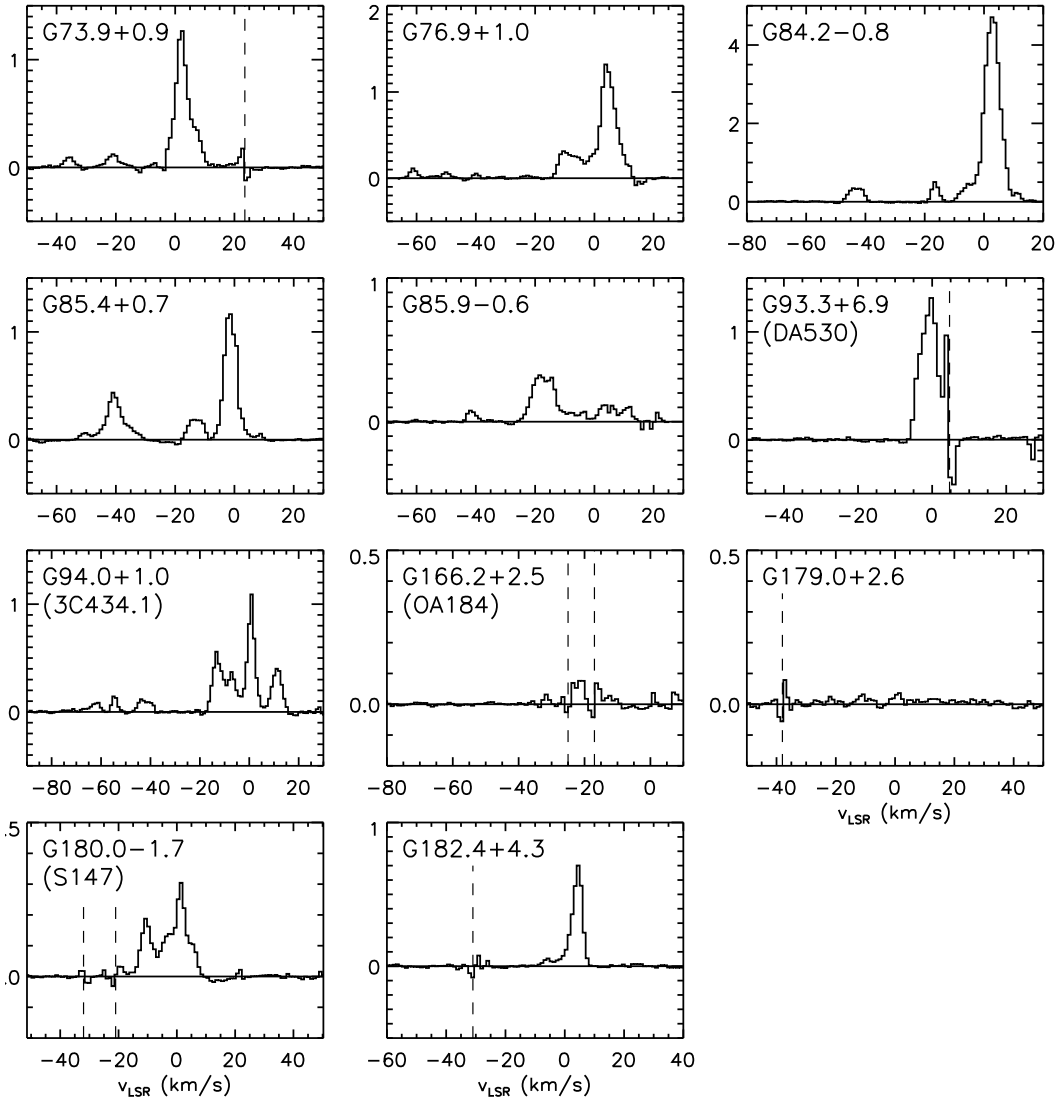

Figure 2.1 Average ^{12}CO $J = 1{-}0$ spectra of 11 supernova remnants. The dashed lines mark the telluric CO line positions.

Table 2.2 Mapping Parameters of SNRs

Galactic Coordinate	Name(s)	Size (arcmin)	Observed area (arcmin)	Grid Spacing (arcsec)
73.9 +0.9		22?	53×41	60
76.9 +1.0		12×9	17×18	60
84.2 −0.8		20×16	33×27	60
85.4 +0.7		24	51×61	60
85.9 −0.6		24	37×40	60
93.3 +6.9	DA530	27×20	37×36	60
94.0 +1.0	3C434.1	30×25	42×39	60
166.2 +2.5	OA184	90×70	97×94	60
179.0 +2.6		70	108×130	120
180.0 −1.7	S147	180	252×274	120
182.4 +4.3		50	63×61	60

(120″) via the position switching mode. Table 2.2 lists the observed areas and the grid spacings for the target SNRs. The total number of spectra obtained in this study is ∼45000.

2.3 Results

Figure 2.1 shows the average spectra toward 11 SNRs. Strong CO emission lines are detected toward all SNRs other than G166.2+2.5 and G179.0+2.6. In the following subsections, we summarize the results obtained for individual SNRs.

2.3.1 G73.9+0.9

G73.9+0.9 is located in the complex Cygnus area in the sky. This source has a faint and broad, spur-like structure in radio and is classified as an SNR on the basis of its polarization and spectral index (Reich et al. 1986). According to a recent

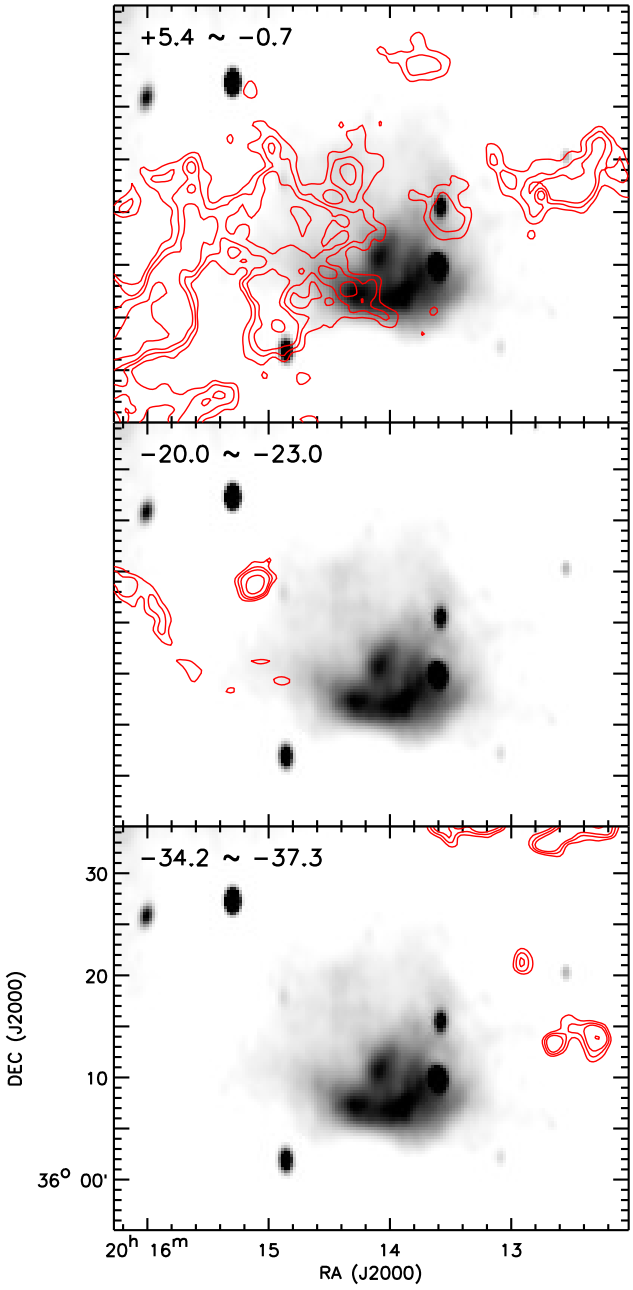

Figure 2.2 ^{12}CO $J = 1-0$ average intensity maps of G73.9+0.9 (contour levels: 1.2, 1.6, 2, 3 K). The gray-scale image is the Canadian Galactic Plane Survey (CGPS) 1420 MHz radio continuum image (scale range: 11∼21 K) (Taylor et al. 2003).

radio continuum study, the spectral index of this target is 0.23 and there could be a pulsar wind nebula in the central region (Kothes et al. 2006). In HI, Pineault et al. (1996) suggested that there are no obvious HI features associated with the remnant, although large-scale HI features at -45 km s^{-1} indicate a complementary morphology. Case et al. (1998) suggested a distance of 6.6 kpc, based on the $\Sigma - D$ relation.

According to our survey, CO molecular clouds appeared at around +2, -21, and -36 km s^{-1} (Fig. 2.1). The +2 km s^{-1} component was the most prominent (Fig. 2.2). At this velocity, there is a large and filamentary cloud crossing the northern part of the SNR along east-west direction. The southern part of the SNR is bright in radio continuum, whereas the northern part, where the CO cloud overlaps, is faint. However, there is no evidence of the interaction between the molecular cloud and the SNR. Although we detected a few clumpy clouds at other velocities, they showed no correlation with the SNR.

2.3.2 G76.9+1.0

This source is the smallest ($\sim 10'$) among our targets. It is a filled-center SNR with a diffuse extended envelope in the radio continuum, and it could be a pulsar wind nebula (Landecker et al. 1993; Kothes et al. 2006). Landecker et al. (1993) suggested a distance greater than 7 kpc based on its large rotation measure. Based on the $\Sigma - D$ relation, Case et al. (1998) estimated the distance to be about 4.7 kpc.

We find that the most prominent CO component that appears at $\sim$+5 km s^{-1} is distributed near the center and the southeast region of the remnant (Figs. 2.1 & 2.3). However, this velocity component shows no spatial correlation with the radio continuum. Several CO clouds are also detected around the SNR at a $v_{\rm LSR}$ from -12 to 0 km s^{-1} and near the south-east boundary at -40 km s^{-1}. However, there is no obvious morphological correlation between the radio and CO distribution.

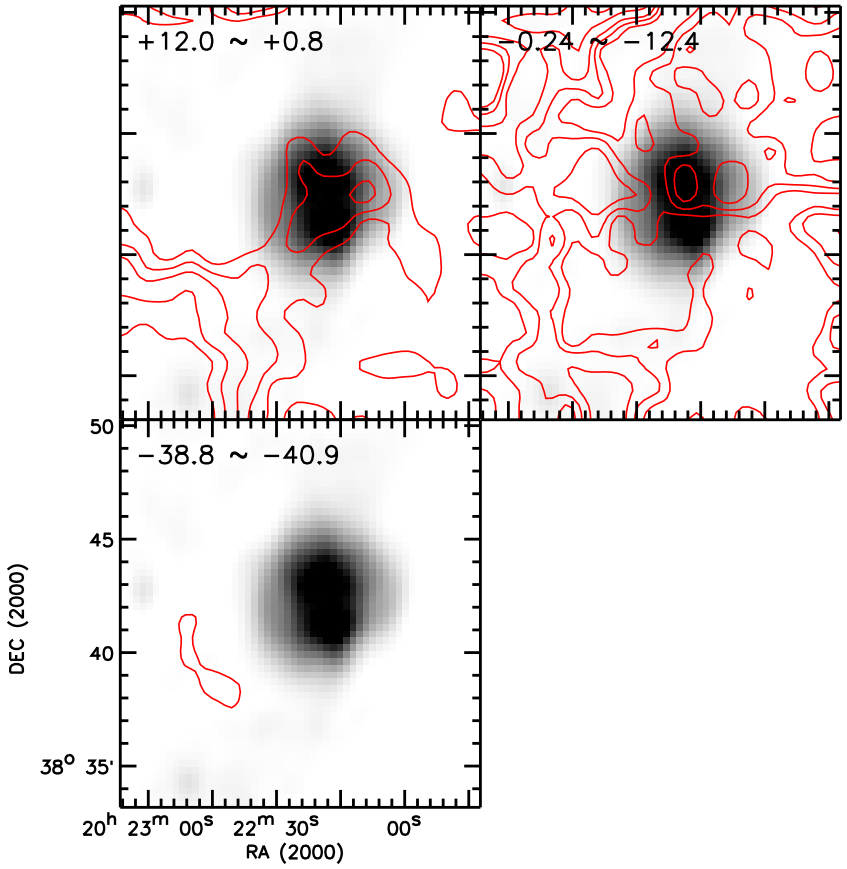

Figure 2.3 ^{12}CO $J = 1-0$ average intensity maps of G76.9+1.0 (contour levels: 0.5, 0.8, 1.2, 2, 3 K). The gray-scale image is the CGPS 1420 MHz radio continuum image (scale range: 11∼21 K).

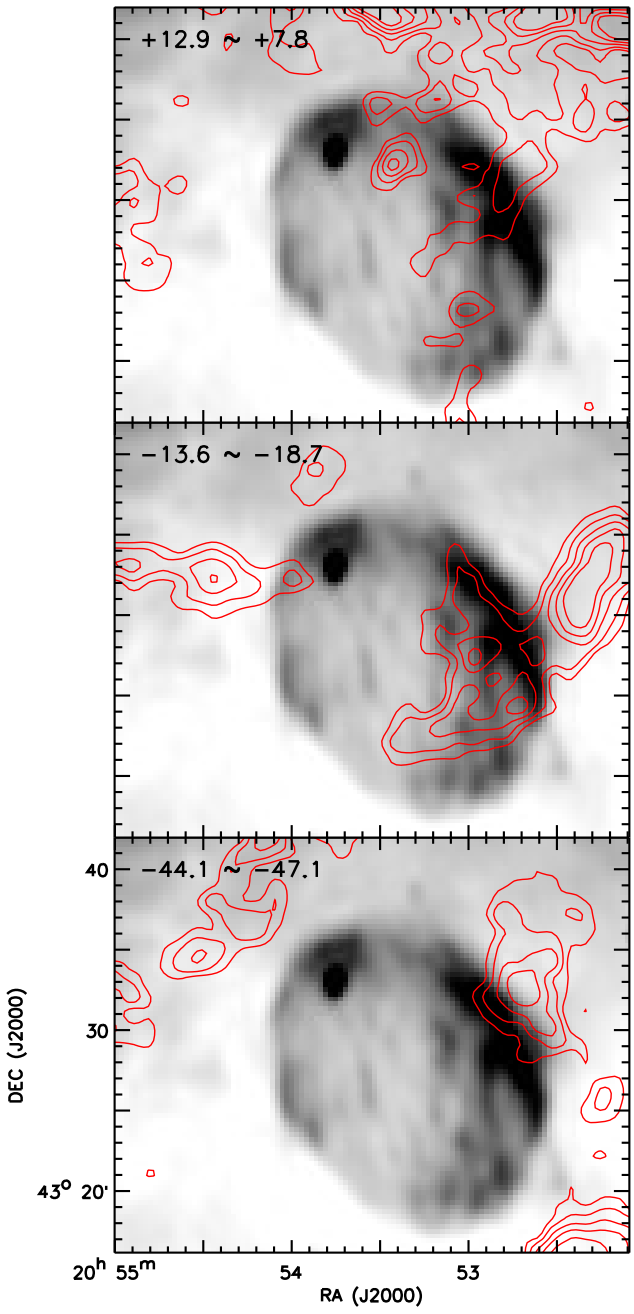

Figure 2.4 ^{12}CO $J = 1{-}0$ average intensity maps of G84.2−0.8 (contour levels: 0.5, 0.8, 1.2 ,1.6 ,2 K). The gray-scale image is the CGPS 1420 MHz radio continuum image (scale range: 11∼24 K).

2.3.3 G84.2−0.8

G84.2−0.8 is shell-type remnant having filamentary structures parallel to the major axis with no polarized emission (Matthews et al. 1980; Kothes et al. 2006). Huang & Thaddeus (1986) showed that this remnant lied at the south of a large molecular cloud complex at a $v_{\rm LSR}$ between −44 and −33 km s^{-1}. They estimated the kinematic distance to be 7.2 kpc and the total mass to be 8.5×10^5 M$_\odot$ for the cloud. Feldt & Green (1993) performed ^{12}CO $J = 1{-}0$ observation with the KOSMA 3-m telescope (FWHM = 3.′8) in addition to HI observations using the DRAO Synthesis Telescope (FWHM $\approx 1' \times 1.'5$). They found that the CO molecular cloud at −17 km s^{-1}, corresponding to a kinematic distance of ∼4 kpc is spatially coincident with the SNR. No OH maser emission was detected toward the remnant (Frail et al. 1996).

We detected CO emission at four velocities: ∼ +11, +2.7, −17, and −46 km s^{-1} (Fig. 2.1). The −17 km s^{-1} cloud detected by Feldt & Green (1993) is more clearly observed in our data (Fig. 2.4). There are two clouds: a large one in the west and a small one in the east. The large cloud in the west has a semi-circular shape and is localized inside the remnant. Its northwest boundary matches well with the boundary of the remnant with no asymmetric line emission. The radio continuum is enhanced in the region where a molecular cloud is located. These features suggest a possible interaction between the molecular cloud and the remnant. In order to confirm the interaction, we need to obtain more observations using higher transition CO lines. If this cloud were interacting with the SNR, the distance to the SNR would be 4.9 kpc according to the rotation curve of Brand & Blitz (1993). The velocity component of −46 km s^{-1} appears to be aligned along the southwest and the west. However, it does not show any correlated features with the remnant.

2.3.4 G85.4+0.7

G85.4+0.7 is shell-type SNR with two separated faint shells, discovered recently from the Canadian Galactic Plane Survey (CGPS) (Kothes et al. 2001a). Kothes et al. (2001a) detected a large HI loop structure surrounding the SNR at a $v_{\rm LSR}$ of

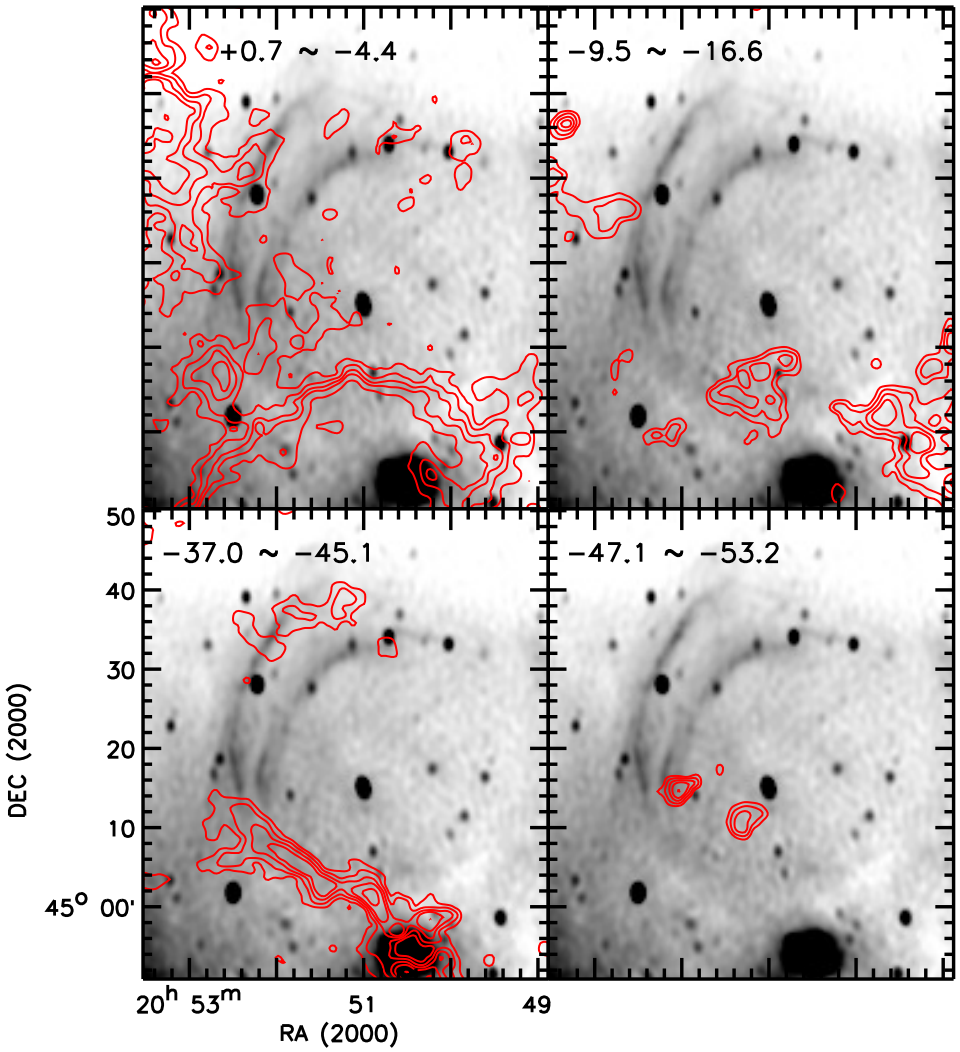

Figure 2.5 ^{12}CO $J = 1{-}0$ average intensity maps of G85.4+0.7 (contour levels: 0.6, 1.0, 1.5, 2, 3 K). The gray-scale image is the CGPS 1420 MHz radio continuum image (scale range: 8.5∼11.5 K).

-12 km s^{-1}. They interpreted the structure as a stellar-wind shell generated by the progenitor of the SNR, and proposed a distance of 3.8 kpc to the SNR corresponding to the velocity of the HI loop.

We detected CO emissions at ~ -1, -12, -41, and -50 km s^{-1} (Fig. 2.1). The molecular cloud at -41 km s^{-1} shows a considerably interesting feature (Fig. 2.5). This molecular cloud is in filamentary shape and aligned along the south-east boundary of the SNR. The spatial relation between the cloud and the SNR suggests that their association is very likely. The cloud extends to the bright, compact radio source below the remnant, which is the HII region G84.9+0.5 (Foster et al. 2007). The velocity of the HII region from radio recombination line observation is $v_{\rm LSR} = -39.3$ km s^{-1}, and Foster et al. (2007) proposed a kinematic distance of 4.9 kpc considering the noncircular motions near the Perseus spiral arm. The velocity of the CO cloud (-41 km s^{-1}) agrees with that of the radio recombination line, and the cloud surrounds the HII region, which indicates that they are physically associated. The CO emission lines in this area show asymmetric profiles that are probably related to the outflows of young stellar objects. If the -41 km s^{-1} molecular cloud were physically associated with both the HII region and the SNR, the distance to the SNR would be 4.9 kpc (Foster et al. 2007) or 7.2 kpc if we adopt the rotation curve of Brand & Blitz (1993). And it will be difficult to associate the HI loop structure detected by Kothes et al. (2001a) with the SNR. A detailed study on the CO gas and its association with the HII region and the SNR will be presented in a separate paper.

2.3.5 G85.9−0.6

G85.9−0.6 is a shell-type SNR discovered recently by the CGPS. Kothes et al. (2001a; 2006) suggested that the target might be located in the low-density inter-arm region at ∼5 kpc based on its faint radio and X-ray brightness. There was no particular feature observed from the HI and polarized emission. The distance based on the $\Sigma - D$ relation of Case et al. (1998) is 19.6 kpc.

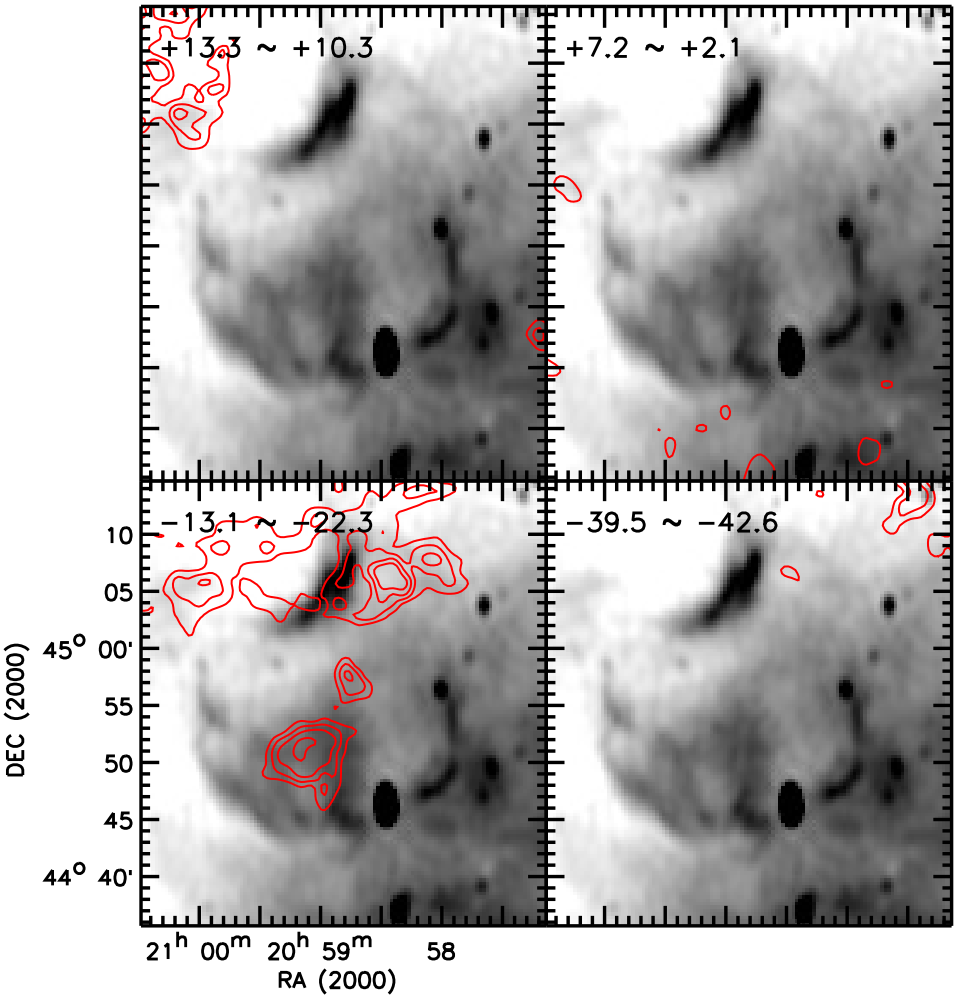

Figure 2.6 ^{12}CO $J = 1{-}0$ average intensity maps of G85.9−0.6 (contour levels: 0.7, 1.1, 1.5, 2 K). The gray-scale image is the CGPS 1420 MHz radio continuum image (scale range: 9.5∼14 K).

We detected CO molecular clouds at +12, +5, −20, and −41 km s^{-1} (Fig. 2.1). At −20 km s^{-1}, there is a large molecular cloud near the northern boundary of the SNR and small clouds in the central region of the SNR (Fig. 2.6). However, there are no indications suggesting the interaction of these clouds with the SNR. The distribution of CO molecular clouds at other velocities does not show any correlation with the radio morphology of the remnant.

2.3.6 G93.3+6.9 (DA530)

G93.3+6.9 is classified as bilateral type with a well-defined shell morphology in the radio continuum (Gaensler 1998). This remnant is located at the northern edge of the Cyg OB7 molecular cloud complex at 0.8 kpc that has $v_{\rm LSR} = -7$ to 0 km s^{-1} (Huang & Thaddeus 1998). Landecker et al. (1999) found an HI bubble at a distance of 3.5 kpc that could have been produced by stellar wind from the massive star progenitor. Foster et al. (2003) estimated the distance of 2.2 kpc by comparing their model of HI column density distribution with the observed HI data. From Chandra X-ray observations, Jiang et al. (2007) found an extended small hard X-ray feature at the centre of the remnant and proposed that it would be pulsar wind nebula. OH maser observation was made toward the remnant with negative results (Frail et al. 1996).

We detected CO emission at −6 to +5 km s^{-1} (Fig. 2.1). Diffuse emissions at $\sim$ −1.3 km s^{-1} appear to surround the north-west of the remnant although the morphological correlation between the CO and radio distribution is not clear (Fig. 2.7).

2.3.7 G94.0+1.0 (3C434.1)

G94.0+1.0 is a shell type SNR with an asymmetric shape. In radio continuum emission, the western area is faint and has no distinct shell-like feature in visible region, whereas a bright semi-circular shell is evident in the east. In CGPS 1420 MHz radio emission, there was no polarized emission (Willis 1973; Landecker et al. 1985; Kothes

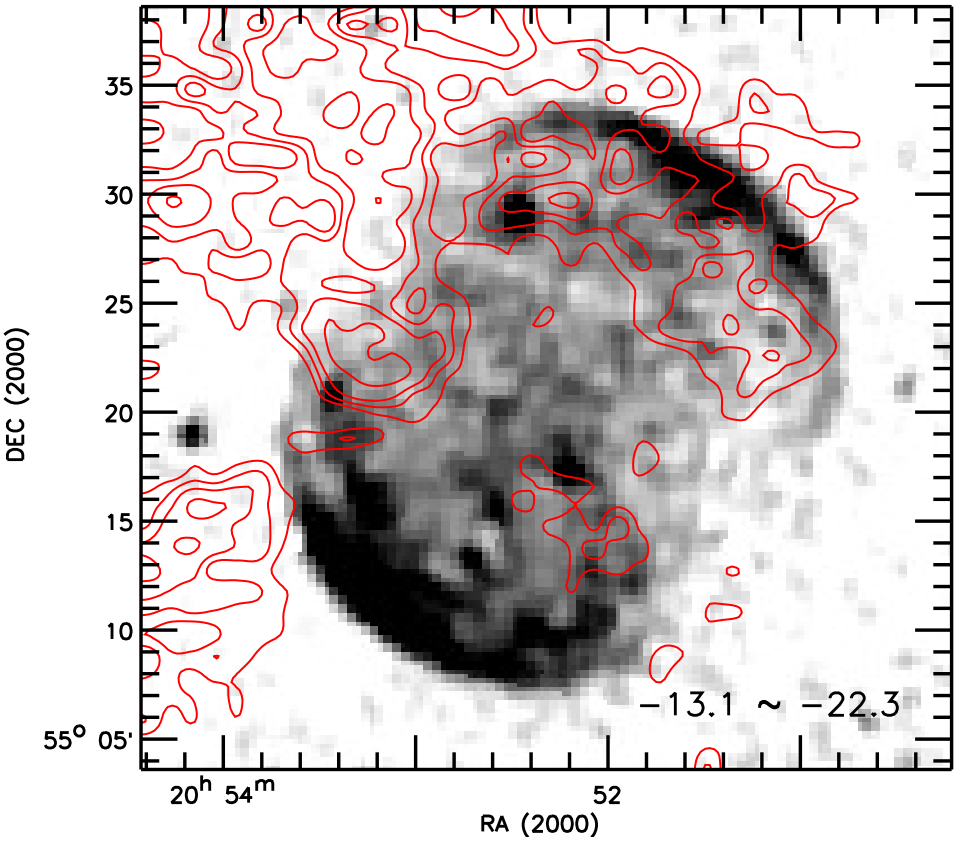

Figure 2.7 ^{12}CO $J = 1-0$ average intensity maps of G93.3+6.9 (contour levels: 1.1, 1.3, 1.5, 1.8 K). The gray-scale image is the WENSS 325 MHz radio continuum image (scale range: 9.5∼14 Jy/beam) (Rengelink et al. 1990).

et al. 2006). An HI observation suggested that a HI stellar wind bubble at 4.5 kpc is surrounding the remnant and that the progenitor could be an O4 star (Foster 2005). By using ROSAT data, he showed that bright, thermal hard X-ray emission was detected toward the radio bright region with good correlation. An OH maser observation was made toward the remnant with negative results (Frail et al. 1996).

We detected molecular gas over a wide velocity range from -70 to -40 km s^{-1} and from -20 to $+20$ km s^{-1} (Fig. 2.1). The positive velocity components ($v_{\rm LSR} \geq 0$ km s^{-1}) and large negative velocity components ($v_{\rm LSR} \leq -40$ km s^{-1}) do not show any correlated feature between the MCs and the radio continuum emission. We note that there is clear anti-correlation between the CO and radio distribution at ~ -13 km s^{-1} (Fig. 2.8). The large CO cloud is located in the western area of the weak radio continuum region with well-defined spatial correlation. Such anti-correlation is considerably similar to the case of the SNR G109.1$-$1.0 (CTB109), for which the interaction of the SNR with the molecular cloud occurs (Tatematsu et al. 1987, 1990; Sasaki et al. 2006). A detailed study on the interaction between the molecular cloud and the SNR will be reported in a separate paper (Jeong et al. 2012). If the molecular cloud at -13 km s^{-1} were associated with the SNR, the distance to the SNR would be about 3.0 kpc.

2.3.8 G166.2+2.5 (OA184)

G166.2+2.5 is a large radio source with low radio surface brightness, and it was known as an evolved SNR (Willis 1973). However, this source has been recently classified as an HII region based on its flat radio spectral index, missing X-ray emission, and non-significant polarization (Foster et al. 2006). Huang & Thaddeus (1986) noted that OA 184 is located $\sim 2^\circ$ west of VRO 45.05.01 and suggested that both of them are associated with a molecular cloud complex at $v_{\rm LSR} = -22$ km s^{-1}. The cloud complex is located between the two sources and its velocity is coincident with the velocities of the $H\alpha$ emission lines detected toward them (Lozinskaya 1981). Routledge et al. (1986) suggested that an HI feature at a $v_{\rm LSR}$ of -30 km s^{-1} in the

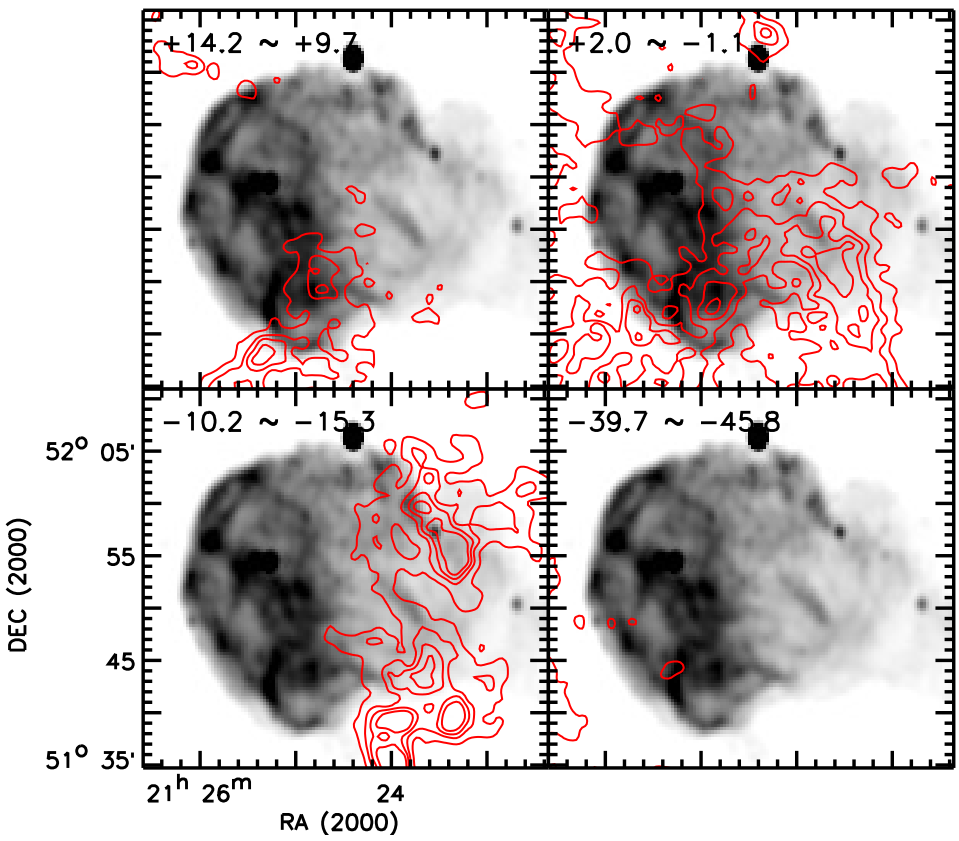

Figure 2.8 ^{12}CO $J = 1{-}0$ average intensity maps of G94.0+1.0 (contour levels: 0.8, 1.5, 2, 2.5 K). The gray-scale image is the CGPS 1420 MHz radio continuum image (scale range: 8∼14 K).

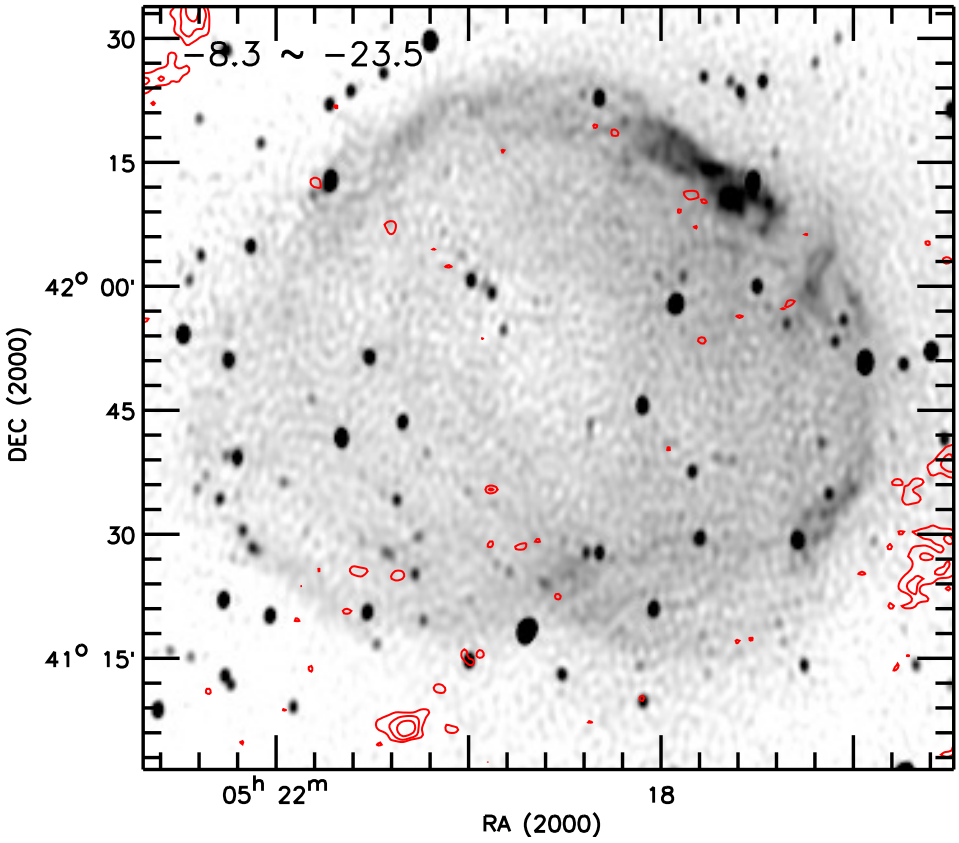

Figure 2.9 ^{12}CO $J = 1-0$ average intensity maps of G166.2+2.5 (contour levels: 0.9, 1.3, 1.8 K). The gray-scale image is the CGPS 1420 MHz radio continuum image (scale range: 4.6∼6 K).

southwest is probably associated with the source. OH maser observation was made toward the remnant with a negative result (Frail et al. 1996).

We detected a few small ($\leq 5'$) CO clumps from -26 to -9 km s^{-1} (Fig. 2.1). These clumps are located $\sim 10'$ away from the radio boundary of the source in the southeast and southwest (Fig. 2.9). They do not show any correlated features with the remnant.

2.3.9 G179.0+2.6

G179.0+2.6 is a faint SNR with a diameter of about $70'$. Three bright radio spots near the center of the remnant are radio galaxies along the line of sight (Fuerst et al. 1986; 1989).

CO emission toward this remnant is extremely weak, as shown in Fig. 2.1. Only one molecular cloud with a $5'$ diameter is detected at ~ -12 km s^{-1} (Fig. 2.10). This cloud lies near the southwest radio boundary; however, no signature of the SNR-MC interaction is observed.

2.3.10 G180.0−1.7 (S147)

G180.0−1.7 has large angular size of $\sim 3^\circ$ and remarkable optical filaments (van den Bergh et al. 1973). Anderson et al. (1996) discovered a pulsar $40'$ away from the center to the west. The age of the pulsar is estimated to be $3 \pm 0.4 \times 10^4$ yr (Kramer et al. 2003). No OH maser emission was detected toward the remnant (Frail et al. 1996).

We found some molecular clouds at velocities from ~ -14 to $+5$ km s^{-1} (Fig. 2.1). Fig. 2.11 shows the average intensity map from -14.8 to $+7.6$ km s^{-1}. The cloud at ~ -11 km s^{-1} is located $15'$ away toward the southeast from the radio boundary. CO emission at ~ -5 km s^{-1} is detected near the radio filaments in the south and shows filamentary and clumpy morphology. The cloud at $\sim +1$ km s^{-1} is located in the western part of the remnant where radio brightness is very faint. Although we detected molecular clouds near the SNR, none of them show correlated features

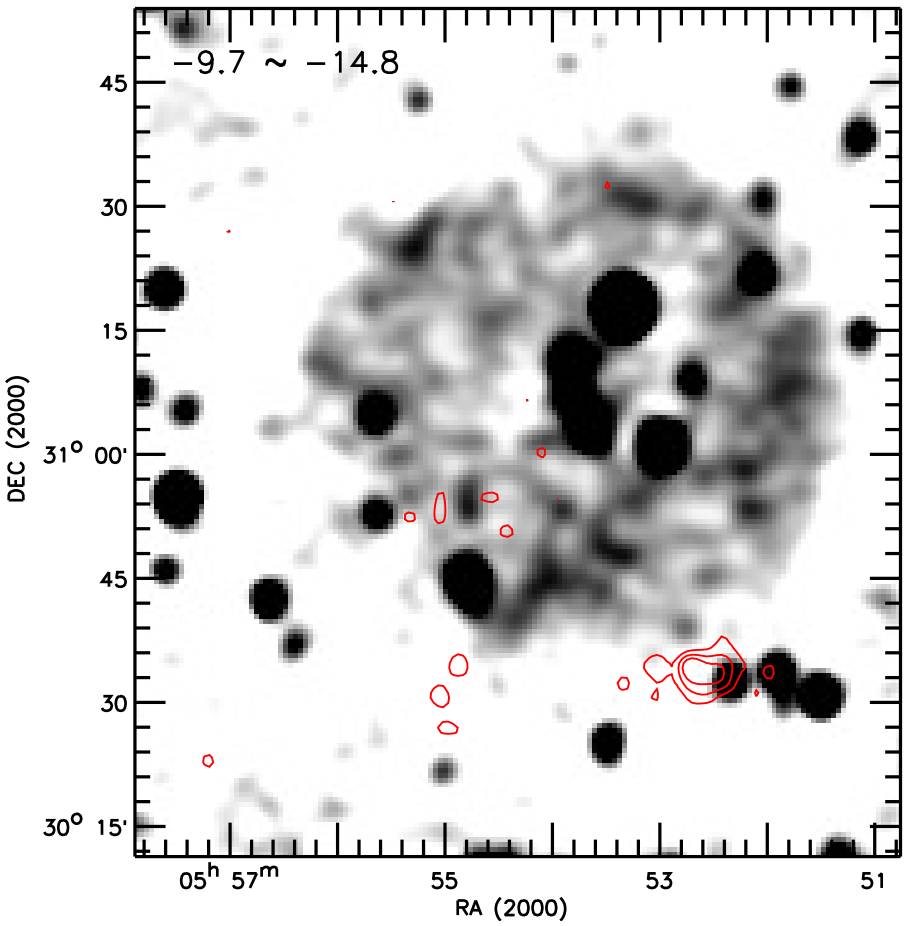

Figure 2.10 ^{12}CO $J = 1-0$ average intensity maps of G179.0+2.6 (contour levels: 0.4, 0.8, 1.2 K). The gray-scale image is the WENSS 325 MHz radio continuum image (scale range: 0.5∼8 mJy/beam).

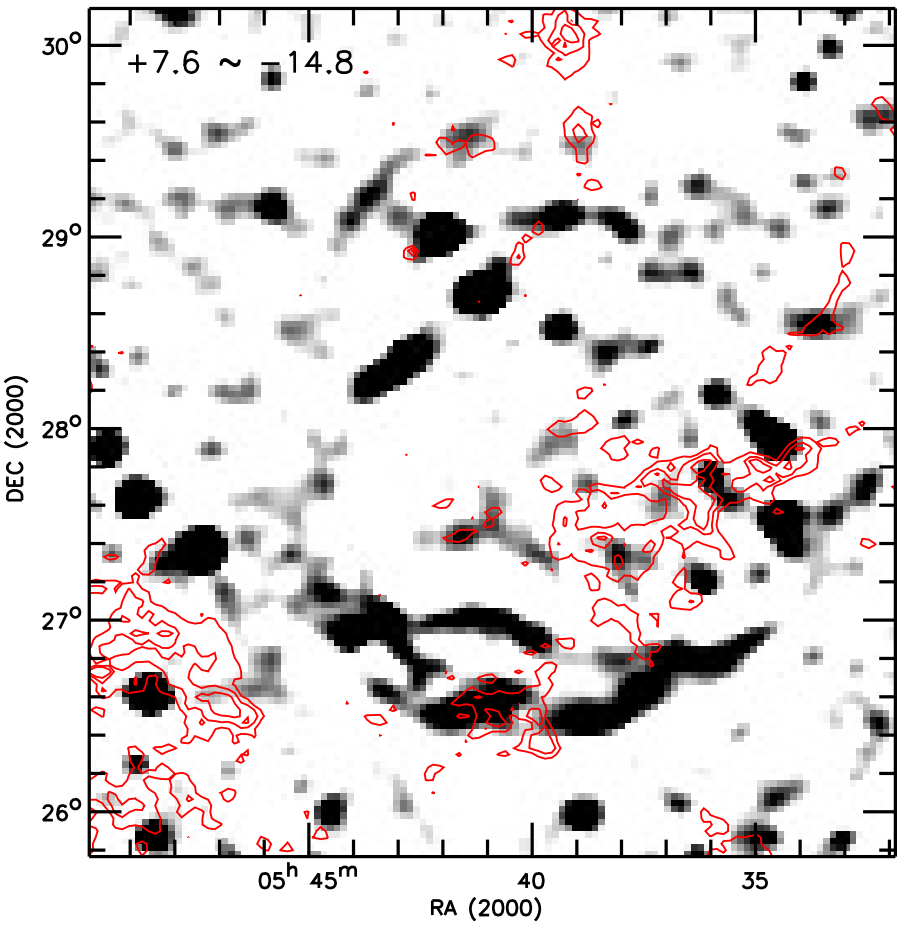

Figure 2.11 ^{12}CO $J = 1-0$ average intensity maps of G180.0−1.7 (contour levels: 0.4, 0.8, 1.2 K). The gray-scale image is the GB6 4850 MHz radio continuum image (scale range: 1.7∼6.3 mJy/beam) (Condon et al. 1994).

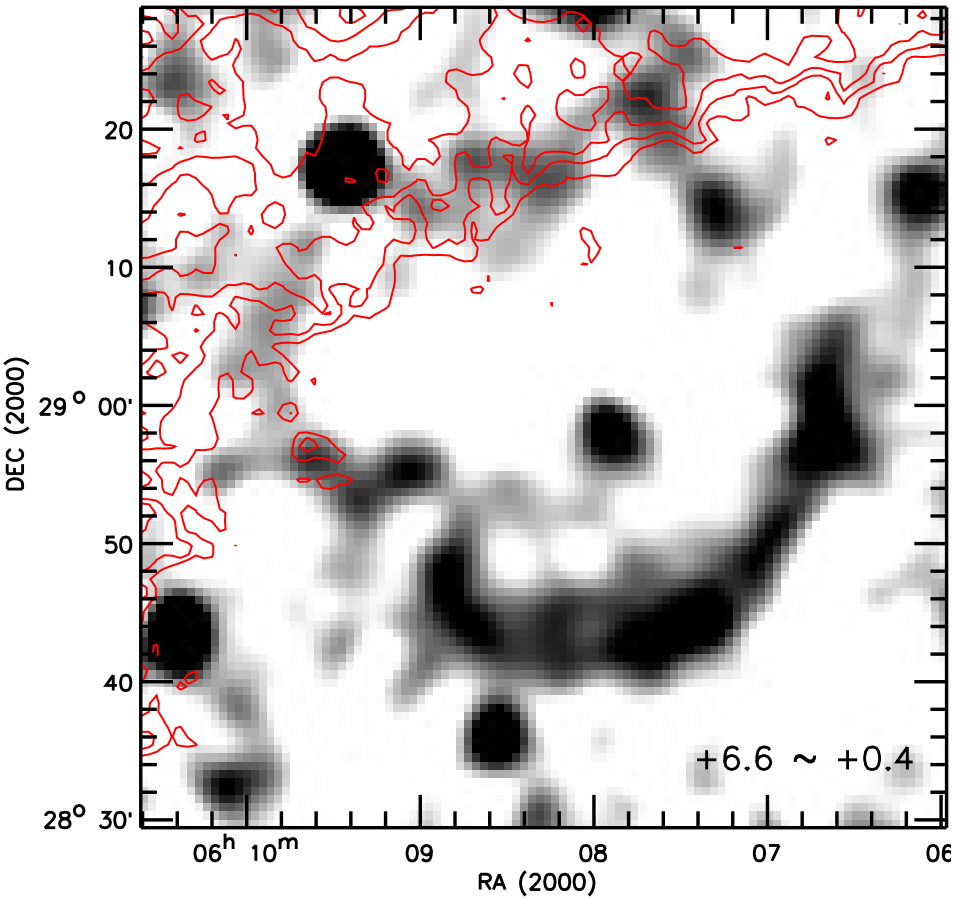

Figure 2.12 ^{12}CO $J = 1-0$ average intensity maps of G182.4+4.3 (contour levels: 0.5, 0.8, 1.1, 1.5 K). The gray-scale image is the GB6 4850 MHz radio continuum image (scale range: 0.38∼9 mJy/beam).

with the remnant.

2.3.11 G182.4+4.3

G182.4+4.3 is a shell-type SNR with a highly polarized, bright partial shell in the southwest (Kothes et al. 1998). The southern shell is bright and circular, whereas the northern shell is faint and flattened. No X-ray emission was detected toward the SNR.

We detected CO emissions at velocities from -9 to $+10$ km s^{-1} (Fig. 2.1). Most CO emissions arise outside the north and northeast shell of the remnant where the radio brightness is significantly fainter than that of the south shell. The boundary of the molecular cloud at $\sim +4$ km s^{-1} matches well with the radio boundary of the remnant (Fig. 2.12). It is possible that the molecular cloud is blocking the remnant, although no direct evidence for their interaction has been detected.

Table 2.3 Summary of Results

Supernova Remnant	CO velocity[a] (km/s)	Kinematic distance[b] (kpc)	Note
G73.9 +0.9	+3	···	Extended, filamentary MC across the northern part of the remnant along the east-west direction.
G76.9 +1.0	···	···	Large cloud across the SNR from southeast to northwest, but no obvious spatially-correlated features.
G84.2 −0.8	−17	4.9	Semi-circular CO cloud coincident with the western SNR boundary with enhanced radio brightness.
G85.4 +0.7	−41	7.2	Long, filamentary MC along the southwestern boundary of the SNR, connected to the compact HII region G84.9+0.5 in the south.
G85.9 −0.6	···	···	Several MCs in the field, but no obvious spatially-correlated features.
G93.3 +6.9	−2	···	Large, diffuse MC surrounding the northeast boundary of the SNR.
G94.0 +1.0	−13	3.0	Large molecular clouds blocking the western part of the SNR where the radio emission is faint.
G166.2 +2.5	···	···	Several small molecular clumps outside the SNR boundary.
G179.0 +2.6	···	···	Small molecular clumps in the southern part of the SNR, but no obvious spatially-correlated features.
G180.0 −1.7	···	···	Small MCs in the central area of the SNR without any correlation.
G182.4 +4.3	+4	···	Large, diffuse MC just outside the northwestern boundary of the SNR.

[a]Velocity of the CO emission that is spatially-correlated with the SNR.

[b]Kinematic distances corresponding to the CO velocity assuming the rotation curve of Brand & Blitz (1993). For small CO velocities, no kinematic distances have been derived.

2.4 Summary

We carried out ^{12}CO $J = 1-0$ line survey of SNRs using the SRAO 6-m telescope. We observed 11 SNRs between $l = 70°$ and 190°: G73.9+0.9, G76.9+1.0, G84.2−0.8, G85.4+0.7, G85.9−0.6, G93.3+6.9 (DA530), 94.0+1.0 (3C434.1), 166.2+2.5 (OA184), 179.0+2.6, 180.0−1.7 (S147), and G182.4+4.3. The mapping is performed either in half-beam or full-beam sampling to cover the full extents of individual SNRs in the radio continuum. The total number of spectra is about 45,000. We summarize our main results below:

1. We found CO molecular clouds having spatial correlations with radio emission in six SNRs: G73.9+0.9, G84.2−0.8, G85.4+0.7, G93.3+6.9, G94.0+1.0, and G182.4+4.3. However, no strong evidence for the interaction, e.g., broad wings or high-velocity shocked gas, was detected for these objects. We did not detect molecular clouds having any obvious spatial correlation with radio emission in the other SNRs. Table 2.3 summarizes the results in which the second column lists the velocities of the possibly associated CO features and their kinematic distances. The fourth column gives a short summary on individual SNRs.

2. Two SNRs are particularly interesting. In G85.4+0.7, there is a well-defined filamentary molecular cloud that matches well with the southern boundary of the SNR at -41 km s^{-1}. Another interesting SNR is 3C434.1. It has molecular clouds in the western part of the SNR, where the radio emission is weak. Such anti-correlation between a molecular cloud and radio emission was previously found in the SNR CTB109 (G109.1−1.0), and the their association is likely. Further observations are needed to confirm the interaction between molecular clouds and these SNRs.

Bibliography

Abdo, A. A., Ackermann, M., Ajello, M., et al. 2009, ApJ, 706, L1

Acciari, V. A., Aliu, E., Arlen, T., et al. 2009, ApJ, 698, L133

Aharonian, F. et al. 2008, A&A, 490, 685

Anderson, S.B., Cadwell, B.J., Jacoby, B.A., Wolszczan, A., Foster, R.S., & Kramer, M. 1996, ApJ, 468, L55

Brand, J., & Blitz, L. 1993, A&A, 275, 67

Byun, D.-Y. "Development of the SRAO 6-meter Telescope Control System and Molecular Line Observation of Supernova remnants" 2004, PhD thesis, Seoul National University

Byun, D.-Y., Koo, B.-C., Tatematsu, K. & Sunada, K. 2006, ApJ, 637, 283

Case, G.L., & Bhattacharya, D. 1998, ApJ, 504, 761

Chen, Y., Su, Y., Slane, P., & Wang, Q. D. 2004, ApJ, 616, 885

Choi, H.-K., Byun, D.-Y., & Koo, B.-C. 2003, International Journal of Infrared and Millimeter Waves, 24, 683

Claussen, M.J., Frail, D.A., Goss, W.M., & Gaume, R.A. 1997, ApJ, 489, 143

Condon, J.J., Broderick, J.J., Seielstad, G.A., Douglas, K. & Gregory, P.C. 1994, AJ, 107, 1829

DeNoyer, L.K. 1979, ApJ, 228, L41

Elitzur, M. 1976, ApJ, 203, 124

Feldt, C., & Green, D.A., 1993, A&A, 274, 421

Foster, T. 2005, A&A, 441, 1043

Foster, T.J., Kothes, R., Kerton, C.R., & Arvidsson, K., 2007, ApJ, 667, 248

Foster, T., Kothes, R., Sun, X.H., Reich, W. & Han, J.L. 2006, A&A, 454, 517

Foster, T., & Routledge, D. 2003, ApJ, 598, 1005

Frail, D.A., Goss, W.M., Reynoso, E.M., Ciacani, E.B., Green, A.J., & Otrupcek, R., 1996, AJ, 111, 1651

Fuerst, E., & Reich, W. 1986, A&A, 154, 303

Fuerst, E., Reich, W., Kuhr, H., & Stickel, M. 1989, A&A, 223, 66

Gaensler, B.M. 1998, ApJ, 493, 781

Green, D.A. 2004, Bulletin of the Astronomical Society of India, 32, 335

Green, D.A. 2009, Bulletin of the Astronomical Society of India, 37, 45

Higgs, L.A., Landecker, T.L. & Roger, R.S. 1983, AJ, 88, 97

Huang, Y.-L., & Thaddeus, P. 1986, ApJ, 309, 804

Jackson, J.M. et al. 2006, ApJS, 163, 145

Jeong, I.-G., Koo, B.-C., Cho, W.-K., Kramer, C., Stutzki, J. & Byun, D.-Y. 2013, ApJ, 770, 105

Jiang, B., Chen, Y., & Wang, Q.D. 2007, ApJ, 670, 1142

Jiang, B., Chen, Y., Wang, J., Su, Y., Zhou, X., Safi-Harb, S., & DeLaney, T. 2010, ApJ, 712, 1147

Koo, B.-C. 2003, Shocked Atomic and Molecular Gas in Supernova Remnants (ASP Conf. Ser. **289**), ed. S. Ikeuchi, J. Hearnshaw, & T. Hanawa (San Francisco: ASP), 199

Koo, B.-C., Park, Y.-S., Hong, S.-S., Yun, H.-S., Lee, S.-G., Byun, D.-Y., Lee, J.-W., Choi, H.-K., Lee, S.-S., Yoon, Y.-Z., Kim, K.-T., Kang, H.-W., & Lee, J.-E. 2003, JKAS , 36, 43

Kothes, R., Fedotov, K., Foster, T.J. & Uyaniker, B. 2006, A&A, 457, 1081

Kothes, R., Fuerst, E., & Reich, W. 1998, A&A, 331, 661

Kothes, R., Landecker, T.L., Foster, T., & Leahy, D.A. 2001a, A&A, 376, 641

Kothes, R., Reich, W., Foster, T. & Byun, D.-Y. 2003, ApJ, 588, 852

Kothes, R., Uyaniker, B. & Pineault, S. 2001b, ApJ, 560, 236

Kramer, M., Lyne, A.G., Hobbs, G., Lohmer, O., Carr, P., Jordan, C., & Wolszczan, A. 2003, ApJ, 593, L31

Landecker, T.L., Higgs, L.A., Roger, R.S., 1985, AJ, 90, 1082

Landecker, T.L., Higgs, L.A. & Wendker, H.J. 1993, A&A, 276, 522

Landecker, T.L., Routledge, D., Reynolds, S.P., Smegal, R.J., Borkowski, K.J., & Seward, F.D. 1999, ApJ, 527, 866

Lee, J.-W., Han, S.-T., Byun, D.-Y., Koo, B.-C., & Park, Y.-S. 2002, International Journal of Infrared and Millimeter Waves, 23, 47

Lee, J.-J., Koo, B.-C., Snell, R. L., Yun, M. S., Heyer, M. H., & Burton, M. G. 2012, ApJ, 749, 34

Lee, J.-J., Koo, B.-C., Yun, M. S., Stanimirović, S., Heiles, C., & Heyer, M. H. 2008, AJ, 135, 796

Lockett, P., Gauthier, E., & Elitzur, M. 1999, ApJ, 511, 235

Lozinskaya, T.A. 1981, SvAL, 7, 17

Matthews, H.E. & Shaver, P.A. 1980, A&A, 87, 255

Pineault, S., Gaumont-Guay, S., & Madore, B. 1996, AJ, 112, 201

Reich, W., Fuerst, E., Reich, P., Sofue, Y., & Handa, T. 1986, A&A, 155, 185

Reach, W.T. & Rho, J. 1999, ApJ, 511, 836

Rengelink, R.B., Tang, Y., de Bruyn, A.G., Miley, G.K., Bremer, M.N., Roettgering, H.J.A. & Bremer, M.A.R. 1997, A&AS, 124, 259

Routledge, D., Landecker, T.L., & Vaneldik, J.F. 1986, MNRAS, 221, 809

Sasaki, M., Kothes, R., Plucinsky, P.P., Gaetz, T.J. & Brunt, C.M. 2006, ApJ, 642, L149

Snell, R.L., Hollenbach, D., Howe, J.E., Neufeld, D.A., Kaufman, M.J., Melnick, G.J., Bergin, E.A., & Wang, Z. 2005, ApJ, 620, 758

Tatematsu, K., Fukui, Y., Iwata, T., Seward, F.- D., & Nakano, M. 1990, ApJ, 351, 157

Tatematsu, K., Fukui, Y., Nakano, M., Kogure, T., Ogawa, H. & Kawabata, K. 1987, A&A, 184, 279

Taylor, A.R., et al. 2003, AJ, 125, 3145

van den Bergh, S., Marscher, A.P., & Terzian, Y. 1973, ApJS,26, 19

Wardle, M. 1999, ApJ, 525, L101

Wardle, M., & Yusef-Zadeh, F. 2002, Science, 296, 2350

Willis, A.G. 1973, A&A, 26, 237

Chapter 3

CO J=1−0 and J=2−1 Line Observations of the Molecular Cloud - Blocked Supernova Remnant 3C434.1

3.1 Introduction

[1] Supernova remnants (SNRs) appear usually spherical when they are young. Historical SNRs such as Cassiopeia A, Tycho, and Kepler are good examples. As they evolve, however, their morphology can deviate considerably from sphericity by their interaction with the ambient medium. If the SNR encounters, for example, a dense molecular cloud, the SNR shell becomes distorted. In contrast, if the remnant crosses a diffuse bubble, then part of the SNR shell could blow out or could even be completely missing. Therefore, from the morphology of SNRs, we can infer their environments, which are often useful for understanding the nature and evolution of SNRs.

[1]This chapter is published in the Astrophysical Journal, 2013, 770, 105

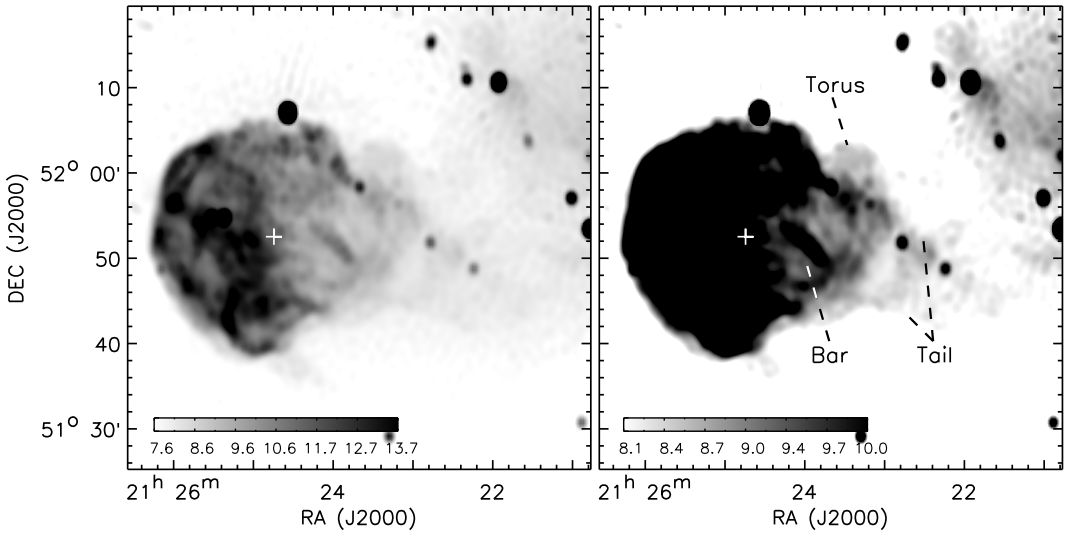

Figure 3.1 Radio continuum image of 3C434.1 at 1420 MHz from the Canadian Galactic Plane Survey data (Taylor et al. 2003). The two frames show the same image with different gray scales to emphasize the detailed radio continuum structure. The central white cross represents the geometrical center of the remnant. The features discussed in the text are labeled.

The SNR 3C434.1 (G94.0+1.0) is a shell-like supernova remnant with a distinct morphology in radio (Willis 1973; Goss et al. 1984; Landecker et al. 1985; Foster 2005; see Fig. 3.1). It has a bright eastern hemisphere which has a well-defined, circular boundary. The limb brightening indicates that we are seeing the eastern half of a spherical shell with a radius of $13'$. The complex filaments projected inside the remnant implies that the shell is not uniform. The circular shell-like structure continues a little further to the west, but then the morphology becomes quite complex. Some noticeable features are as follows: (i) a linear, convergent, thin "tail" that originates out from the western end of the shell and extends much further ($\sim 20'$) to the west, (ii) a "torus" that appears to be composed of several ring structures surrounding the connecting portion of the tail and the SNR shell, and (iii) a $8'$-long "bar" that is located near the center of the torus and extends roughly parallel to the tail. We discuss these features later in this paper.

Foster et al. (2004) explored the atomic environment of the SNR using Canadian Galactic Plane Survey (CGPS) HI 21 cm-line data. They noted fragmented HI filaments along the SNR boundary and interpreted them as parts of preexisting stellar wind bubble produced by the massive progenitor of the SNR. They developed a dynamical model for the SNR and its wind bubble based on this scenario. The kinematic distance to the HI filaments (10 kpc), however, yielded unreasonable parameters, and thus, they instead adopted the distance to the Perseus spiral arm (5.2 kpc) as the distance to the SNR. Later, Foster (2005) carried out follow-up multiwavelength studies in radio to X-rays. He analyzed the archival ROSAT X-ray data to show that the X-ray emission is bright and centrally-brightened in the eastern part of the SNR and that the X-ray spectrum can be fitted with a single-temperature thermal plasma model. The derived temperature and density of the X-ray emitting plasma were 4.5×10^6 K and 0.2 cm^{-3}, respectively, with a revised distance of 4.5 ± 0.5 kpc. He also detected Hα emission correlated with the radio structure along the southeastern boundary of the SNR.

In this paper, we present the results of our CO study of 3C434.1 which gives a

picture of the SNR significantly different from the previous HI studies. We found a large molecular cloud in contact with the western boundary of the SNR. The cloud was originally identified by Huang & Thaddeus (1986) in their low-resolution ($\sim 30'$) CO survey of SNRs; however, no follow-up studies have been made. We present strong evidence for the interaction of the SNR with the molecular cloud, and we argue that the western part of the SNR is faint and complicated because the remnant is interacting with the cloud there. We derive the physical parameters of 3C434.1 based on the new kinematic distance (3 kpc) and discuss the variation of radio spectral index and the origin of the distinct radio features.

3.2 Observations

^{12}CO $J = 1-0$ (115.2712 GHz) observations were carried out from November 2003 to December 2003 using the Seoul Radio Astronomy Observatory (SRAO) 6-m telescope. The FWHM beam size at 100 GHz was $120''$and its main beam efficiency was 70% (Koo et al. 2003). We used a 100 GHz SIS mixer receiver with single-side band filter and a 1024-channel auto-correlator with a 50 MHz bandwidth for front-end and back-end, respectively.

We mapped the $41' \times 39'$ (R.A. $\times$ Dec.) area centered at ($21^{\rm h}24^{\rm m}50^{\rm s}$, $51^\circ53'00''$) with $1'$ grid spacing by using the position switching mode. The velocity coverage was from -95 to $+35$ km s^{-1}. The off-position was located at ($21^{\rm h}22^{\rm m}28^{\rm s}$, $51^\circ40'00''$). The system temperature ranged from 500 to 800 K depending on the elevation and weather condition. The typical rms noise level was ~ 0.3 K at 0.5 km s^{-1} resolution. Each spectrum was integrated over 30 s. The relative calibration accuracy had been checked by observing bright standard sources near the target every one or two hours. Pointing accuracy was better than $20''$.

^{12}CO $J = 2-1$ (230.5380 GHz) follow-up line observations were performed in December 2004 using the 3-m telescope at the Kölner Observatorium für Sub-Millimeter Astronomie (KOSMA). We used a dual-channel SIS receiver (Graf et al. 1998) and

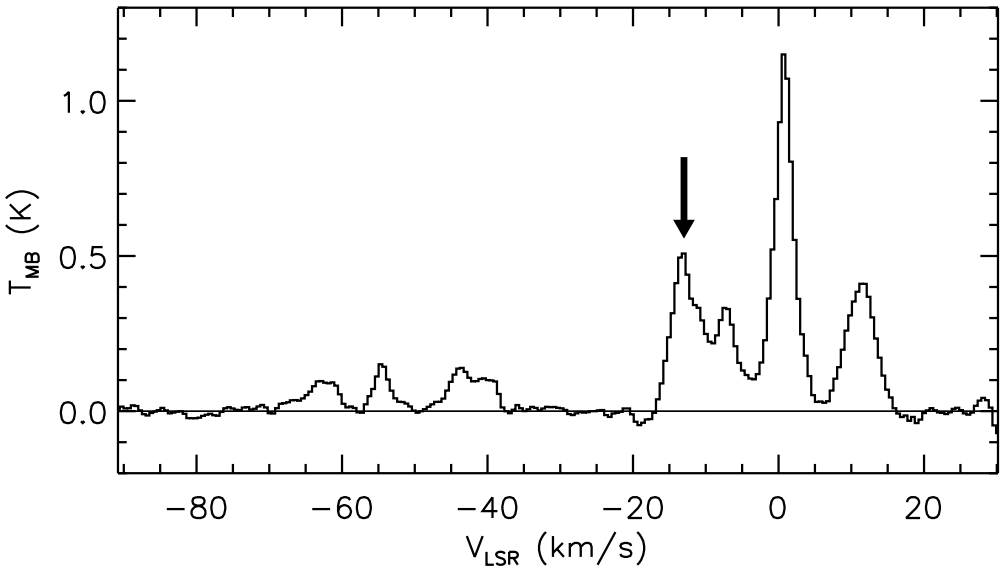

Figure 3.2 SRAO ^{12}CO $J = 1-0$ average spectrum of 3C434.1. The arrow marks the -13 km s^{-1} component associated with the SNR.

acousto-optical spectrometers (Schieder et al. 1989) for front-end and back-end, respectively. The beam width and main beam efficiency were 130″ and 68%, respectively. Pointing accuracy was better than 10″. We have mapped an area of 20′ × 37′ using the position-switched on-the-fly (OTF) mode with a grid spacing of 50″. The OFF position was ($21^{\rm h}35^{\rm m}39^{\rm s}.1$, $52^\circ42'59''$). The velocity resolutions was 0.2 km s^{-1} and the typical rms noise level was $\sim$ 0.3 K.

The data were reduced by using CLASS[2] software, which is part of the Gildas package for single-dish spectral line analysis developed by Grenoble and IRAM. Usually the baseline was fitted with a second-order polynomial, but for some spectra we used a third-order polynomial too.

3.3 Results

3.3.1 SRAO ^{12}CO $J = 1$–0

Several molecular clouds are detected in the velocity range covered by our observations. Figure 3.2 shows the average spectrum of the area: several velocity components are apparent; bright components between -20 and $+20$ km s^{-1} and faint components between -70 and -35 km s^{-1}.

Figure 3.3 shows the channel maps of the prominent velocity components. The components at large negative velocities ($-70 \sim -35$ km s^{-1}) are located outside the remnant; the -44 km s^{-1} cloud is located a few arc minutes beyond the southeast boundary. The -55 and -61 km s^{-1} molecular clouds are located close to the SNR boundary, but their intensities are very weak and line widths are narrow. Thus, we consider it unlikely, that these features have any relation with the remnant. The positive velocity ($v_{\rm LSR} \geq 0$ km s^{-1}) components are associated with the complex local clouds of Cep OB2 and Cyg OB7 at 0.8 kpc (Humphreys 1978). These clouds are located in the southern part of the field, and we do not find any correlated features with the radio continuum emission.

[2]http://www.iram.fr/IRAMFR/GILDAS

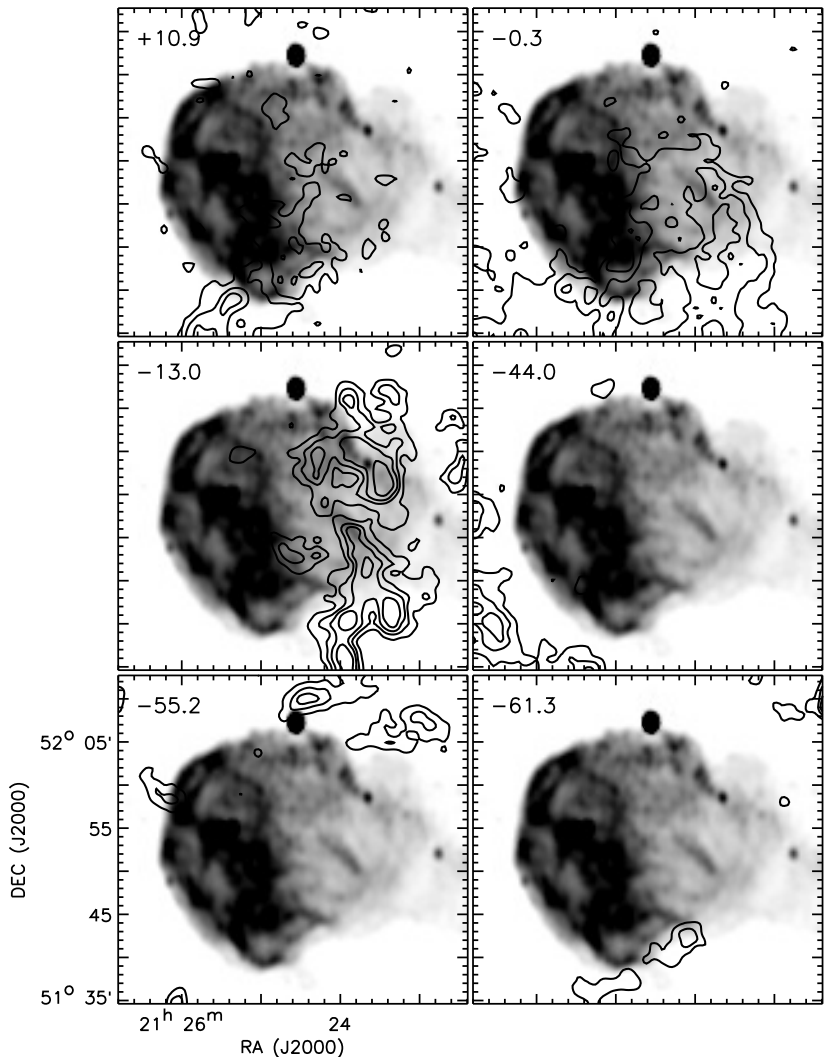

Figure 3.3 SRAO ^{12}CO $J = 1-0$ contoured channel maps of prominent velocity components. Individual frames show single channel maps of width = 0.5 km s^{-1}. Velocity centers are marked at the top left corners. The contour levels are 0.9, 2, 3, and 4.5 K in brightness temperature. The gray-scale image in each channel map is the CGPS 1420 MHz radio continuum image of 3C434.1.

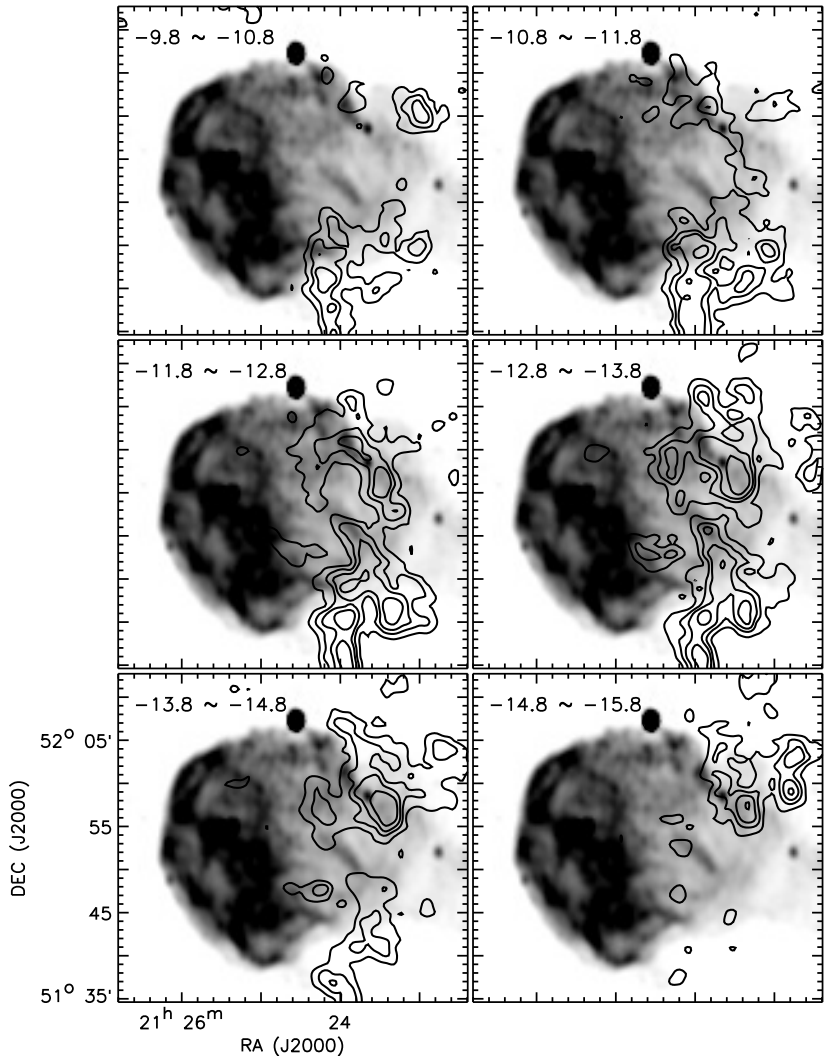

Figure 3.4 Detailed SRAO ^{12}CO $J = 1-0$ channel maps of 3C434.1 from -10.0 to -15.6 km s^{-1}. Each frame shows intensity distributions averaged over two channels or 1.0 km s^{-1}. Contour levels are 0.9, 2, 3 and 4.5 K in brightness temperature. The Gray-scale is the CGPS 1420 MHz radio continuum image.

It is the -13 km s^{-1} cloud that shows a clear spatial correlation with the radio continuum emission. The cloud is widely distributed over the western part of the remnant where the radio continuum intensity is low. Figure 3.4 compares the distributions of the CO and radio continuum intensities in detail from $v_{\rm LSR} = -9.8$ to -15.8 km s^{-1}. The cloud is elongated vertically along the western boundary of the remnant. At -11.8 to -12.8 km s^{-1}, the southern part of the cloud is bright and there is a thin filamentary structure that matches well with the western boundary of the torus structure in the radio continuum. The bright CO region matches well with the southern curved edge of the radio continuum. At -12.8 to -13.8 km s^{-1}, the northern and southern parts of the cloud are about equally bright and there is emission along the bar structure in the radio continuum.

The above morphological correlation between the CO and radio continuum strongly suggests that the CO cloud is interacting with the SNR and that the complex radio morphology of the SNR is caused by this interaction. We estimate the mass of the western molecular cloud by integrating the CO emission over $v_{\rm LSR} = -8$ to -18 km s^{-1} in an area of $23' \times 39'$ and assuming a Galactic CO-to-H_2 conversion factor of 2.3 $\times 10^{20}$ cm^{-2} (K km s^{-1})$^{-1}$ (Strong et al. 1988). The resulting mass is $(1.00 \pm 0.02) \times 10^4\ d_3^2\ M_\odot$ where d_3 is the distance to the SNR normalized to 3 kpc (see § 4.1) and the error is 1σ rms error.

3.3.2 KOSMA ^{12}CO $J = 2$–1

A high ^{12}CO $J = 2$-1/1-0 ratio identifies shocked warm and dense CO gas. Figure 3.5 shows the spatial variation of the ^{12}CO $J = 2$-1/1-0 ratio obtained from the SRAO ^{12}CO $J = 1$–0 and KOSMA ^{12}CO $J = 2$–1 maps integrated over $v_{\rm LSR} = -16$ to -8 km s^{-1} and binned to $2' \times 2'$. We exclude pixels with an integrated intensity less than 2.5 K km s^{-1} in order to exclude positions with low S/N ratios from the map. In Figure 3.5, high (≥ 1.0) ratios are found toward the southern molecular cloud. The spectra of this area are shown in Figure 3.6. Note that the 0 km s^{-1} component shows $J = 2$–1 emission weaker than the $J = 1$–0 emission with ^{12}CO J=2–1/J=1–0 ratio

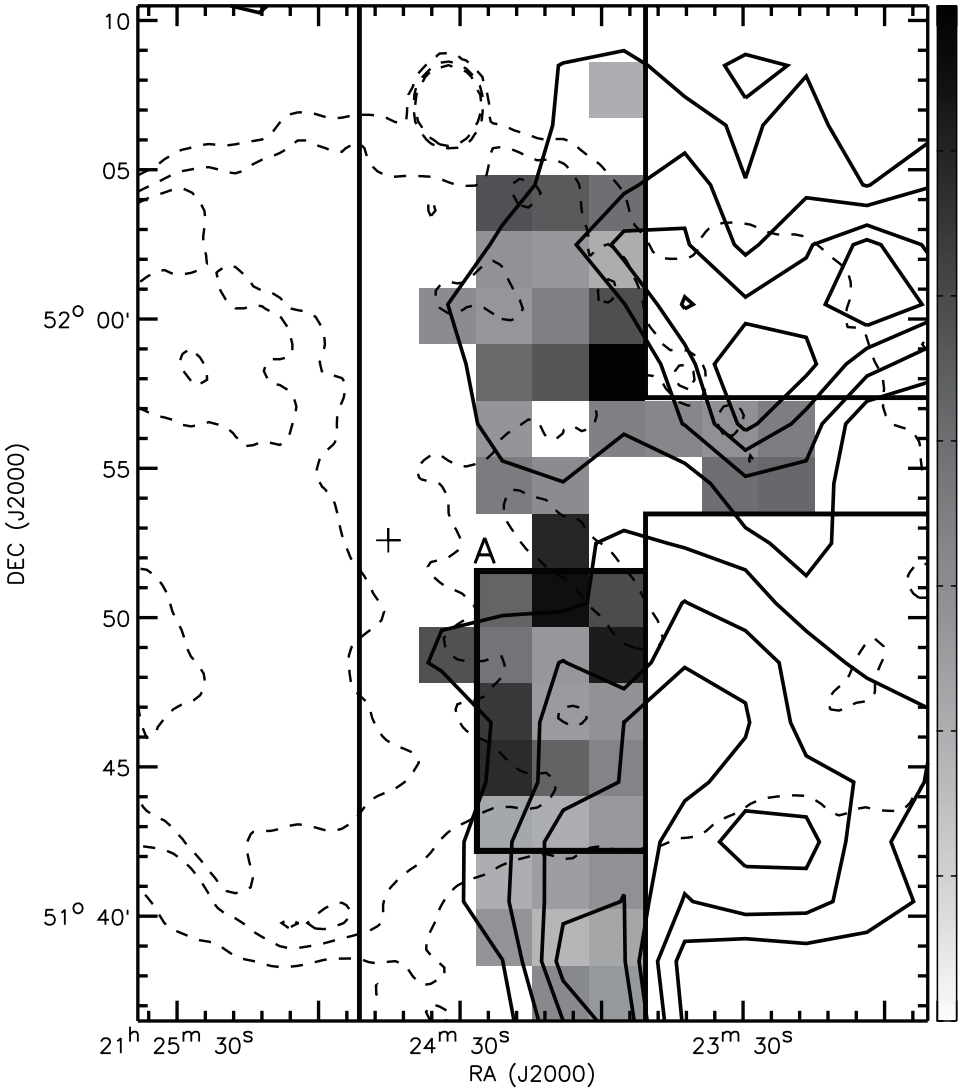

Figure 3.5 ^{12}CO $J = 2{-}1/1{-}0$ ratio map in gray scale. The gray scale varies linearly from 0.1 to 1.8 with the darker scale for the higher ratios. The dashed contours represent the 1420 MHz radio continuum emission of the SNR (contour levels: 8.2, 10, and 12 K in brightness temperature). The solid contour is the SRAO ^{12}CO $J = 1{-}0$ integrated intensity map from $v_{\rm LSR} = -16$ to -8 km s^{-1} (levels: 4, 8, 12, 15 $\times$ 1 K km s^{-1}). The bold line marks the area observed with KOSMA ^{12}CO $J = 2{-}1$.

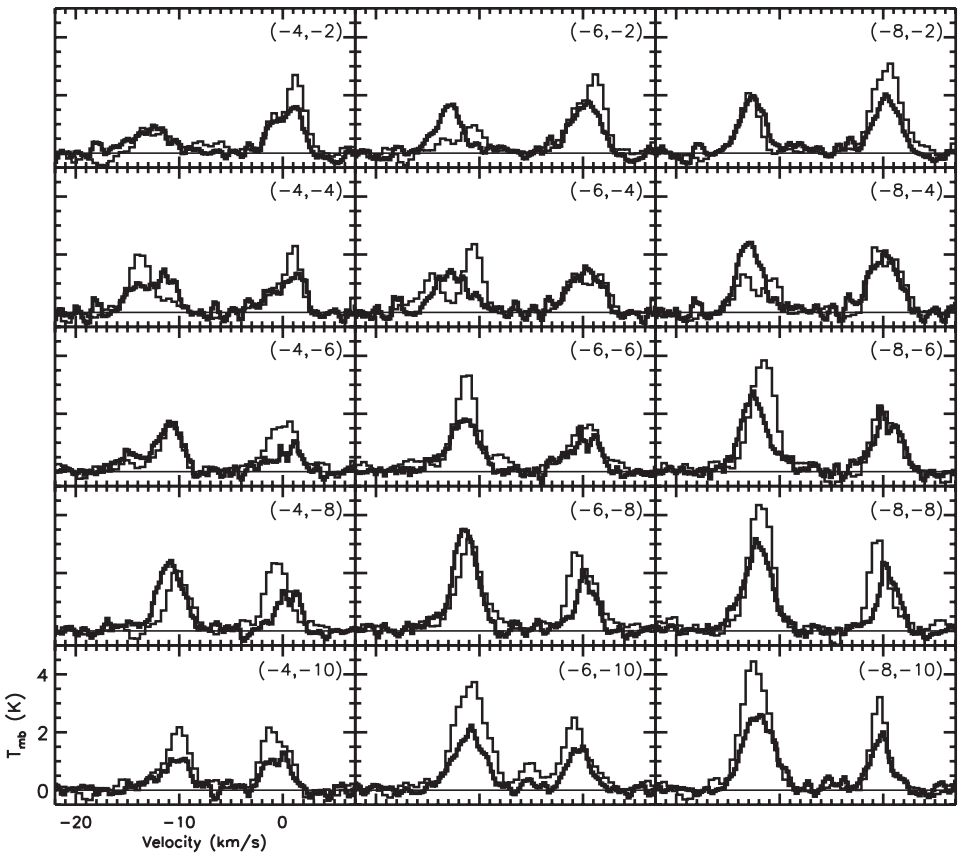

Figure 3.6 CO molecular line spectra of SRAO $J = 1{-}0$ (thin lines) and KOSMA $J = 2 - 1$ (thick lines) at region A of Fig. 3.5. The positions of the spectra are marked in each frame as coordinates relative to the geometrical center of the remnant, ($21^{\mathrm{h}}24^{\mathrm{m}}45^{\mathrm{s}}$, $51^{\circ}52'27''$).

of 0.3 to 1.0 which is typical for giant molecular clouds (Sakamoto et al. 1994). The position $(-4, -10)$ also shows an example of ordinary CO line profiles of unshocked molecular clouds between -16 and -8 km s^{-1}. Here, the ratio is 0.5 at a velocity of -11 km s^{-1}. On the other hand, the -13 km s^{-1} component has a higher J=2–1/J=1–0 ratio. The ^{12}CO J=2–1/J=1–0 integrated intensity ratio varies from 0.5 to 1.6 in region A in Figure 3.5 and the highest value (1.6) is at ($21^{\rm h}24^{\rm m}8^{\rm s}$, $51°50'30''$) or at $(-6, -2)$ in Figure 3.6. Typically, the high ratio regions are located at the boundary of the southern molecular clouds with the peak velocity of -13 km s^{-1}. However, at position $(-4, -4)$, only the -11 km s^{-1} velocity component shows the high ratio CO line emissions. The ratio is 0.95 at this position using CO integrated intensity results.

A ratio higher than ~ 1 indicates the presence of warm and dense CO gas, presumably heated and compressed by the SNR shock (e.g., Koo et al. 2001). We use the large velocity gradient (LVG) model (Scoville & Solomon 1974; Goldreich & Kwan 1974) to estimate the physical parameters of the shocked gas. Using $\mathrm{T}_{mb,J=1-0} = 0.5$ K and $^{12}\mathrm{R}_{2-1/1-0} = 1.6$ at the $(-6, -2)$ position, we obtain $n(\mathrm{H_2}) \sim 2.0 \times 10^3$ cm^{-3} and $X(^{12}\mathrm{CO})/(dv/dr) \sim 7.9 \times 10^{-8}$ pc (km s^{-1})$^{-1}$ for $\mathrm{T}_k = 100$ K where $X(^{12}\mathrm{CO})/(dv/dr)$ is the fractional abundance of ^{12}CO relative to $\mathrm{H_2}$ [$X(^{12}\mathrm{CO})$] per unit velocity gradient interval. This gives a CO column density of 2.4×10^{15} cm^{-2} assuming a velocity width of $\Delta v = 5$ km s^{-1}. This is valid when the emitting region fills the telescope beam (FWHM=130″). If the beam filling factor is lower, e.g., ~ 0.1, the source intrinsic brightnesses and the column density derived scale up by the inverse factor, i.e. by ~ 10, whereas the density, derived from the line ratio, stays roughly the same.

3.4 Discussion

3.4.1 New Distance to 3C434.1 and Its Physical Parameters

The morphological relation and the high $^{12}\mathrm{R}_{2-1/1-0}$ ratio strongly suggest that the SNR 3C434.1 is interacting with the molecular cloud that shows CO emission at -13 km s^{-1}. The kinematic distance corresponding to -13 km s^{-1} is 3.0 kpc assuming the Galactic rotation curve of Brand & Blitz (1993) with $R_0 = 8.5$ kpc and $v_0 = 220$ km s^{-1}. Our kinematic distance is less than the 4.5 ± 0.9 kpc distance proposed by Foster (2005).

Foster et al. (2004) noted fragmented HI filaments along the SNR boundary at -80 km s^{-1} and interpreted them as parts of a preexisting stellar wind bubble produced by the massive progenitor of the SNR. According to our result, however, the velocity difference is too large for this component to be associated with the SNR. We instead examine the correlation of the HI emission at around $v_{\mathrm{LSR}} = -13$ km s^{-1} with the SNR.

Figure 3.7 shows the CGPS HI channel maps from -9.7 to -15.5 km s^{-1}. We first note that there is a large-scale gradient in HI intensity over the field: The northwestern area is brighter than the southeastern area. Second, there is a large filamentary HI-absorption structure in the northwestern area of the field, but it is not related to the SNR. Absorption from the -13 km s^{-1} cloud interacting with the SNR is not apparent. Third, there is a long, linear HI structure just outside of, and along, the southern SNR boundary at velocities from -11 to -15 km s^{-1} (labelled "Filament S"). The radio brightness drops sharply across the HI filament. Therefore, the linearly-shaped southwestern radio boundary seems to be related to this HI structure.

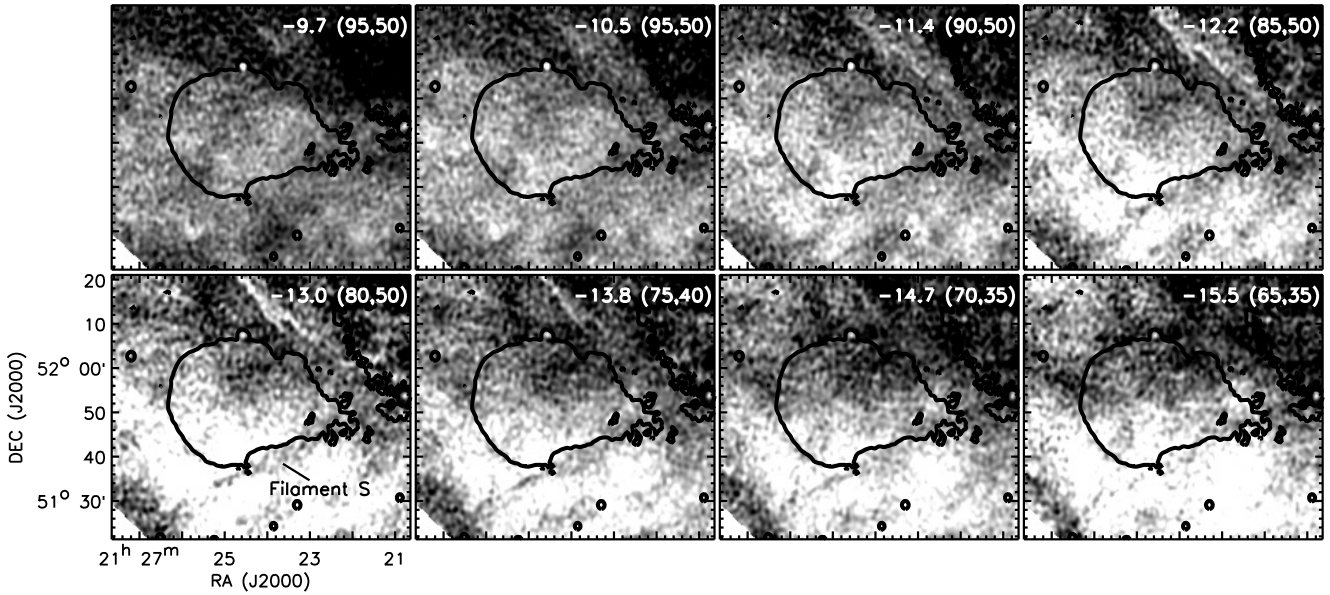

Figure 3.7 CGPS HI distribution of 3C434.1 from −9.7 to −15.5 km s^{-1} at 0.8 km s^{-1} separation. The gray scales are different for individual frames, and the maximum and minimum brightness temperatures of the scales (in Kelvins) are marked in individual frames in parentheses. The contour is the CGPS 1420 MHz radio continuum contour at 8 K.

The geometrical center of the shell is ($21^{\rm h}$ $24^{\rm m}$ $45^{\rm s}$, 51° $52'$ $27''$) and its radius (R_s) is $13'$ or 11.3 pc at 3.0 kpc. The spherical morphology suggests that we can apply standard model to this part of the remnant, as has been confirmed by hydrodynamic simulations (e.g., Tenorio-Tagle et al. 1985). From the ROSAT X-ray spectra, Foster (2005) derived an electron temperature of $T_e = 4.5 \times 10^6$ K for the host X-ray emitting gas, which corresponds to a shock speed $v_s = (16 k_B T_e/3\mu)^{1/2} = 570$ km s^{-1} (where $\mu = 1.4 m_{\rm H}/2.3 = 0.61 m_{\rm H}$ is the mean mass per particle, $m_{\rm H}$ = mass of H nuclei, and k_B is Boltzmann's constant). This speed is large and we may assume that the SNR is in its adiabatic phase. Then, from the Sedov solution, the radius and the velocity give an age of $0.4 R_s/v_s = 7,900$ yr. The estimated volume emission measure is $\int n_e^2 dV = 4.5 \times 10^{57}$ cm^{-6} pc^3 (scaled to 3.0 kpc). Foster (2005) assumed that this X-ray emission comes from a thin shell in contact with the stellar wind bubble. We instead assume that the X-ray emitting gas is roughly filling the eastern half because the X-ray emission is centrally brightened, which gives an rms electron density of 0.23 cm^{-3}. Then the SN explosion energy is, from the Sedov solution, $E_{SN} = 2.1 \times 10^{51} n_0 (R/10 \text{ pc})^3 (v_s/10^3 \text{ km s}^{-1})^2 = 0.19 \times 10^{51}$ ergs, where $n_0 (= n_e/1.2) = 0.19$ cm^{-3} is the number density of hydrogen nuclei of the medium taking into account an He abundance of 10% by number. This is smaller than the canonical value of 10^{51} ergs but not unreasonable. The derived parameters of the SNR are summarized in Table 3.1. The dynamical evolution of the SNR including the western part interacting with the molecular cloud will be discussed in § 4.3.

3.4.2 Variation of Radio Spectral Index

SNRs interacting with molecular clouds often show flattening or a turnover of the radio synchrotron spectrum at low frequencies around the areas of the interaction, i.e., the spectral index becomes larger than the typical value ($\alpha \sim -0.5$; $S_\nu \propto \nu^\alpha$) of shell-type SNRs or even becomes positive. Some examples are IC 443 (Green 1986), the Cygnus Loop (Leahy & Roger 1998), HB 21 (Koo et al. 2001; Leahy 2006), 3C391 (Brogan et al. 2005), and W44 (Castelletti et al. 2007). Several mechanisms

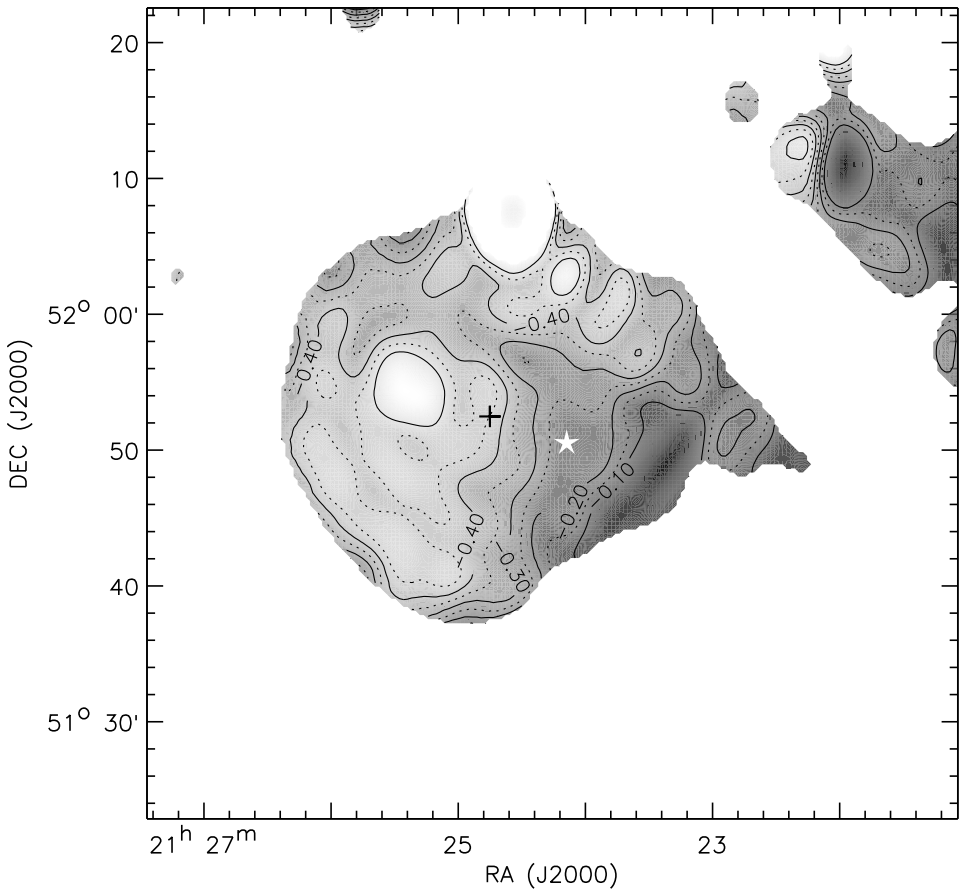

Figure 3.8 Spectral index map of 3C434.1. The spectral indices (α in $S_\nu \propto \nu^\alpha$) are derived only for the areas with 1420 and 408 MHz brightnesses larger than 1.2 K and 15.2 K corresponding to 5-σ brightnesses, respectively. The range of gray scale in α is from -0.6 to $+0.2$. The solid contours are drawn every 0.1 while the dotted contours are drawn every 0.05. The star symbol shows the location of the high CO ratio region.

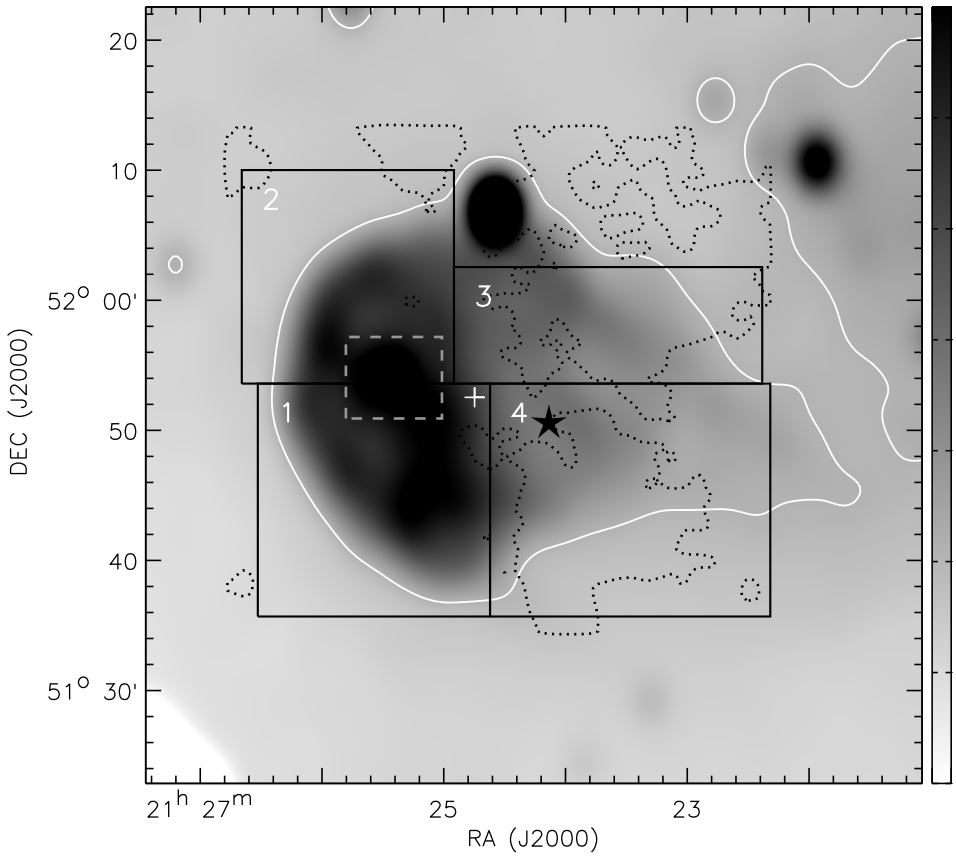

Figure 3.9 Convolved 1420 MHz radio continuum image of 3C434.1. The Gray scale varies linearly from 6 to 13 K with the darker scale for the higher temperatures. Boxes show the regions for the $T - T$ plots in Fig. 10. The dashed box represents the area excluded in the $T - T$ plots. The star symbol shows the location with high CO $J = 2 - 1/1 - 0$ ratio.

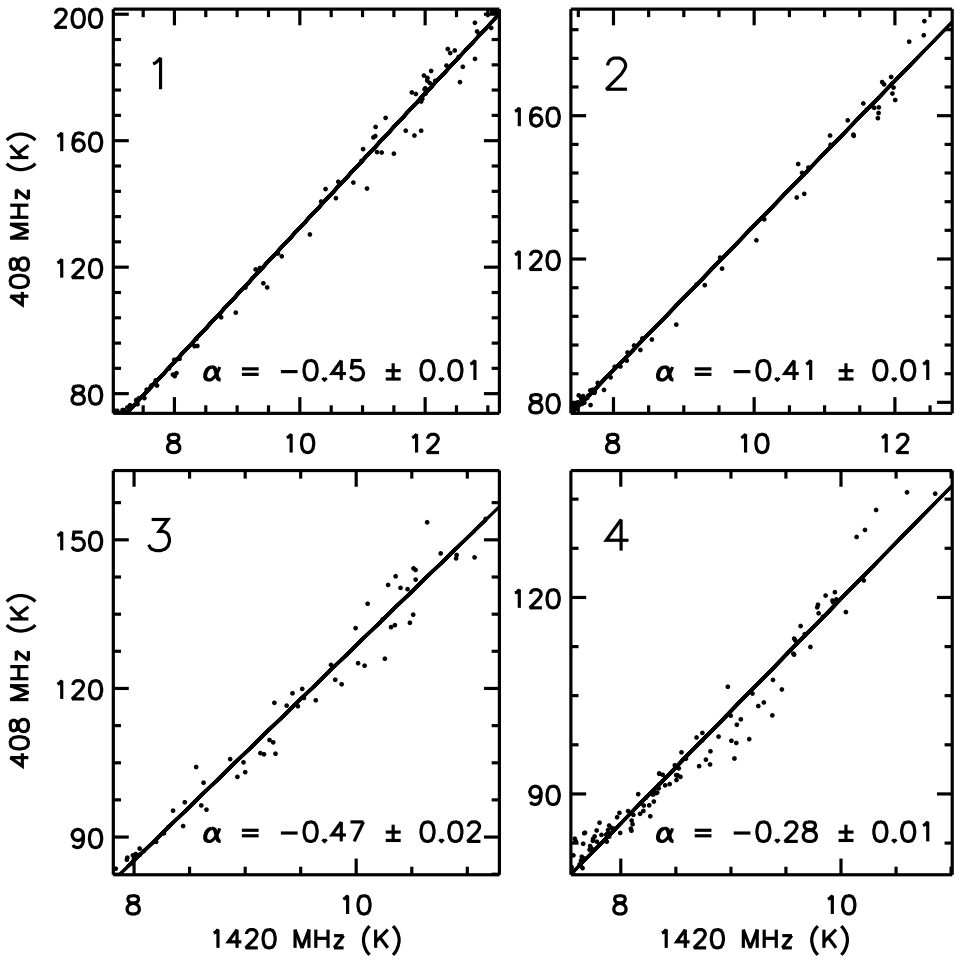

Figure 3.10 $T - T$ plot results of four regions obtained by pixel-to-pixel comparison of CGPS 408 and 1420 MHz radio continuum images.

Table 3.1 Physical parameters of SNR 3C434.1

Parameter	Value
Distance (kpc)	3.0
Radius of eastern shell (pc)	11.3
Age (yr)	7,900
Ambient hydrogen density (cm^{-3})	0.19
SN energy (ergs)	0.19×10^{51}
H_2 mass of interacting molecular cloud ($M_\odot$)	1.0×10^4

have been proposed for the flat radio spectrum: free-free absorption by thermal plasma in the dense postshock region, ionization losses from mixed dense molecular material, second-order Fermi acceleration by the turbulent medium in the postshock region (Leahy & Roger 1998; Ostrowski 1999), the higher compression ratio owing to the energy loss to cosmic ray particles (Bykov et al. 2000), and the relatively flat spectrum of ambient cosmic rays entering the shock (Chevalier 1999). For 3C434.1, Foster et al. (2004) derived a spectral index of -0.38 ± 0.03 from 150 MHz to 2.7 GHz and noted that the western extension has a slightly flatter spectrum (≤ 0.3) than the eastern radio shell. Later Kothes et al. (2006) derived a somewhat steeper index of -0.48 ± 0.02 by fitting the total fluxes from 30 MHz to 5 GHz.

We produce a spectral index map using the CGPS 1420 and 408 MHz radio continuum data. We first convolve the 1420 MHz image (FWHM=49″) to the beam size (168″) of the 408 MHz image, and we subtract a constant background in each image: 7.3 and 77 K for 1420 and 408 MHz, respectively. The resulting spectral index map is shown in Figure 3.8, which confirms the flat spectrum in the western area: The eastern bright area has an index of -0.45 to -0.3 whereas the southwestern area has -0.1 to 0.0. The area around ($21^{\rm h}\ 23^{\rm m}\ 20^{\rm s}$, $51^\circ\ 49'\ 10''$) has a particular flat spectrum (~ 0.0). The average spectral index of the entire SNR is -0.33.

We also derive the spectral index using the "T-T plot method", wherein we make a pixel-to-pixel comparison of the brightness temperatures at two different frequencies and derive the slope. The advantage of this method is that the slope is not affected by potentially different zero levels of each set of frequency data and smooth background emission (Turtle et al. 1962). We divide the target area into four regions and derive the index in each region from 1420 and 408 MHz data. Figure 3.9 shows the boundary of the four regions in the convolved 1420 MHz radio continuum image, and Figure 3.10 shows their pixel-to-pixel comparison of the brightness at two frequencies, respectively. The indices derived from least-squares fitting are given in the individual graphs. In three regions, the index varies little (-0.47 to -0.41), but in the southwestern area (region 4), the index is -0.28 ± 0.01 which is considerably

flatter than the other regions. This flat spectral index could be due to the interaction with the molecular cloud, confirming the reasoning given above. The average spectral index of all areas is -0.42 ± 0.01.

3.4.3 Interaction with the Molecular Cloud and Radio Morphology

The dynamical evolution of a SNR originating near the boundary of a dense molecular cloud has been numerically studied by several authors (e.g., Tenorio-Tagle et al. 1985; Wang et al. 1992; Ferreira & de Jager 2008). The details of the evolution depend on the physical and geometrical parameters of the simulation, e.g., the SN explosion energy, the densities of the molecular cloud and diffuse gas, the location of SN explosion site, etc. If the SN explodes in the diffuse medium close to the boundary of the molecular cloud, the SN blast wave expands adiabatically until it encounters the cloud. When the blast wave hits the dense cloud, two waves are produced: a shock wave propagating into the cloud and a reflected wave propagating back to the interior of the SNR. The propagating shock wave decelerates rapidly because of the high density and also because the reflective wave lowers the driving pressure near the cloud. Because the molecular cloud's density is considerably larger than that of the diffuse medium, it is not overly disrupted, and the SNR appears as a semicircular shell. The semicircular morphology of the SNR CTB 109, which is another SNR blocked by a molecular cloud (Tatematsu et al. 1987, 1990; Sasaki et al. 2006), has been acceptably explained by this scenario (Wang et al. 1992).

The SNR 3C434.1 also has a semicircular shape, but it does not quite fit into the above scenario: It has a narrow, convergent tail that originates from the western end of the shell and extends much further ($> 25'$ from the center) to the west. Also, there is a torus that appears to surround the western end of the tail. The inner boundary of the torus is quite circular with a clear limb brightening. This probably indicates that the cloud that is interacting with 3C434.1 is thin and that the blast wave has broken through it. This hypothesis is consistent with the presence of an elongated CO cloud along the western boundary of the SNR.

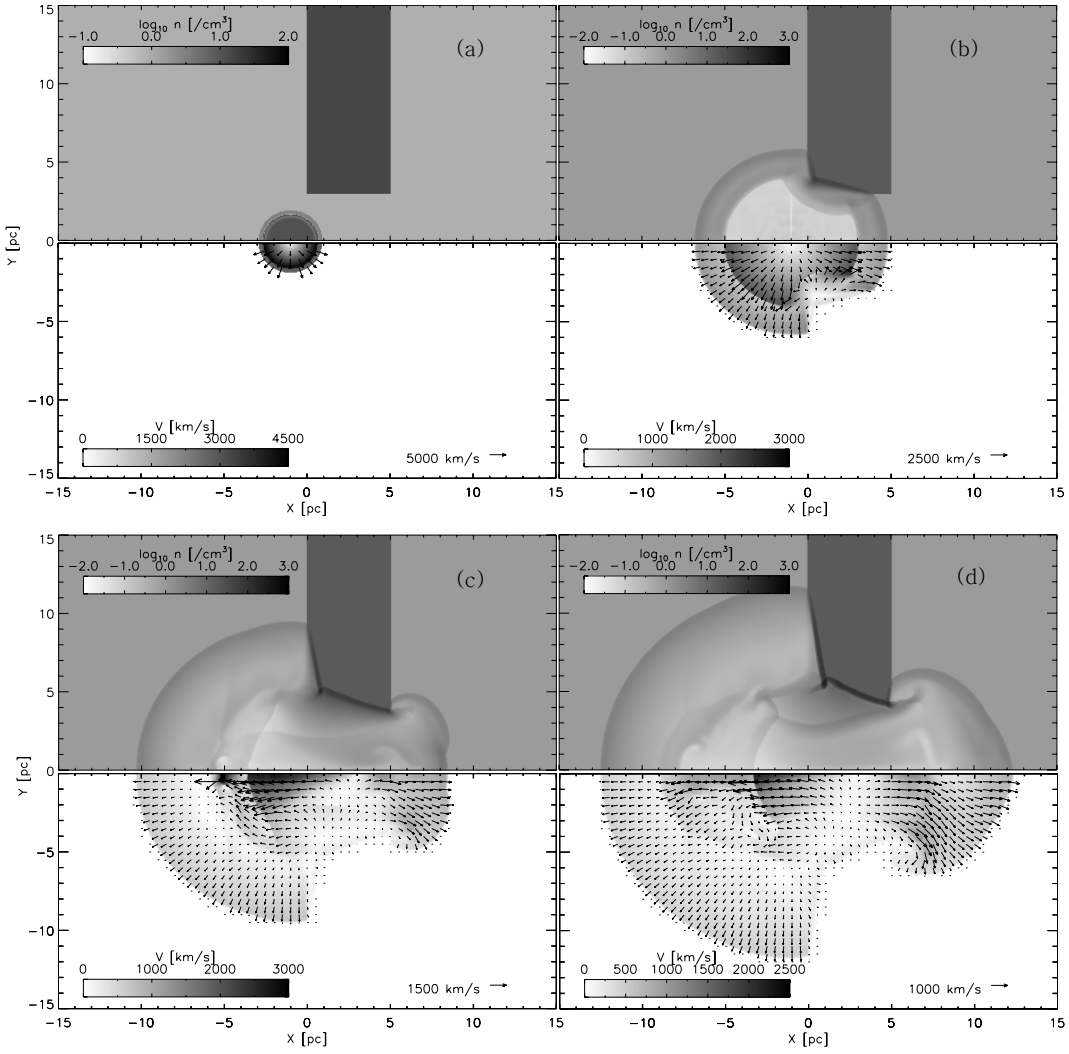

Figure 3.11 Hydrodynamic evolution model for 3C434.1. Frames from (a) to (d) show the density (upper panels) and velocity structures (lower) at different stages in the SNR evolution (t = 350, 1950, 4950 and 7950 yr, respectively). In the density panels, the color bars are shown in logarithmic units. In the velocity panels, arrows mark both the direction as well as the magnitude of the velocity field. The molecular cloud with a cylindrical hole of radius 3 pc is shown in dark gray on the density panel, but the molecular cloud and intercloud medium cannot be seen separately in the velocity panel, because their velocity distribution is assumed to be static.

We have developed a hydrodynamic model to confirm the above hypothesis. We assume that the SN explodes at 1 pc from the boundary of a sheetlike cloud that has a thickness of 5 pc. The H-nuclei number density of the cloud is assumed to be 20 cm^{-3}, which is a typical density for the interclump medium of giant molecular clouds (e.g. Chevalier 1999, and references therein). For the density of the diffuse medium and SN explosion energy, we adopt 1 cm^{-3} and 10^{51} ergs, respectively. These canonical values are both about 5 times larger than those of 3C434.1 but since the radius (and velocity) scales with $(E_{SN}/n)^{0.2}$ in the Sedov phase, the resulting morphological evolution in time should be approximately correct. The density distribution of a core-collapse SN is characterized by a central region of approximately constant density and an outer region with a steep gradient (e.g., Matzner & McKee 1999). We assume that the SN ejecta, which are freely expanding, are composed of a central region of constant density and an outer region with a steep power law ($\rho(r) \propto r^{-9}$) with a total mass of 8 $M_{\odot}$. When the steep power-law portion of the ejecta is interacting with the ambient medium, a similarity solution exists (Chevalier 1982). Our numerical simulation starts at $t = 350$ yr, and the distributions of the physical parameters at this time are taken from this similarity solution. We first considered a model in which the cloud was shaped like an infinitely extended disk. This model, however, did not produce the torus-like structure in the west in time. We therefore assume that the cloud has a cylindrical hole at the center, so that the shock can penetrate through the central hole. The radius of the hole is assumed to be 3 pc. For the calculation, we adopt the three-dimensional hydrodynamic code developed by Harten, Lax and van Leer (HLL) with a modified cooling effect (Harten et al. 1983). This HLL code is efficient for describing the shock propagation. The simulation box consists of $512 \times 256 \times 256$ grid points with a spatial resolution of 1/16 pc. We calculate one quadrant column along the symmetric axis (x-axis), and we copy the results to the other quadrants by assuming symmetry.

The results of the numerical simulations are shown in Figure 3.11 where we show the time evolution of the density and velocity distributions in the upper and lower

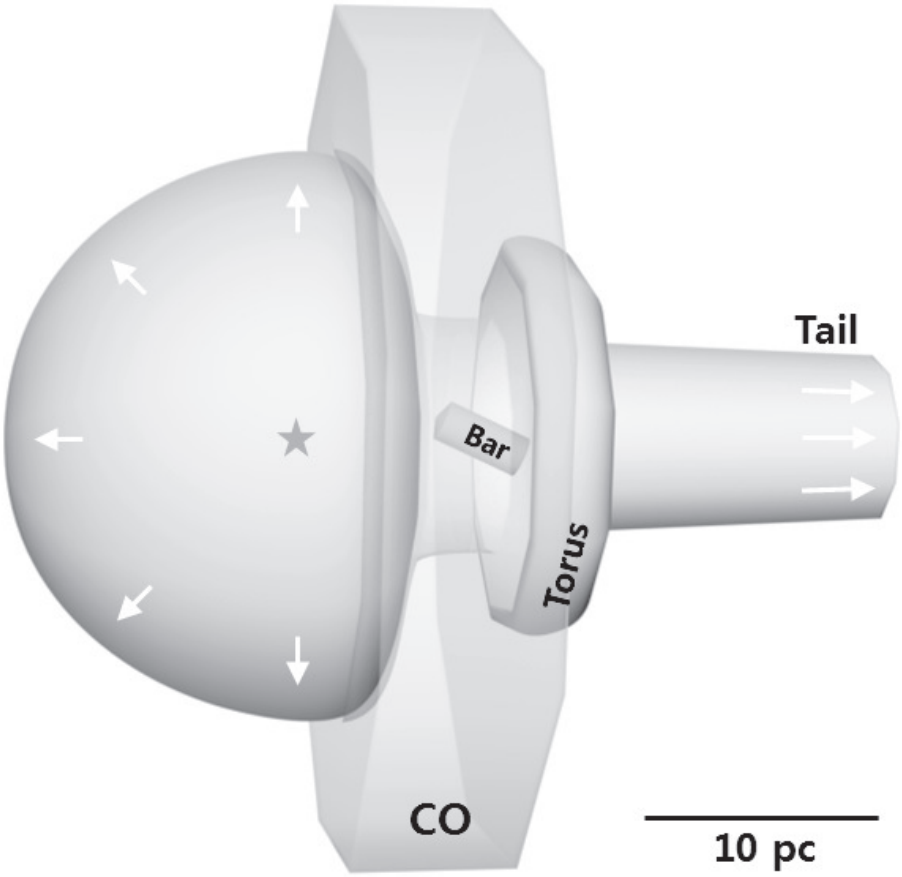

Figure 3.12 Schematic diagram of the SNR 3C434.1. The thin, disklike molecular cloud interacting with the SNR is labeled "CO". The pronounced radio continuum features (torus, bar, and tail) are also labeled. The asterisk symbol marks the position of the SN explosion.

panels, respectively. Figure 3.11 (a) shows the initial distributions at $t = 350$ yr. The ambient shock is at 1.89 pc, while the reverse shock propagating into the SN ejecta is at 1.60 pc from the explosion center. Between these two shocks, the shocked ambient medium and the shocked ejecta are separated by a contact discontinuity which is at 1.66 pc (see Chevalier 1982). At $t = 1,950$ yr (Fig. 3.11(b)), the SNR blast wave propagating to the right has been significantly distorted by the interaction with the cylindrical wall of the cloud. The cloud boundary has been compressed to high density while the shock propagating into the dense cloud is considerably decelerated. Note that the reverse shock in the interacting region is now propagating backward into the central area in the rest frame, whereas the reverse shocks in the other regions are still propagating forward in the rest frame. At $t = 4,950$ yr (Fig. 3.11(c)), the radius of the left-half of the SNR becomes 9.4 pc, which is close to that of the Sedov solution, as expected. Meanwhile, the blast wave propagating to the right has propagated through the cylindrical hole and popped out of the cloud producing a mushroom-like structure. In the interior, the reverse shocks from the side walls collide and produce a fast flow to the east. At $t = 7,950$ yr (Fig. 3.11(d)), which is close to the age of 3C434.1, again the radius of the left-half of the SNR agrees with that (11.3 pc) of the Sedov solution. The blast wave on the right by now appears almost spherical. Note that the velocity of the blast wave on the right is larger than on the left, so that the distance to the rightmost front from the explosion center is more than 13 pc. The density and velocity distributions in the interior of the SNR become complex owing to the collision of waves and hydrodynamic instabilities. Meanwhile, the shock propagating into the dense cloud became partially radiative, so that the density of the shocked cloud is very high ($\sim 10^3$ cm^{-3}).

The resulting morphology of the numerical simulation is close to the radio morphology of 3C434.1 but there are some differences. In Figure 3.12, we draw a schematic diagram of 3C434.1 including its radio-continuum features, i.e., torus, bar, and tail. The spherical eastern half of the SNR with a radius of 11 pc is quite consistent with the hydrodynamic model. The torus structure partly matches the

mushroom structure in the model. The shocked, highly-compressed boundary of the molecular cloud corresponds to the northwestern SNR boundary with enhanced radio brightness in the radio map. The bar structure represents the dense swept-up cloud material embedded within the SNR. The long, radio-continuum tail that extends much further than the overall radius of the SNR, however, is not easy to explain. It seems to indicate that there might have been a preexisting tunnel of much lower density in the ISM. An interesting possibility would be a "star trail" as in the Crab Nebula (Blandford et al. 1983; Cox et al. 1991). In the Crab nebula, there is a thin (~ 0.5 pc) jetlike structure in the radio continuum to the north, and it was attributed to the trail of the progenitor star; the progenitor star was moving before the explosion and its red supergiant wind leaves a trail through which the SN blast wave can propagate beyond. In 3C434.1, the radius of the tail is wide, i.e., $5'$ or ~ 4.4 pc just behind the torus. However, if the trail is filled with hot, shocked gas, the trail will expand sideways at about the velocity of the sound speed of the hot gas, which is 250 km s^{-1} for 4.5×10^6 K X-ray emitting gas, the maximum increment of the radius of the tunnel by the SNR would be < 2 pc. Therefore, the tunnel might have had a large radius initially.

3.5 Conclusion

We observed ^{12}CO $J = 1$–0 and $J = 2$–1 emission lines toward the SNR G94.0+1.0 (3C434.1) using the SRAO and KOSMA telescopes. The presence of a molecular clouds around the SNR had been known from the previous low-resolution ($30'$) survey, but the relation between the two had not been investigated. Our observations reveal a thin molecular cloud elongated along the north-south direction superposed on the western part of the SNR. The spatial correlation of the CO emission with the radio continuum structure together with its high ^{12}CO $J = 2$–1/1–0 line ratio strongly suggests that the cloud is interacting with the SNR. The relatively flat radio spectral index may also be due to the interaction. The systemic velocity of the

cloud is -13 km s^{-1}, which yields a new kinematic distance of 3 kpc to the SNR. The new distance implies that 3C434.1 is located within the Perseus spiral arm. This, together with the interaction with the molecular cloud suggests that 3C434.1 is likely a remnant of a core-collapse supernova that had a massive ($\geq$8 $M_{\odot}$) stars as its progenitor.

Our result indicates that the distinct radio morphology of 3C434.1 is due to the interaction with a dense, blocking cloud in the west. Indeed the spatial correlation between the CO and radio continuum features is remarkable. Features such as the torus, bar, and tail must reflect different efficiencies of particle acceleration depending on the shock speed, ambient density, and magnetic field strength. Currently, strong evidence exists for 45 SNRs, which indicates their interaction with molecular clouds according to the compilation by Jiang et al. (2010), which covers 16% of the known Galactic SNRs (see also Jeong et al. 2012). 3C434.1 is one such prototypical SNR in this category, and future high-resolution observations and hydromagnetic simulations will give us a better understanding of this intriguing SNR.

Bibliography

Blandford, R. D.,Kennel, C. F., McKee, C. F., & Ostriker, J. P. 1983, Nature, 301, 586

Brand, J., & Blitz, L. 1993, A&A, 275, 67

Brogan, C. L., Lazio, T. J., Kassim, N. E., & Dyer, K. K. 2005, AJ, 130, 148

Bykov, A. M., Chevalier, R. A., Ellison, D. C., & Uvarov, Y. A. 2000, ApJ, 538, 203

Castelletti, G., Dubner, G., Brogan, C., & Kassim, N. E. 2007, A&A, 471, 537

Chevalier, R. A. 1982, ApJ, 258, 790

Chevalier, R. A. 1999, ApJ, 511, 798

Cox, C. I., Gull, S. F., & Green, D. A. 1991, MNRAS, 250, 750

Ferreira, S. E. S., & de Jager, O. C. 2008, A&A, 478, 17

Foster, T. 2005, A&A, 441, 1043

Foster, T., Routledge, D., & Kothes, R. 2004, A&A, 417, 79

Goldreich, P., & Kwan, J. 1974, ApJ, 189, 441

Goss, W. M., Mantovani, F., Salter, C. J., Tomasi, P., & Velusamy, T. 1984, A&A, 138, 469

Graf, U. U., Honingh, C. E., Jacobs, K., Schieder, R., & Stutzki, J. 1998, Astronomische Gesellschaft Meeting Abstracts, 14, 120

Green, D. A. 1986, MNRAS, 221, 473

Harten, A., Lax, P. D., & van Leer, B. 1983, SIAMR, 25, 35

Huang, Y.-L., & Thaddeus, P. 1986, ApJ, 309, 804

Humphreys, R. M. 1978, ApJS, 38, 309

Jeong, I.-G., Byun, D.-Y., & Koo, B.-C. et al. 2012, Ap&SS, 342, 389

Jiang, B., Chen, Y., & Wang, J. et al. 2010, ApJ, 712, 1147

Koo, B.-C., Park, Y.-S., & Hong, S. S. et al. 2003, J. Korean Astron. Soc., 36, 43

Koo, B.-C., Rho, J., Reach, W. T., Jung, J., & Mangum, J. G. 2001, ApJ, 552, 175

Kothes, R., Fedotov, K., Foster, T. J., & Uyanıker, B. 2006, A&A, 457, 1081

Landecker, T. L., Higgs, L. A., & Roger, R. S. 1985, AJ, 90, 1082

Leahy, D. A. 2006, ApJ, 647, 1125

Leahy, D. A., & Roger, R. S. 1998, ApJ, 505, 784

Matzner, C. D., & McKee, C. F. 1999, ApJ, 510, 379

Ostrowski, M. 1999, A&A, 345, 256

Sakamoto, S., Hayashi, M., Hasegawa, T., Handa, T., & Oka, T. 1994, ApJ, 425, 641

Sasaki, M., Kothes, R., Plucinsky, P. P., Gaetz, T. J., & Brunt, C. M. 2006, ApJ, 642, L149

Schieder, R., Tolls, V., & Winnewisser, G. 1989, Exp. Astron., 1, 101

Scoville, N. Z., & Solomon, P. M. 1974, ApJ, 187, L67

Strong, A. W., Bloemen, J. B. G. M., & Dame, T. M. et al. 1988, A&A, 207, 1

Tatematsu, K., Fukui, Y., Iwata, T., Seward, F. D., & Nakano, M. 1990, ApJ, 351, 157

Tatematsu, K., Fukui, Y., & Nakano, M. et al. 1987, A&A, 184, 279

Taylor, A. R., Gibson, S. J., & Peracaula, M. et al. 2003, AJ, 125, 3145

Tenorio-Tagle, G., Bodenheimer, P., & Yorke, H. W. 1985, A&A, 145, 70

Turtle, A. J., Pugh, J. F., Kenderdine, S., & Pauliny-Toth, I. I. K. 1962, MNRAS, 124, 297

Wang, Z., Qu, Q., Luo, D., McCray, R., & Mac Low, M.-M. 1992, ApJ, 388, 127

Willis, A. G. 1973, A&A, 26, 237

Chapter 4

AKARI/Herschel Far-Infrared Survey of Galactic Supernova Remnants

4.1 Introduction

Supernova (SN) explosions are one of the most energetic events in a galaxy, which inject enormous energy ($\sim 10^{51}$ erg) to the interstellar medium (ISM) and supply heavy elements and possibly dust grains. Since 70 – 80 % of 294 known Galactic supernova remnants (SNRs) are probably core-collapse SNRs, we expect that a good fraction of SNRs could interact with their parental molecular clouds (MCs). These MC-interacting SNRs are bright in the far-infrared (far-IR) waveband such as 3C391, W44, and IC443, so far-IR data provides a new window to study the environment of SNRs and their physical characteristics.

Since the Infrared Astronomical Satellite (*IRAS*) survey of Galactic SNRs in 10 to 100 μm bands, we have an opportunity to investigate the physical and morphological characteristics of SNRs in far-infrared (far-IR) bands in detail. From the IRAS survey for about 160 Galactic SNRs, Arendt (1989) and Saken et al. (1992)

detected that about 20 % of targets showed well-defined and spatially correlated features in far-IR wavebands. Their studies also revealed that dust grains in older SNRs are colder and more massive, so they suggested that the correlation between the age of SNRs and the effect of dusty environment on SNRs. However, *IRAS* survey had limitations for detailed study of SNRs because of a low resolution and a narrow band coverage.

After many years since the *IRAS* survey, the *Spitzer* GLIMPSE survey data in IRAC (3.6, 4.5, 5.8, and 8.0 μm) and MIPS (24 and 70 μm) bands has been used to explore inner Galaxy ($10^\circ < l < 65^\circ$ and $285^\circ < l < 350^\circ$, $|b| < 1^\circ$) with advanced high resolution and sensitivity. Using IRAC images, Lee (2005) and Reach et al. (2006) detected near-IR emission originated from shock-heated dust, find-structure line, and molecular lines towards about 18 interacting SNRs with MCs. Pinheiro Gonçalves et al. (2011) searched for mid-IR counterpart from the SNRs and identified correlated morphologies from 39 out of 121 SNRs. These sources showed a linear correlation between mid-IR and radio fluxes. However, due to the limitation of the observed area, the detected SNRs in IR bands are not increased than before, so systematic studies for all known SNRs are additionally needed with higher resolution and much wider $l - b$ coverage in IR bands.

Recently, far-IR surveys become available, including the all-sky survey by the *AKARI* (Doi et al. 2012) and the Galactic plane survey by the *Herschel* (Molinari et al. 2010). The far-IR photometric data of the *AKARI* and *Herschel* data are quite useful in statistical and systematic studies for Galactic SNRs. The *AKARI* survey provides all-sky data covering more than 90 % of the sky, and it is possible to reveal far-IR structures and characteristics for large SNRs. The *Herschel* data from Hi-GAL Galactic plane survey with higher resolution and better sensitivity is useful to describe for small SNRs than previous IR surveys. So, these two data enable us to reveal the detailed structures that we have not seen before.

Using these data, the purpose of this study is to make a catalog of far-IR SNRs in the Milky Way, to explore the environment of SNRs and their physical character-

istics, and to understand the far-IR properties of SNRs interacting with MCs.

This paper has been divided into four sections. In Sect. 4.2, we briefly describes the *AKARI* and *Herschel* far-IR data. In Sect. 4.3, we show the methodology that is used to conduct SNR identifications and flux measurements, and report the results of our survey. Section 4.4 discusses far-IR properties of Galactic SNRs from the survey results. Section 4.5 summarizes the important results of this survey.

4.2 AKARI and Herschel Data

The *AKARI* FIS has performed the all-sky survey in four photometric bands with high spacial resolution than the *IRAS* survey. The four bands had center wavelengths at 65μm (N60), 90μm (WIDE-S), 140 μm (WIDE-L), and 160 μm (N160), which covered the spectral range from 50 to 180 μm. The spatial resolutions are about $0'.7$ for the N60 and WIDE-S bands, and about $1'$ for the WIDE-L and N160 bands (Kawada et al. 2007). The average scan area in four bands covered about 97% of the sky (Doi et al. 2012).

The *Herschel* Photodetector Array Camera and Spectrometer (PACS; 70 and 160 μm) and Spectral and Photometric Imaging REceiver (SPIRE; 250 and 350 μm) data are also obtained for this survey. The archival *Herschel* PACS/SPIRE data generated by the *Herschel* data processing pipeline are downloaded from Herschel Science Archive (HSA)[1]. The spatial resolution of *Herschel* are $5.2''$ to $25''$.

These data provide the much improved spatial resolution and the sensitivity with reduced source confusion in far-IR studies of Galactic SNRs. We summarized the instrumental characteristics of the *AKARI* and *Herschel* in Table 4.1.

[1] http://www.cosmos.esa.int/web/herschel/science-archive

Table 4.1. Instrument characteristics of *AKARI* and *Herschel*

	AKARI				*Herschel*			
Central Wavelength (μm)	60	90	140	160	70	160	250	350
Wavelength Range (μm)	50−80	60−110	110−180	140−180	60−85	130−210	$\lambda/\Delta\lambda \sim 3$	$\lambda/\Delta\lambda \sim 3$
FWHM (arcsec)	37 ± 1^1	39 ± 1^1	58 ± 3^1	61 ± 4^1	5.2	12	18.2	24.9
Pixel size (arcsec^2)	15×15	15×15	15×15	15×15	3.2×3.2	6.4×6.4	6×6	10×10

Note. — [1] Kawada et al. (2007), AKARI data - ver 2.0, Herschel data - PACS (level 2.5 product), SPIRE (level 2.0 & 2.5 products)

4.3 Results

4.3.1 SNR Identifications

The *AKARI* FIS (65, 90, 140, and 160 μm) and *Herschel* PACS/SPIRE (70, 160, 250 and 350 μm) data were used to search for associated far-IR features with SNRs comparing with radio continuum and X-ray data by a visual inspection method. For our survey, we examined 294 known SNRs in our Galaxy (Green 2014) and classified the targets from 1 to 5 groups. The criterion of identification was almost same as the Arendt's strategy (Arendt 1989). The first group is a detected SNR which shows well-defined far-IR structures such as shells or filaments coinciding spatially with radio or X-ray morphology. The second group is a possible SNR associating with a far-IR source, but the far-IR emission shows a little confused to define its distribution and is not strong to show a clear correlation with a known SNR at other wavelengths. The third group is a conclusive case showing extended and diffused far-IR emissions in the line of sight toward the SNR without any correlated and associated features. The forth group is not detected in any of far-IR emissions from the SNR. We also marked a partially broken data or no observed region toward targets in fifth group.

Based on these criteria, 59 SNRs (20 %) were classified as group 1 including 13 interacting SNRs with MCs. These targets were dominantly detected at 70 and 90 μm bands. Figs. 4.2-4.5 display the images of the far-IR detected SNRs with radio continuum and X-ray data. The number of SNRs categorized as group 2, 3, and 4 were 90 (30.6 %), 138 (46.9 %), and 7 (2.4 %), respectively. Table 4.2 shows the list of the detected SNRs from our survey and summarizes results from previous surveys at mid/far-IR and γ-ray bands. Table 4.2 also contains the observed evidence from interacting SNRs with MCs (Jiang et al. 2010).

Table 4.2. FIR Detected SNRs in AKARI and Herschel Survey

SNR name	other name	Size[a]	IA[b]	IS[b]	IRAC[b]	MIPS[b]	AKARI[b]	*Herschel*[b]	MCs[c]	γ-ray[d]
0.0−0.0	Sgr A East	$3.5' \times 2.5'$	—	3	—	—	1	1	OH, LB, MA, H_2	FGL, HES, VER
0.9+0.1		$8'$	4	4	—	—	5	3/5	—	HES
1.4−0.1		$10'$	—	—	—	—	4/5	3	OH	—
4.5+6.8	Kepler	$3'$	1	1	—	—	2/5	1	—	—
5.4−1.2	Milne 56	$35'$	4	4	—	—	3	—	OH	FGL
6.4−0.1	W28	$48'$	3	2	—	—	1	1	OH, LB, MA, H_2 MA	HESS, FGL, EGR, AGL
6.5−0.4		$27'$	—	—	—	—	2	2	—	EGR
8.3−0.0		$5' \times 4'$	—	—	—	—	1	1	—	—
8.7−0.1	W30	$45'$	—	4	—	—	1	1	OH	FGL, HES
9.7−0.0		$12' \times 11'$	—	—	—	—	3	3	OH	—
10.5−0.0		$6'$	—	—	—	1	1	1	—	—
11.0−0.0		$11' \times 9'$	—	—	—	3	2	1	—	—
11.1−1.0		$18' \times 12'$	—	—	—	—	1	1	—	—
11.1+0.1		$12' \times 10'$	—	—	—	1	1	1	—	—
11.2−0.3		$4'$	1	2	1	1	1	1	—	HES
11.4−0.1		$8'$	4	4	3	3	3	3	—	FGL
12.0−0.1		$7'$	1	1	3	3	2	2	—	—
12.8−0.0		$3'$	—	—	—	3	3	3	—	HES, MAG
13.5+0.2		$5' \times 4'$	—	—	3	3	2	1	—	—
14.3+0.1		$5' \times 4'$	—	—	—	1	1	1	—	—
15.4+0.1		$15' \times 14'$	—	—	—	3	3	3	—	HES
15.9+0.2		$7' \times 5'$	4	4	3	1	2	1	—	—
16.4−0.5		$13'$	—	—	—	1	2	2	—	—
16.7+0.1		$4'$	—	4	3	2	3	2	OH, MA	—
17.4−0.1		$6'$	—	—	—	2	1	1	—	—

Table 4.2 (cont'd)

SNR name	other name	Size[a]	IA[b]	IS[b]	IRAC[b]	MIPS[b]	AKARI[b]	*Herschel*[b]	MCs[c]	γ-ray[d]
18.6−0.2		6′	—	—	—	1	1	1	—	—
18.8+0.3	Kes 67	17′× 11′	2	4	3	3	2	2	MA, LB, ratio	EGR
20.0−0.2		10′	4	4	3	3	3/5	3	—	FGL
20.4+0.1		8′	—	—	—	1	1	1	—	—
21.5−0.9		4′	4	4	3	1	2	1	—	—
21.5−0.1		5′	—	—	—	1	1/5	1	—	—
21.8−0.6	Kes 69	20′	3	4	1	1	1	1	OH, LB, MA, H_2	—
22.7−0.2		26′	3	4	1	2	2	2	—	—
23.3−0.3	W41	27′	3	4	2	2	1	1	RC	FGL, HES, MAG
23.6+0.3		10′	1	2	3	1	1	1	—	—
24.7+0.6		30′× 15′	4	4	3	2	3	3	—	FGL
27.4+0.0	4C-04.71	4′	3	1	3	1	2	1	—	FGL
27.8+0.6		50′× 30′	4	4	3	3	3	3	—	FGL, EGR
28.6−0.1		13′× 9′	—	—	3	1	3	1	—	
28.8+1.5		100′	—	—	—	—	3	—	—	FGL, EGR
29.7−0.3	Kes 75	3′	4	4	3	1	3	2	LB, MA	HES
31.9+0.0	3C391	7′× 5′	1	1	1	1	1	1	OH, LB, MA, H_2	FGL
32.4+0.1		6′	—	—	—	2	2	2	—	FGL
32.8−0.1	Kes 78	17′	3	1	3	3	2	2	OH	HES
33.2−0.6		18′	2	1	3	2	2	1	—	—
33.6+0.1	Kes 79	10′	2	2	2	1	2	1	MA	FGL
34.7−0.4	W44	35′× 27′	1	4	1	1	1	1	OH, LB, MA, ratio, H_2 MA	FGL, EGR
35.6−0.4		15′× 11′	—	—	—	1	3	3	—	HES
36.6−0.7		25′	—	1	2	3	3	3	—	—
39.2−0.3	3C396	8′× 6′	4	4	1	1	2	1	LB, MA, H_2 MA	—

Table 4.2 (cont'd)

SNR name	other name	Size[a]	IA[b]	IS[b]	IRAC[b]	MIPS[b]	AKARI[b]	*Herschel*[b]	MCs[c]	γ-ray[d]
40.5−0.5		22′	2	4	4	2	2	2	MA	HES, EGR, MLR
41.1−0.3	3C397	4.5′× 2.5′	3	4	1	1	3/5	2	LB, MA	—
43.3−0.2	W49B	4′× 3′	1	1	1	1	1	1	H_2 MA	FGL, HES
45.7−0.4		22′	—	4	2	2	3	2	—	FGL
46.8−0.3	HC30	17′× 13′	3	1	3	3	2	1	—	—
49.2−0.7	W51	30′	4	1	3	3	2	2	OH, LB, MA	MLR
54.1+0.3		1.5′	1	1	3	3	1	1	MA	VER
54.4−0.3	HC40	40′	3	4	1	1	2	2	LB, MA	FGL
59.8+1.2		20′× 16′	—	—	—	—	1	1	—	—
63.7+1.1		8′	—	—	—	—	1	1	RC	—
65.1+0.6		90′× 50′	—	4	—	—	2	2	—	MLG
65.3+5.7		310′× 240′	1	4	—	—	1	—	—	—
69.0+2.7		80′	1	1	—	—	2	—	—	FGL, EGR
69.7+1.0		16′× 14′	—	—	—	—	1	1	—	—
74.0−8.5	Cygnus Loop	230′× 160′	1	1	—	—	1	—	MA	FGL
74.9+1.2	CTB 87	8′× 6′	4	4	—	—	3	—	RC	FGL, VER
76.9+1.0		9′	—	—	—	—	3	3	—	FGL
78.2+2.1	γ Cygni	60′	3	1	—	—	2	—	MA	FGL, EGR, AGL, MLR, VER
85.9−0.6		24′	—	—	—	—	1	—	RC	—
89.0+4.7	HB21	120′× 90′	2	2	—	—	1	—	LB, MA, ratio, H_2	FGL
94.0+1.0	3C 434.1	30′× 25′	4	4	—	—	2	2	MA, ratio	—
106.3+2.7		60′× 24′	—	—	—	—	2	—	RC	FGL, EGR, MLR
109.1−1.0	CTB 109	28′	1	1	—	—	2	—	LB, MA	FGL
111.7−2.1	Cas A	5′	1	1	—	—	1	1	RC	FGL, MAG, VER
114.3+0.3		90′× 55′	3	4	—	—	2	2/5	—	FGL

Table 4.2 (cont'd)

SNR name	other name	Size[a]	IA[b]	IS[b]	IRAC[b]	MIPS[b]	AKARI[b]	*Herschel*[b]	MCs[c]	γ-ray[d]
116.5+1.1		$80' \times 60'$	3	4	—	—	3	—	—	FGL
116.9+0.2	CTB 1	$34'$	3	1	—	—	2	2	—	—
119.5+10.2	CTA 1	$90'$	4	4	—	—	2	—	—	FGL, EGR, AGL, VER
120.1+1.4	Tycho	$8'$	1	1	—	—	1	1	MA	FGL, VER
127.1+0.5	R5	$45'$	2	4	—	—	2	2	—	FGL
130.7+3.1	3C58	$9' \times 5'$	3	4	—	—	3	—	—	FGL, MAG
132.7+1.3	HB3	$80'$	4	4	—	—	3	3/5	MA	FGL, EGR
156.2+5.7		$110'$	—	—	—	—	2	—	—	FGL
160.9+2.6	HB9	$140' \times 120'$	3	1	—	—	2	—	—	FGL
166.0+4.3	VRO 42.05.01	$55' \times 35'$	2	4	—	—	2	—	RC	FGL
179.0+2.6		$70'$	4	4	—	—	3	—	—	FGL
180.0−1.7	S147	$180'$	2	4	—	—	2	—	—	FGL, EGR
184.6−5.8	Crab Nebula	$7' \times 5'$	1	1	—	—	1	1	—	HES, MAG, MLR, VER
189.1+3.0	IC443	$45'$	1	1	—	—	1	—	OH, LB, MA, ratio, H_2	FGL, EGR, AGL, MAG ,MLR, VER
192.8−1.1	PKS 0607+17	$78'$	1	1	—	—	2	2/5	RC	—
205.5+0.5	Monoceros Nebula	$220'$	3	1	—	—	1	—	RC	FGL, HES, EGR
260.4−3.4	Puppis A	$60' \times 50'$	1	1	—	—	1	—	RC	FGL
263.9−3.3	Vela (XYZ)	$255'$	1	1	—	—	2	—	MA	FGL, HES
266.2−1.2	RX J0852.0-4622	$120'$	—	—	—	—	3	—	—	FGL, HES
284.3−1.8	MSH 10−53	$24'$?	—	—	—	—	2	—	MA	FGL
290.1−0.8	MSH 11−61A	$19' \times 14'$	3	4	—	—	2	1	RC	FGL
291.0−0.1	MSH 11−62	$15' \times 13'$	3	3	—	—	2	2	—	FGL, EGR
292.0+1.8	MSH 11−54	$12' \times 8'$	1	1	—	—	1	—	—	FGL
292.2−0.5		$20' \times 15'$	—	—	—	—	2	2	—	FGL, HES
293.8+0.6		$20'$	4	4	—	—	3	—	—	FGL

Table 4.2 (cont'd)

SNR name	other name	Size[a]	IA[b]	IS[b]	IRAC[b]	MIPS[b]	AKARI[b]	*Herschel*[b]	MCs[c]	γ-ray[d]
296.5+10.0	PKS 1209-51/52	$90' \times 65'$	4	4	—	—	2	—	—	FGL
296.8−0.3	1156−62	$20' \times 14'$	4	4	3	1	3	3	—	—
298.6−0.0		$12' \times 9'$	3	4	2	2	2	2	—	FGL
304.6+0.1	Kes 17	$8'$	1	1	1	1	1	1	H_2	FGL
308.8−0.1		$30' \times 20'$	4	4	2	2	3	2	—	FGL
309.8+0.0		$25' \times 19'$	4	4	3	3	3	2	—	FGL
310.8−0.4	Kes 20A	$12'$	—	—	1	1	1	1	—	—
311.5−0.3		$5'$	4	4	1	1	2	1	—	—
312.4−0.4		$38'$	2	4	3	3	3	2	—	FGL, EGR
315.1+2.7		$190' \times 150'$	—	—	—	—	3	—	—	FGL
315.4−2.3	RCW 86	$42'$	1	1	—	—	2	—	—	FGL, HES
316.3−0.0	MSH 14−57	$29' \times 14'$	3	4	3	3	2	2	—	FGL
317.3−0.2		$11'$	—	—	3	2	1	1	—	—
318.2+0.1		$40' \times 35'$	—	—	3	2	3	3	—	HES
320.4−1.2	MSH 15−52	$35'$	2	3	—	—	3	3	—	FGL, HES
321.9−0.3		$31' \times 23'$	4	3	3	3	3	3	—	FGL
323.5+0.1		$13'$	2	1	2	2	2	2	—	—
326.3−1.8	MSH 15−56	$38'$	2	4	—	—	3	—	—	FGL
327.1−1.1		$18'$	4	4	—	—	3	—	—	HES
327.6+14.6	SN1006	$30'$	3	4	—	—	3	—	—	FGL, HES
332.4−0.4	RCW 103	$10'$	4	4	1	1	2	2	MA, H_2 MA	FGL
332.4+0.1	MSH 16−51	$15'$	2	3	2	2	2	2	—	FGL
335.2+0.1		$21'$	4	4	2	2	4	4	—	FGL, HES
336.7+0.5		$14' \times 10'$	4	4	4	1	2	2	—	FGL
337.0−0.1	CTB 33	$1.5'$	4	4	3	3	2	2	OH	—

Table 4.2 (cont'd)

SNR name	other name	Size[a]	IA[b]	IS[b]	IRAC[b]	MIPS[b]	AKARI[b]	*Herschel*[b]	MCs[c]	γ-ray[d]
337.2−0.7		6′	4	4	4	1	3	3	—	—
337.2+0.1		3′× 2′	—	—	—	3	3	3	—	FGL, HES
337.8−0.1	Kes 41	9′× 6′	4	4	2	2	2	2	OH	FGL
338.3−0.0		8′	4	4	3	3	3	3	—	FGL, HES
338.5+0.1		9′	3	4	3	3	3	3	—	HES
340.6+0.3		6′	1	1	2	1	1	1	—	—
343.0−6.0	RCW 114	250′	4	—	—	—	3	—	—	FGL, EGR
343.1−2.3		32′	—	—	—	—	3	—	—	FGL, EGR, HES
343.1−0.7		27′× 21′	—	—	3	3	1	1	—	—
344.7−0.1		10′	3	4	1	1	2	1	—	HES
345.7−0.2		6′	—	—	4	1	3	3	—	HES
346.6−0.2		8′	4	4	1	2	3	2	OH, H_2	—
347.3−0.5		65′× 55′	—	—	3	3	2	2	LB, MA	FGL, HES
348.5−0.0		10′	—	—	1	1	5	1	OH, H_2	—
348.5+0.1	CTB 37A	15′	2	4	1	1	2/5	1	OH, MA	FGL, HES
348.7+0.3	CTB 37B	17′	1	3	3	1	2	2	—	HES
349.7+0.2		2.5′× 2′	1	1	1	1	1	1	OH, LB, MA, ratio, H_2	FGL, HES
350.1−0.3		4′	4	4	—	—	2	1	—	FGL
351.2+0.1		7′	4	4	—	—	2	1	—	—
353.6−0.7		30′	—	—	—	—	1/5	1	—	HES
354.1+0.1		15′× 3′	—	—	—	—	1/5	1	—	FGL
355.4+0.7		25′	—	—	—	—	3	3	—	FGL
355.6−0.0		8′× 6 ′	—	—	—	—	3	3	—	EGR
356.3−0.3		11′× 7′	—	—	—	—	4	4	—	FGL
357.7−0.1	MSH 17-39	8′× 3′	4	3	—	—	2	1	OH, MA	FGL

Table 4.2 (cont'd)

SNR name	other name	Size[a]	IA[b]	IS[b]	IRAC[b]	MIPS[b]	AKARI[b]	*Herschel*[b]	MCs[c]	γ-ray[d]
357.7+0.3		$24'$	4	4	—	—	3	3	OH	—
358.0+3.8		$38'$	—	—	—	—	3	—	—	FGL
358.5−0.9		$17'$	—	—	—	—	3	3	—	FGL
359.1−0.5		$24'$	4	4	—	—	3	3	OH, MA	HES
359.1+0.9		$12' \times 11'$	—	—	—	—	3	3	—	FGL

[a] Radio sizes of Galactic SNRs (Green 2014).

[b] Summary of Infrared survey catalog- IA: Arendt (1989), IS: Saken et al. (1992), IRAC: Reach et al. (2006), MIPS: Goncalves et al. (2011), **AKARI/Herschel: This work**, Detection classification - **1**: detected, **2**: possible detected, **3**: not conclusive, **4**: no emission, **5**: partially broken or no data

[c] Evidence of interacting SNRs with MCs (CO, HCO^+, CS, etc.) (Jiang et al. 2010; Jeong et al. 2012, 2013) - OH (OH maser), LB (line broadening), MA (morphological agreement of MCs with SNRs), RC (rough spatial correlation between SNRs and MCs), ratio (line ratio, e.g., CO $J = 2 - 1/1 - 0$), H_2 (H_2 line emission)

[d] Summary of γ-ray catalogs: **FGL** - *Fermi*-Large Area Telescope source catalog (Abdo et al. 2009a, 2010; Nolan et al. 2012; Ackermann et al. 2013; Araya 2013; Giordano et al. 2012; Wu et al. 2011; Yuan et al. 2014), **HES** - High Energy Stereoscopic System source catalog (HESS) (http://www.mpi-hd.mpg.de/hfm/HESS/pages/home/sources/, http://www.mpi-hd.mpg.de/hfm/HESS/pages/home/som/, and references therein), **EGR** - Energetic Gamma Ray Experiment Telescope (EGRET) (Hartman et al. 1999; Torres et al. 2003; Casandjian & Grenier 2008), **AGL** - Astrorivelatore Gamma ad Immagini LEggero (AGILE) (Pittori et al. 2009; Chen et al. 2011; Verrecchia et al. 2013), **MAG** - Major Atmospheric Gamma Imaging Cerenkov telescope (MAGIC) (Albert et al. 2006a,b, 2007a,b; Aleksić et al. 2012, 2014), **MLR** - Milagro gamma-ray observatory (Abdo et al. 2009b, 2012), **VER** - Very Energetic Radiation Imaging Telescope Array System (VERITAS) (Acciari et al. 2009, 2010a,b, 2011; Aliu 2011; VERITAS Collaboration et al. 2011; Aliu et al. 2013a,b; Archer et al. 2014, http://veritas.sao.arizona.edu/veritas-science/veritas-results-mainmenu-72), Catalog of high-energy observations of Galactic SNRs (Ferrand & Safi-Harb 2012, http://www.physics.umanitoba.ca/snr/SNRcat/)

4.3.2 Distributions of Detected SNRs

According to our detection criterion, 59 SNRs are identified as well-established morphology at far-IR bands. These results are comparable to the previous IR studies of Galactic SNR surveys. From the *IRAS* all-sky survey (10 – 100 μm), Arendt (1989) and Saken et al. (1992) found that 30 and 35 SNRs were matched with IR emissions. Therefore, the number of detection increased significantly by a factor of two compared to those of previous studies due to improved spatial resolution and detection sensitivity.

Figure 4.1 shows the spatial distributions of the known and detected SNRs with 30° longitude and 1° latitude bins and displays *AKARI* and *Herschel* detected SNRs in each bins, respectively. We also denote the detection rates on the top of the histograms. In here, we can see that most of the known SNRs are concentrated in the Galactic longitude from -60° to 60° and latitude from -0.5° to 0.5°. However, the detection rates are less than 30 % since we can hardly define associated far-IR emissions with SNRs in the Galactic central regions because of IR contamination along the line of sight. We also expected that the detection rate in the outer Galactic regions could be much higher than the inner regions, because the outer SNRs suffered less IR confusion and extinction than the inner SNRs, but the results of the detection rates were not reflected in the effect of IR confusion along the sight line toward the remnants.

4.3.3 Flux measurement

Among the detected SNRs, we selected 24 targets which show fairly well-defined shell structures clearly seen in the *AKARI* and *Herschel* images. Figs. 4.2 – 4.5 show far-IR distributions of the SNRs. The *Spitzer* 24 μm, X-ray and radio images are also displayed for comparisons. To estimate their far-IR fluxes, the *AKARI* (65, 90, and 140 μm) and *Herschel* (70, 160, 250, and 350 μm) are convolved to the spatial resolution of the *AKARI* 160 μm data ($61''$) and regridded with a same pixel

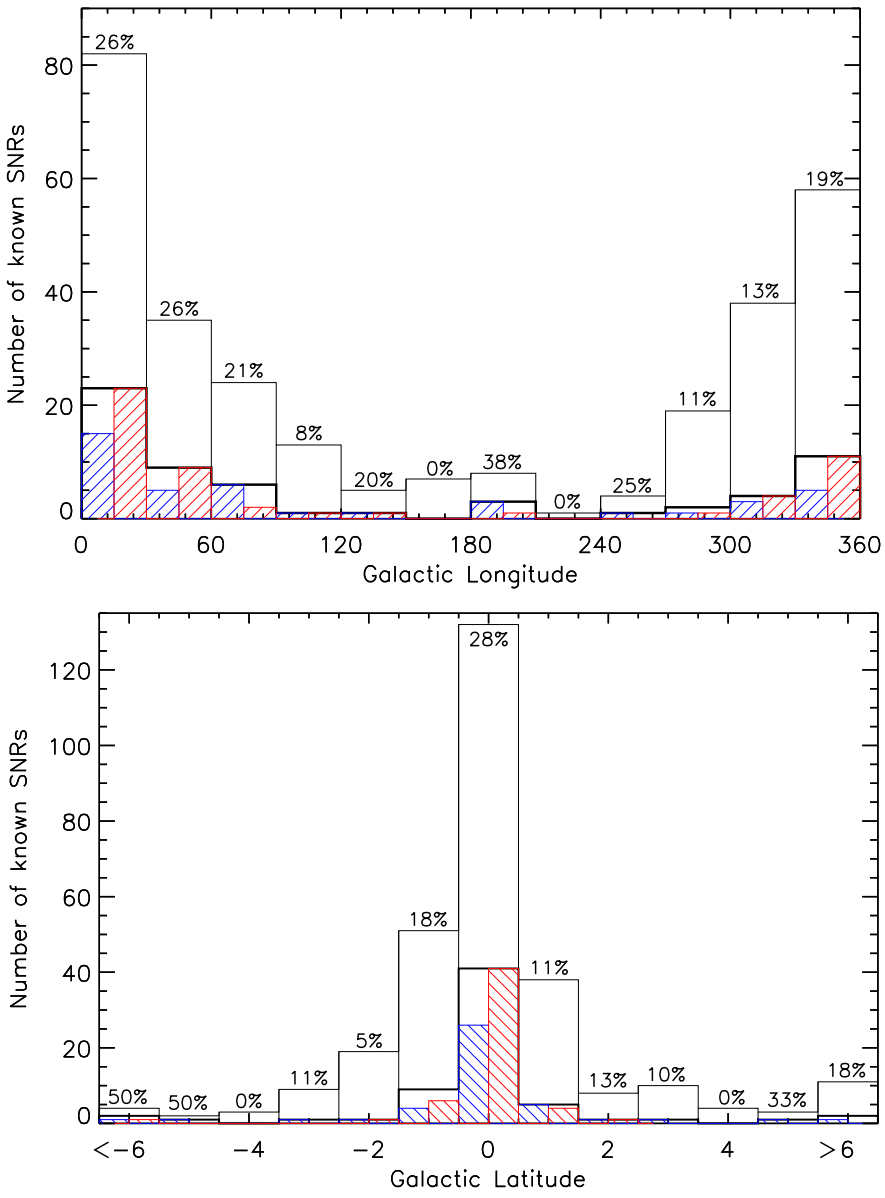

Figure 4.1 Distributions of known and detected SNRs are shown by thin and thick histogram, respectively. Histogram filled by blue and red slash show number of *AKARI* and *Herschel* detected SNRs. Detection rates at longitude and latitude bins are marked on the top of the histogram.

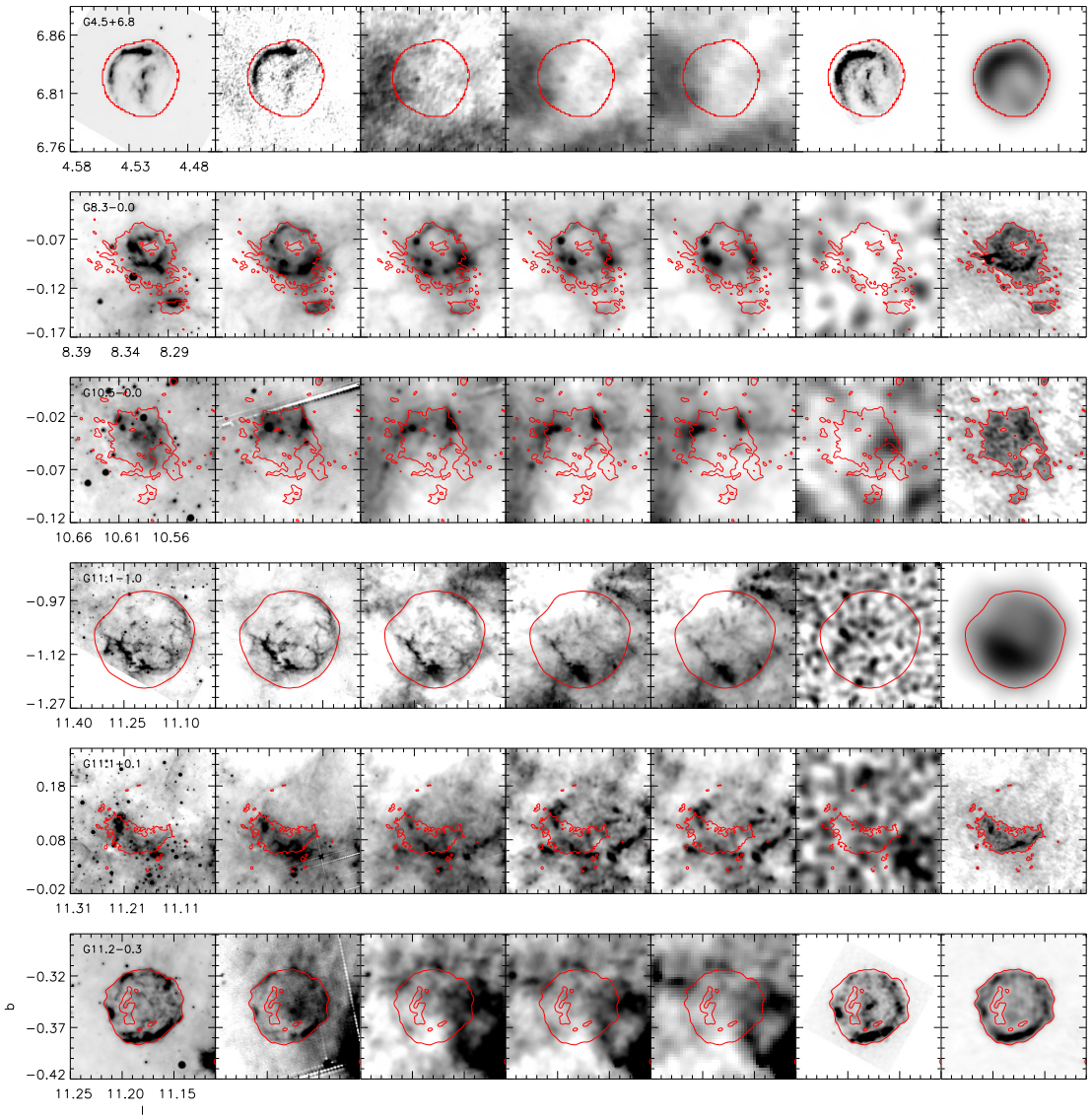

Figure 4.2 Images of *Spitzer* 24 μm, *Herschel* 70, 160, 250, 350 μm, X-ray, and radio continuum data of the selected SNRs. Contours represent radio continuum emission. SNR are from top to bottom: G4.5+6.8 (Kepler), G8.3−0.0, G10.6−0.0, G11.1−1.0, G11.1+0.1, and G11.2−0.3.

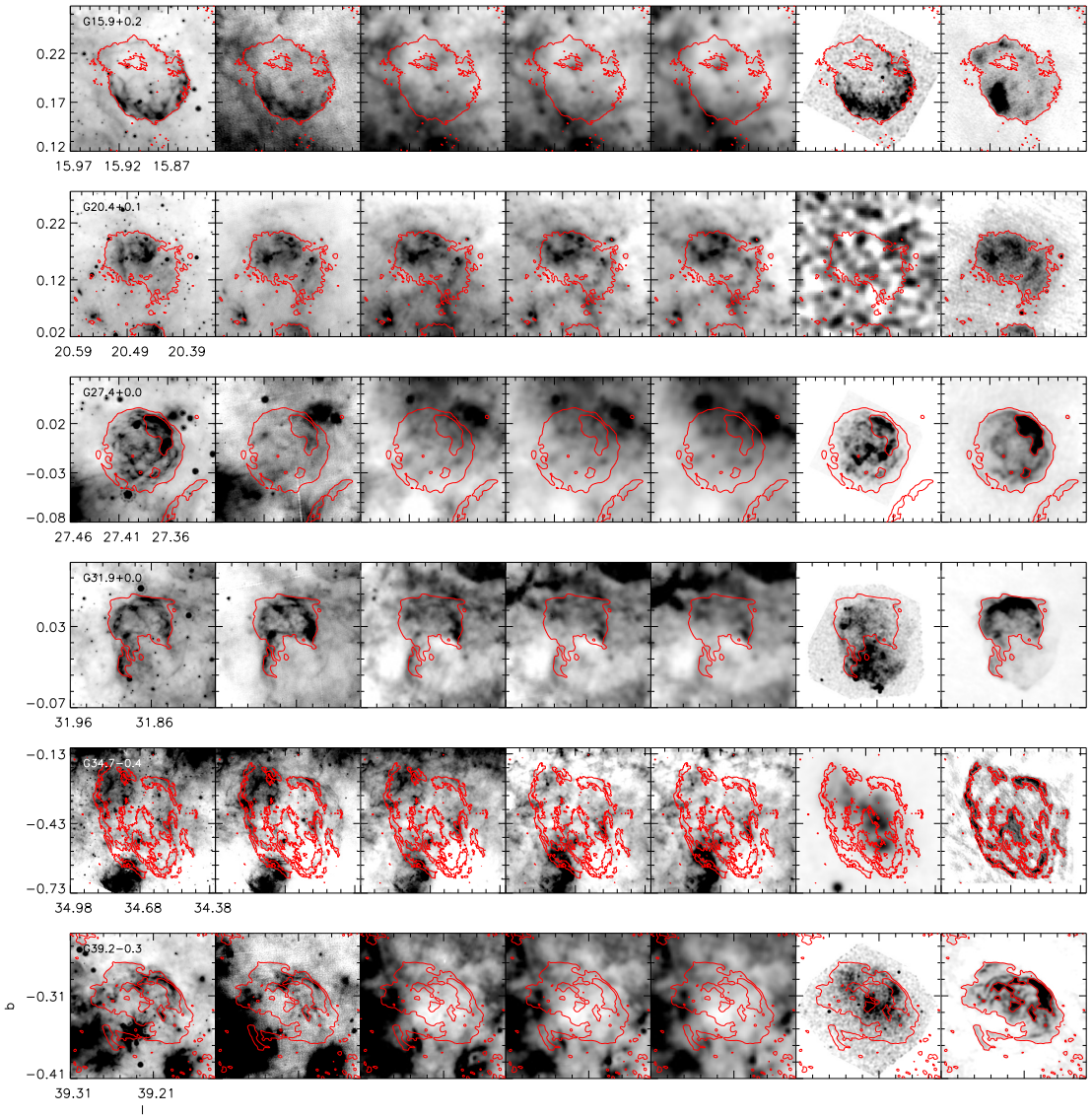

Figure 4.3 The same order of images as Fig. 4.2. SNR are from top to bottom: G15.9+0.2 , G20.4+0.1, G27.4+0.0, G31.9+0.0 (3C391), G34.7−0.4 (W44), and G39.2-0.3 (3C396).

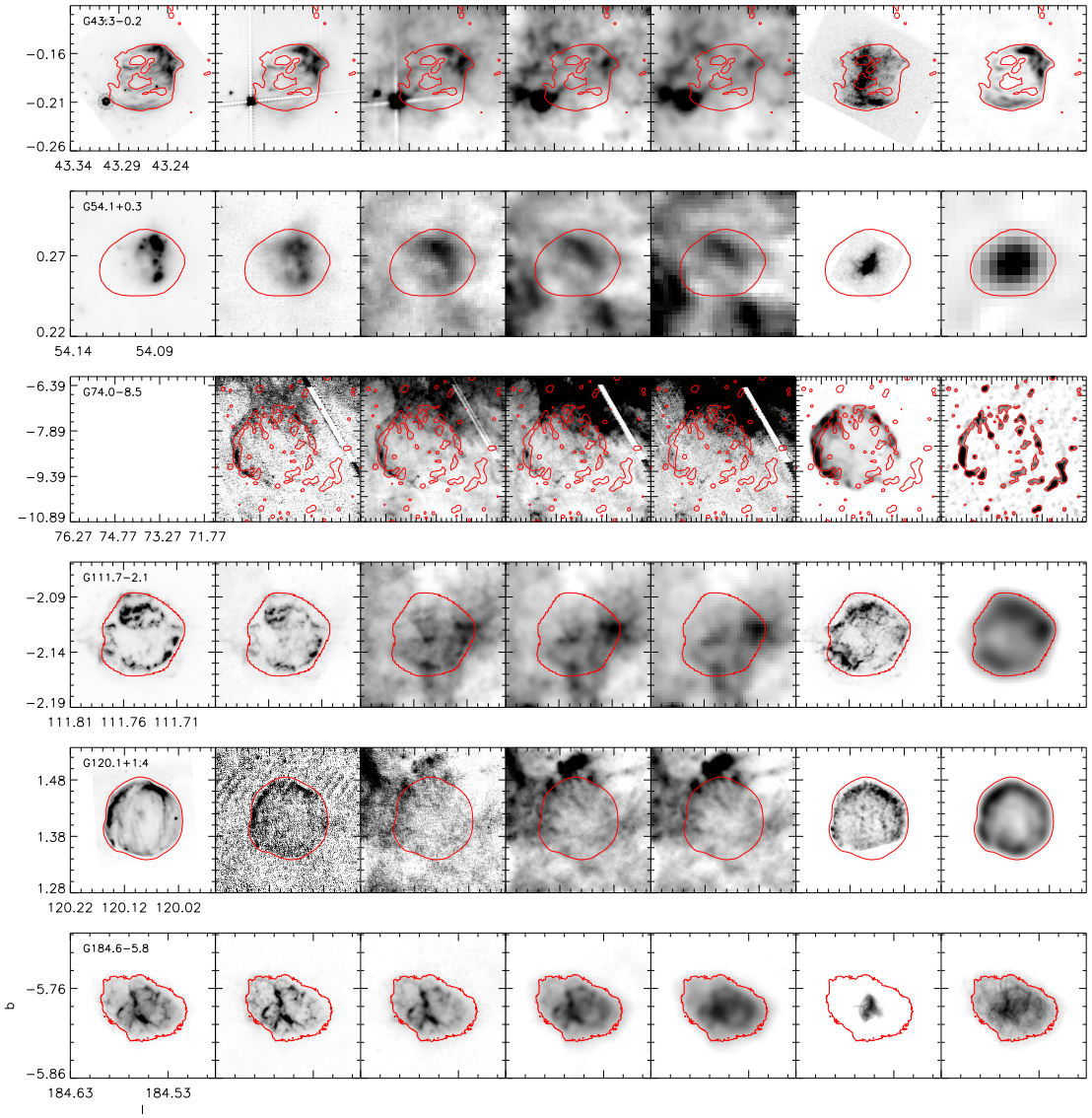

Figure 4.4 The same order of images as Fig. 4.2. SNR are from top to bottom: G43.3−0.2 (W49B), G54.1+0.3, G74.0−8.5 (Cygnus Loop), G111.7-2.1 (Cassiopeia A), G120.1+1.4 (Tycho), and G184.6−5.8 (Crab Nebula). The AKARI (65, 90, 140, and 160 μm) data is used for SNR G74.0−8.5.

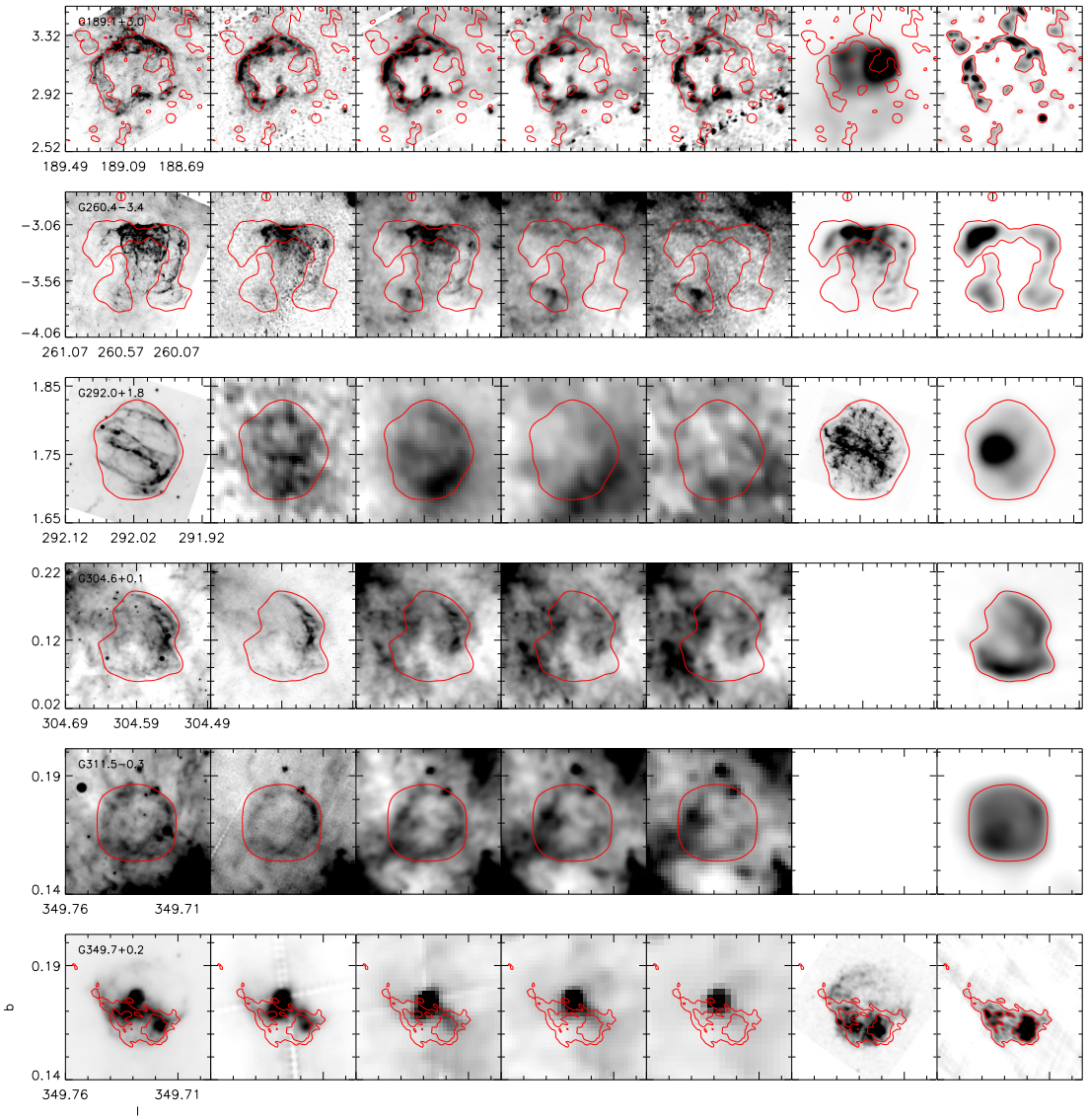

Figure 4.5 The same order of images as Fig. 4.2. SNR are from top to bottom: G189.1+3.0 (IC443), G260.4−3.4 (Puppis A), G292.0+1.8, G304.6+0.1 (Kes 17), G311.5−0.3, and G349.7+0.2. SNR G189.1+3.0, G260.4−3.4, and G292.0+1.8 used the AKARI (65, 90, 140, and 160 μm) data.

Table 4.3. Far-IR Fluxes of 24 Selected Galactic SNRs

SNR (′)	Size[a] (′)	Size$^{b}_{phot}$ (′)	F_{S24} (Jy)	F_{A65} (Jy)	F_{S70} (Jy)	F_{H70} (Jy)	F_{A90} (Jy)	F_{A140} (Jy)	F_{A160} (Jy)	F_{H160} (Jy)	F_{H250} (Jy)	F_{H350} (Jy)
4.5+6.8	3	4	9.5±1.0[c]	—	4.9±0.1	5.7±1.0[c]	—	—	—	—	—	—
8.3−0.0	5×4	5	49.5±5.5	360.4±37.3	481.4±97.2	799.0±43.3	508.6±51.8	1012.1±105.9	1152.4±116.8	1432.8±76.3	626.8±45.5	269.2±19.6
10.5−0.0	6	7×5	12.5±1.8	180.8±19.1	289.0±58.9	420.8±23.3	253.9±27.6	181.3±45.7	682.4±88.0	723.0±53.7	320.2±32.2	126.5±14.6
11.1−1.0	18×12	19.8	83.1±8.3	860.1±86.3	—	1644.9±82.8	1132.2±113.8	1931.3±196.7	1809.4±187.1	2419.0±126.8	957.0±75.6	396.3±31.3
11.1+0.1	12×10	9	16.0±2.0[d]	224.9±25.8	297.0±60.0[d]	455.3±30.9	367.5±45.5	735.0±105.3	—	1100.2±92.1	326.7±30.2	158.1±14.9
11.2−0.3	4	5	40.0±5.0[d]	94.7±9.8	101.0±23.0[d]	153.8±9.8	98.2±11.7	—	7.8±11.8	140.8±22.4	77.4±13.9	29.5±6.2
15.9+0.2	7×5	5.6	16.0±2.0[d]	50.7±6.2	55.0±16.0[d]	59.7±5.1	68.4±9.0	26.4±11.2	45.0±9.6	45.6±14.2	24.3±7.6	7.4±3.0
20.4+0.1	8	9.6×8	79.0±9.0[d]	861.8±86.2	1160.0±230.0[d]	1329.8±66.8	1391.7±139.3	3275.4±328.2	3040.4±306.0	2955.5±150.0	1075.9±77.6	440.9±32.0
27.4+0.0	4	5	37.0±4.0[d]	64.0±7.2	87.0±18.0[d]	99.0±7.7	36.8±7.3	184.3±33.4	287.8±35.3	279.1±34.5	176.6±25.1	80.8±12.2
31.9+0.0	7×5	8.8×7	39.0±4.0[d]	293.8±30.0	395.0±81.0[d]	753.6±39.3	334.7±35.2	572.9±65.3	491.5±62.9	532.6±35.3	75.9±17.8	—
34.7−0.4	35×27	37×27	348.0±39.0[d]	4812.2±481.8	6330.0±1300.0[d]	8267.0±414.9	8676.4±868.9	20038.1±2007.6	21769.4±2179.6	18957.0±953.9	1718.8±129.9	530.1±44.3
39.2−0.3	8×6	7×5	8.5±1.0[d]	30.7±3.7	34.0±11.0[d]	57.1±3.6	—	—	—	—	—	—
43.3−0.2	4×3	6.4×5.2	77.0±8.0[d]	392.5±39.6	529.0±107.0[d]	856.8±43.0	404.1±41.2	297.9±37.6	182.9±33.6	386.6±26.6	61.4±10.0	12.6±5.2
54.1+0.3	12	4.4	23.7±2.4	46.9±4.8	66.3±13.3	94.9±4.9	39.9±4.1	18.2±2.5	4.4±2.2	21.0±2.8	—	—
74.0−8.5	230×160	200×150	—	1906.1±190.6	—	—	2414.4±241.5	4873.0±487.4	2573.7±257.5	—	—	—
111.7−2.1	5	6	202.0±20.0[e]	95.2±9.6	100.0±20.0[e]	143.0±7.2	79.1±8.0	61.8±6.7	61.2±6.9	88.0±5.7	50.2±4.3	34.6±2.8
120.1+1.4	8	10	20.4±2.0	28.9±2.9	32.7±6.6	32.1±1.7	23.3±2.4	7.1±1.2	4.5±1.3	10.2±1.9	9.0±1.5	7.9±1.0
184.6−5.8	7×5	7.6×5.6	59.3±5.9[f]	153.9±15.4	208.8±33.3[f]	210.6±10.5	130.3±13.0	124.7±12.5	99.0±9.9	142.2±7.1	92.7±6.5	94.3±6.6
189.1+3.0	45	42	78.3±8.0	1705.0±170.5	1506.8±301.4	—	1551.4±155.2	2700.4±270.4	2623.5±263.5	—	—	—
260.4−3.4	60×50	57×54	230.0±11.0[g]	1578.0±157.9	1025.0±51.0[g]	—	887.7±88.9	122.9±20.9	201.0±27.7	—	—	—
292.0+1.8	12×8	10	11.9±1.2	40.9±4.1	38.1±7.6	—	30.7±3.1	27.5±3.4	8.6±2.4	24.7±2.2	—	—
304.6+0.1	8	9	19.2±1.9	208.4±20.9	334.4±67.0	392.0±19.7	307.0±30.7	937.9±94.1	778.9±78.5	1062.0±54.3	572.4±40.7	264.1±18.8
311.5−0.3	5	4.4	3.5±0.5[d]	44.2±4.7	58.0±14.0[d]	116.8±6.7	37.1±4.6	—	—	60.8±9.7	14.9±4.7	4.6±2.0
349.7+0.2	2.5×2	3.6	48.5±4.9	346.2±35.2	368.7±73.9	653.9±32.9	308.2±31.9	432.2±52.1	351.9±57.6	594.8±32.3	222.2±16.4	82.6±6.1

Note. — The results of flux calibrations from *Spitzer*, *AKARI* (v2.0), and *Herschel* data. [a]The sizes (Size) are known angular diameter of Galactic SNRs (Green 2014). [b]The photometric sizes (Size$_{phot}$) are used for calibrated area of the IR fluxes. References for Spitzer 24 μm fluxes are: [c]Blair et al. (2007), [d] Pinheiro Gonçalves et al. (2011), [e]Hines et al. (2004), [f]Gomez et al. (2012), [g]Arendt et al. (2010)

size of the $AKARI$ data ($15''$). Using the resultant map, we estimated their fluxes in each band. The circular or elliptical apertures were used for the photometry and the same aperture size was adopted for both the $AKARI$ and $Herschel$ data to extract the fluxes at each wavelength. To determine the photometric area, we used radio continuum data to choose a valid aperture covering all of the emission. The photometric sizes were summarized in Table 4.3. An annulus of a circular or an elliptical shaped area with $30''$ width is employed to remove the background emissions. The background area is located at $30''$ away from the outer boundary of the photometric region. We also excluded strong and embedded emissions in HII regions or uncorrelated features from source and background area. The flux errors (σ_{tot}) were estimated via $\sigma_{tot} = \sqrt{\sigma_{cal}^2 + \sigma_{sky}^2}$, where σ_{cal} is the flux calibration uncertainties assumed to be 10 % for FIS, 5 % for PACS, and 7 % for SPIRE, and σ_{sky} is the sky uncertainties based on the standard deviation of the background fluctuations. The results of the estimated fluxes at far-IR bands are shown in Table 4.3.

4.3.4 Far-IR Correlations between Spitzer, AKARI, and Herschel Data

To check out the consistency of the far-IR data, we compared the flux differences between the $AKARI$ (65 and 160 μm), $Herschel$ (70 and 160 μm), and $Spitzer$ 70 μm data using the 24 selected SNRs. Fig. 4.6 showed the result of the correlation between the $AKARI$ 65 μm and $Herschel$ 70 μm. In this comparison, we used 19 SNRs which were derived the fluxes at both wavelengths. The correlation showed good agreement with the selected data, but the result showed a steep slope from linear and power-law fitting methods in logarithmic scale. The $Herschel$ 70 μm fluxes were about 2 times greater than the $AKARI$ 65 μm.

The comparison between the $AKARI$ 65 μm and $Spitzer$ 70 μm fluxes is presented in Fig. 4.7. The correlation was good agreement with the 21 selected data, and the range of the fitting function on the log scale was about 1.1. In the region of the fluxes between 100 and 1000 Jy, the $Spitzer$ 70 μm was slightly stronger than

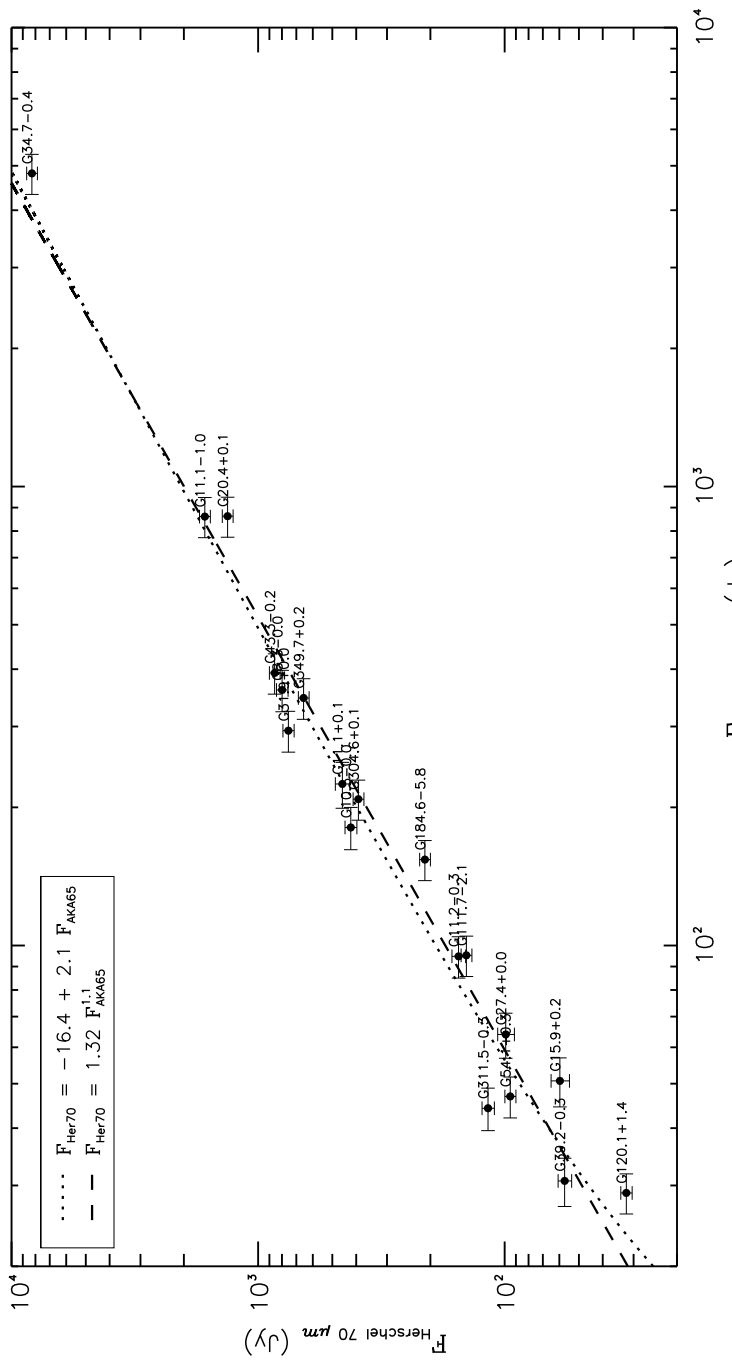

Figure 4.6 Correlation between *AKARI* 65 μm and *Herschel* 70 μm fluxes. The dotted and dashed lines indicate results of a linear fit and a power-law fit in logarithmic scale, respectively. The fitting results are shown in the insert of this figure.

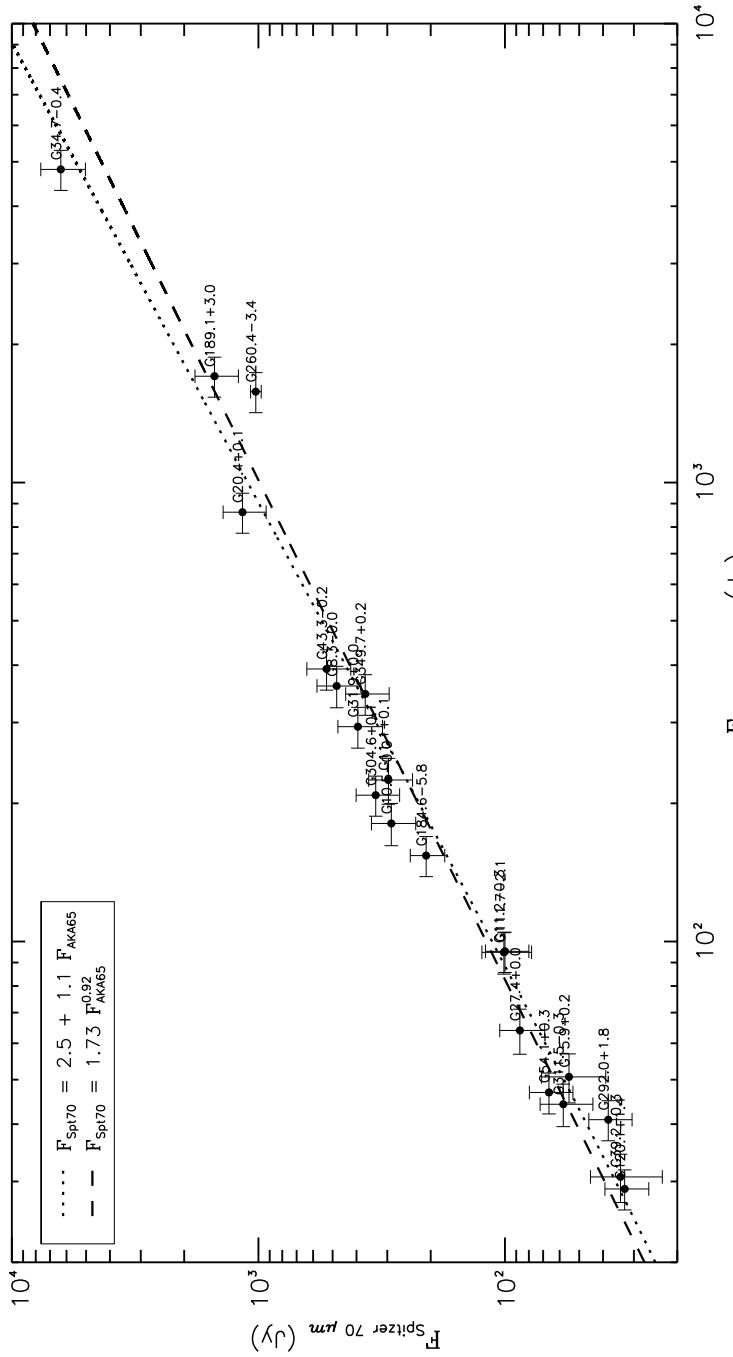

Figure 4.7 Correlation between *AKARI* 65 μm and *Spitzer* 70 μm fluxes. The dotted and dashed lines mark linear and power-law fitting results in logarithmic scale.

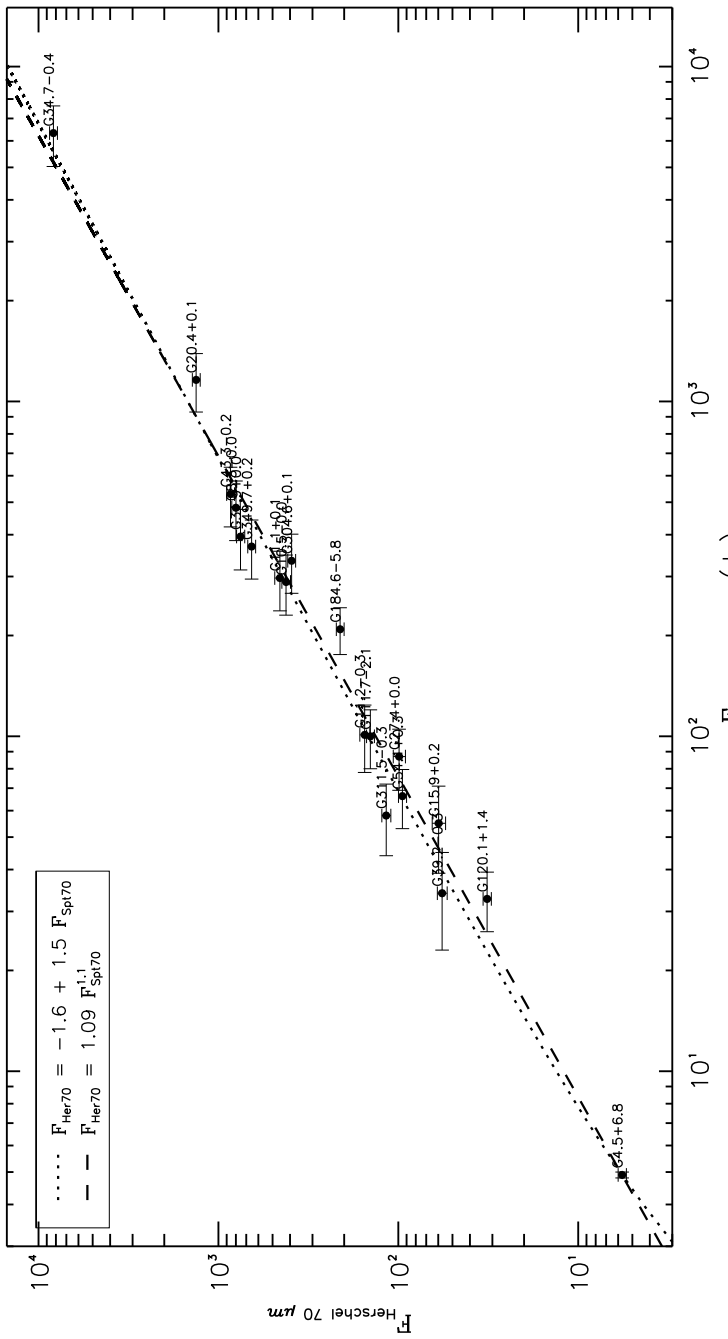

Figure 4.8 Correlation between *Spitzer* 70 μm and *Herschel* 70 μm fluxes. The dotted and dashed lines are based on linear and power-low fitting results in logarithmic scale.

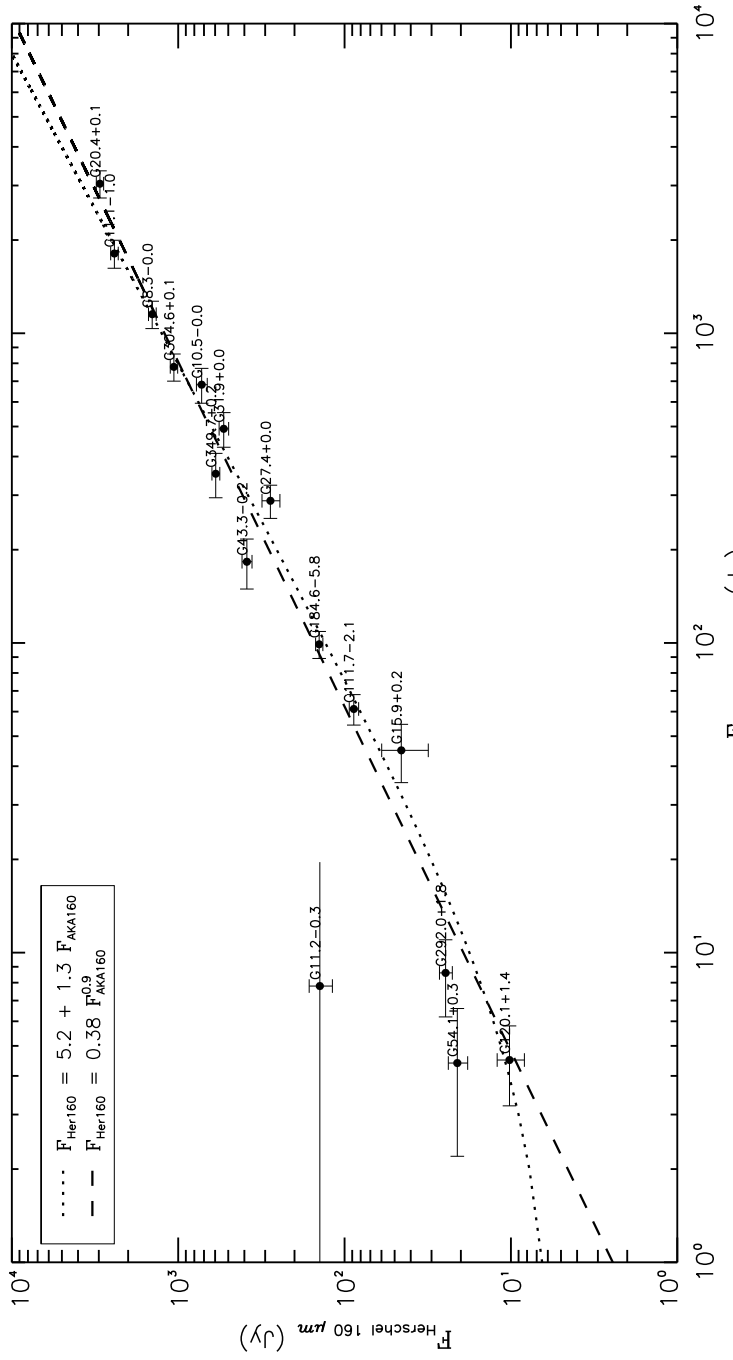

Figure 4.9 Correlation between *AKARI* 160 μm and *Herschel* 160 μm fluxes. The dotted and dashed lines show linear and power-law fitting results in logarithmic scale.

the $AKARI$ 65 μm, but overall tendency was well defined in linear functions. The correlation between the $Herschel$ 70 μm and $Spitzer$ 70 μm fluxes showed a clear positive relation (Fig. 4.8). To find their data consistency, we used 19 targets and found the slope of about 1.5 in logarithmic scale. The $Herschel$ 70 μm fluxes were relatively stronger than the $Spitzer$ 70 μm fluxes. In case of $Spitzer$ 70 μm data, large systematic uncertainties were known from non-linear response of detectors, stripe patterns of the images, and large uncertainty of brightness. This non-linearity could be attributed to underestimate the $Spitzer$ 70 μm photometric fluxes.

We also compared the same wavelength data of the $AKARI$ and $Herschel$ at 160 μm, and the result was shown in Fig. 4.9. This correlation was well described by linear fitting methods, but the far-IR fluxes of less than about 10 Jy from the $AKARI$ 160 μm data showed a much larger dispersion from fitting slopes, because the measured fluxes of these targets could be strongly affected by the background fluctuation.

From the comparison results between the $AKARI$, $Herschel$, and $Spitzer$ data, we could find that these data showed good correlations in the linear and power-law fitting methods, but there were flux differences, especially, in $AKARI$ bands. When we considered the differences between the $AKARI$ and other data, the $AKARI$ fluxes were fairly lower than the other data. In case of the $AKARI$, we used Ver. 2.0 data which was not a final version of the $AKARI$ data. To check the flux differences of $AKARI$ data, we took sample data of a recent version (Ver. 2.1) and compared the fluxes using the same methods of our flux estimations. We found that the new version of the $AKARI$ data showed that the fluxes were slightly increased than our results, but flux ratios were almost similar values compared with our results. In this study, we only used the $AKARI$ fluxes for ratios to find systematic studies, so our ratio results of the $AKARI$ did not show big differences compared with recent data.

In previous study, Tóth et al. (2014) reported that they found positional errors comparing the $2MASS$, $WISE$, and $AKARI$ point source catalogs and flux devia-

tions between observed and model flux densities. We also calculated the astrometric offsets among the bright sources scattered in galactic longitude from 20° to 340° at every 20° to 40° using *AKARI* 65 μm band images comparing with *IRAS* and *MSX* point source catalogs. From our test of the preliminary data set, we found that there were astrometric offset. The range of positional differences toward the inner galactic region ($l < |60°|$) was between 10″ and 30″, corresponding to about 1−2 pixels of the *AKARI* images, but the offset in the outer region was less than a pixel size. From this test, we found that the astrometric offset toward the inner Galactic regions showed much larger than the outer regions. Therefore, if we can use corrected data of the *AKARI*, the flux values and correlations could be better results than the current version of the data.

4.3.5 Far-IR Color-Color Diagrams

We have used the far-IR color-color diagrams of the well-defined SNRs to derive the characteristics for the SNRs using the estimated fluxes from the *Spitzer*, *AKARI*, and *Herschel* data. The far-IR colors of the detected SNRs between [F_{Her70}/F_{Her160}] and [F_{Her250}/F_{Her350}] are presented in Fig. 4.10. We also compared the colors of the SNR with other Galactic sources using published HII region and PNe catalogs from the Herschel Hi-GAL survey (Anderson et al. 2011). We found that the young SNRs less than 1000 yr old (e.g. Cassiopeia A, Tycho, and Crab) were perfectly separated from the other old remnants and other Galactic sources. In the case of the young SNRs, their color ratio of [F_{Her70}/F_{Her160}] was higher than 1 and [F_{Her250}/F_{Her350}] was lower than 2, respectively. The other SNRs and HII regions were located at higher [F_{Her250}/F_{Her350}] ratio with an appropriate slope and wide temperature range, and their distributions did not show any distinct separation into their own groups from this far-IR colors. The dust temperature range are defined by a modified blackbody radiation model ($S \propto B{\cdot}\nu(T)^{\beta}$) with single temperature assuming $\beta \sim 2$. From this group, the interacting SNRs with MCs were mixed without distinct characteristics. The color ratio between [F_{AKA65}/F_{AKA90}]

and [F_{Her250}/F_{Her350}] showed similar distributions comparing with the former ratio. In previous *IRAS* studies, Arendt (1989) and Saken et al. (1992) found a distinct location of the young SNRs from the color-color diagram between the [*IRAS* 25/60 μm] and [*IRAS* 60/100 μm]. From our result, we revealed that the color-color diagram using the far-IR data could also provide one of the effective means to define the young SNRs.

The color-color diagram of the *Spitzer* flux ratio against the *AKARI* and *Herschel* flux ratios were shown in Fig. 4.11. The young SNRs and intermediate SNR aged from 1000 to 4000 yr (e.g. G11.2, G15.9, G54.1, and G292) were distributed at upper part of the color-color diagram from [F_{Spt24}/F_{Spt70}] and [F_{Her70}/F_{Her160}] ratios. The results between [F_{Spt24}/F_{Spt70}] and [F_{AKA90}/F_{AKA140}] were also similar color distributions. In these color-color diagrams, interacting SNRs with MCs were relatively lower part of the diagram and mixed with other remnants. These tendencies were already reported in the mid-infrared study of the SNRs in the inner Galaxy using *Spitzer* 8, 24, and 70 μm data (Pinheiro Gonçalves et al. 2011). From their studies, old remnants had higher colors between [F_{Spt70}/F_{Spt24}] and [F_{Spt8}/F_{Spt24}], and the interacting SNRs with MCs showed relatively higher color distributions than ionic-line-dominant SNRs based on surface brightness correlations between [I_{Spt8}/I_{Spt24}] and [I_{Spt70}/I_{Spt24}], but these colors did not give any direct evidence to classify different origins of far-IR emissions. In these color-color diagrams, the interacting SNRs were located at the lower value of [F_{Spt24}/F_{Spt70}] ratio than the young SNRs without any characteristics of the *Herschel* and *AKARI* colors. We could roughly find the distributions between the interacting SNRs with MCs and the young SNRs from these color-color diagrams, but these results did not give any constraint to divide the characteristics of the SNRs.

In fig. 4.12, the color-color diagrams of the *AKARI* and *Herschel* data sets were described. From the *AKARI* colors between [F_{AKA65}/F_{AKA90}] and [F_{AKA90}/F_{AKA140}], most SNRs were concentrated on the temperature range from 25 to 50 K without any distinct separation between young and other SNRs. The young SNRs were dis-

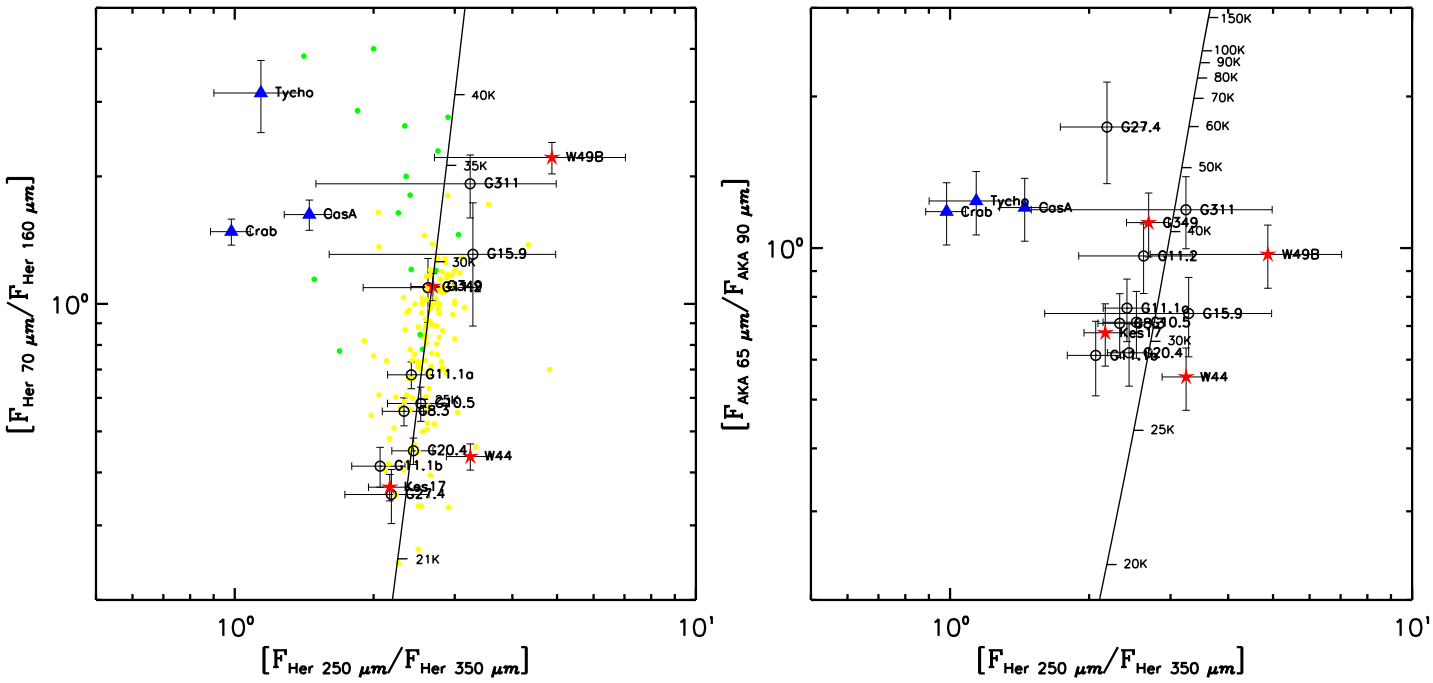

Figure 4.10 *AKARI* and *Herschel* color-color diagrams. (left) *Herschel* [F70/F160] flux ratio vs. *Herschel*[F250/F350] flux ratio, and (right) *AKARI* [F65/90] flux ratio vs. *Herschel* [F250/F350] for 16 SNRs from this survey. Blue triangles and red star marks indicate young and interacting SNRs with molecular clouds, respectively. Open circles are the rest of the detected SNRs. Filled yellow and green circles represent HII regions and PNe. Solid line shows dust temperature from modified blackbody radiation model ($\beta \sim 2$).

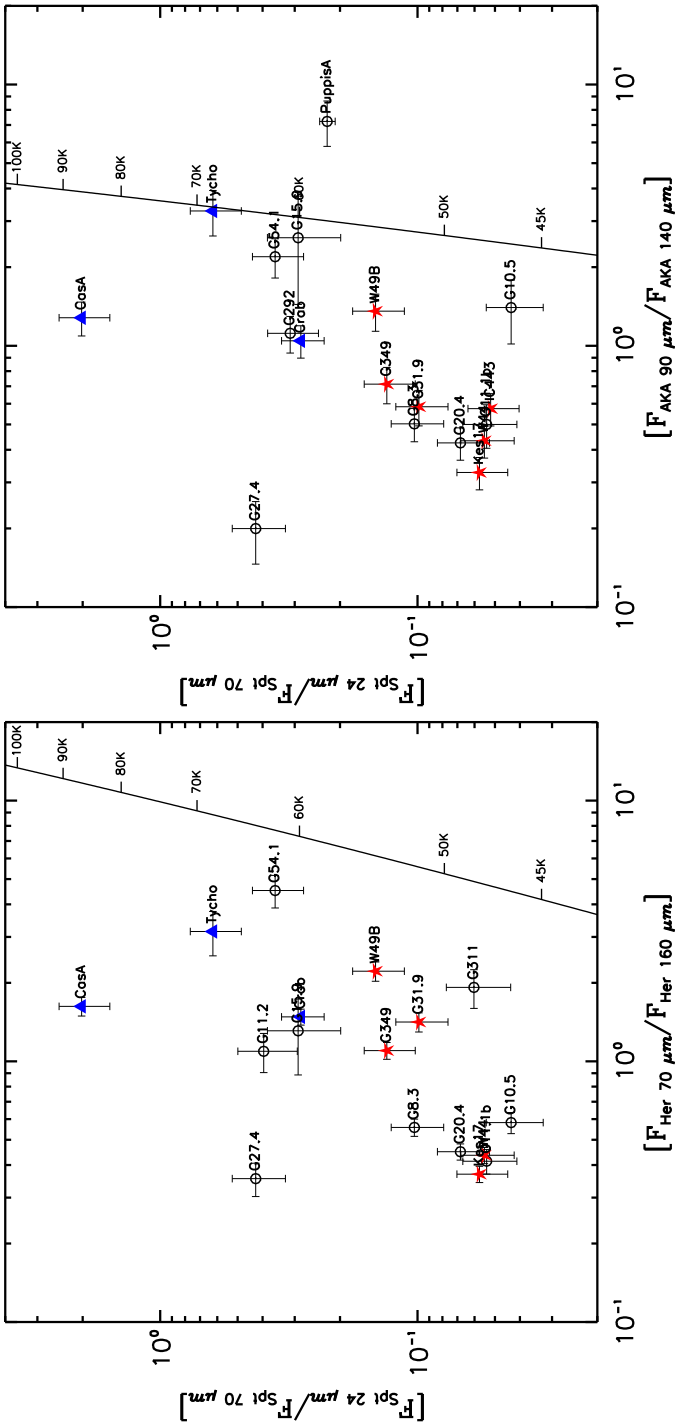

Figure 4.11 Color-color diagrams from the detected SNRs using *Spitzer*, *AKARI*, and *Herschel* fluxes. (left) *Spitzer* [F24/F70] vs. *Herschel* [F70/F160] flux ratio from 17 SNRs. (right) *Spitzer* [F24/F70] vs. *AKARI* [F90/F140] flux ratio from 18 SNRs. The meaning of the symbols and the line are same as those of fig. 4.2.

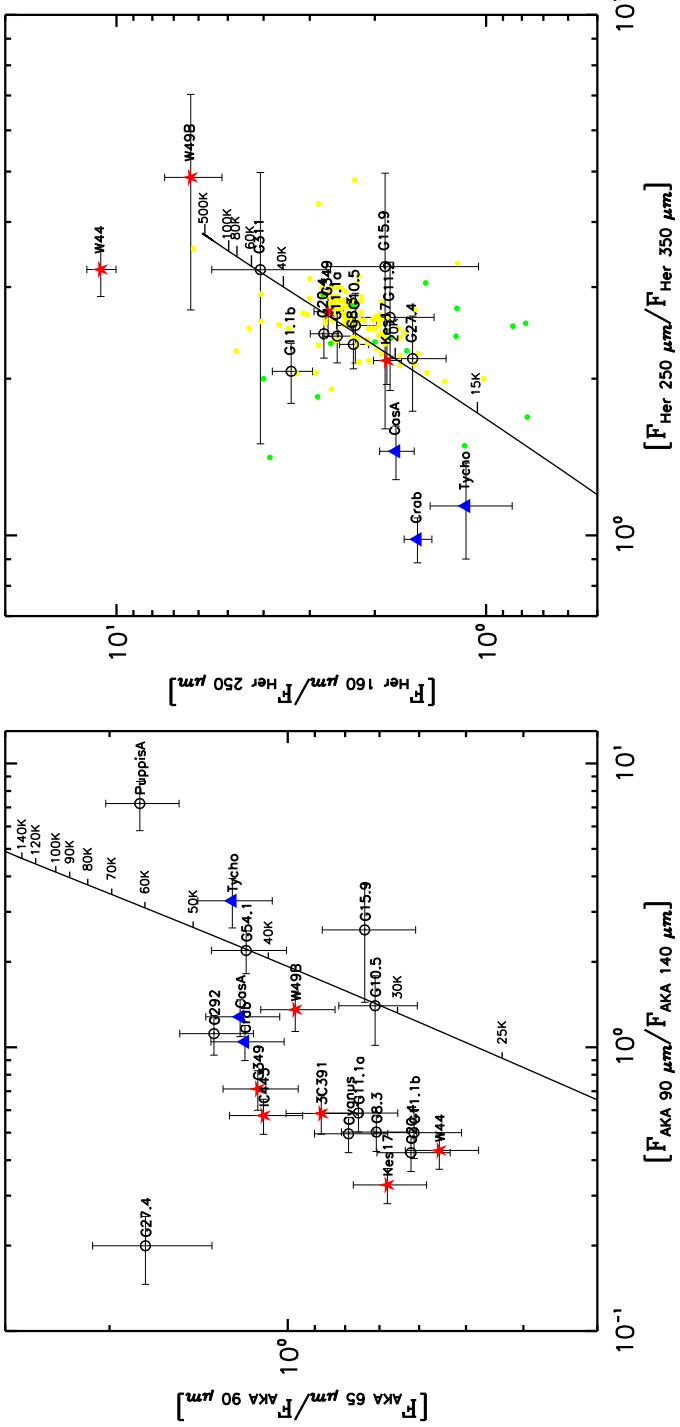

Figure 4.12 Color-color diagrams from the detected SNRs. (left) *AKARI* [F65/F90] vs. *AKARI* [F90/F140] flux ratio from 18 SNRs. (right) *Herschel* [F160/F250] vs. *Herschel* [F250/F350] flux ratio from 18 SNRs. The meaning of the symbols are same as those of fig. 4.2.

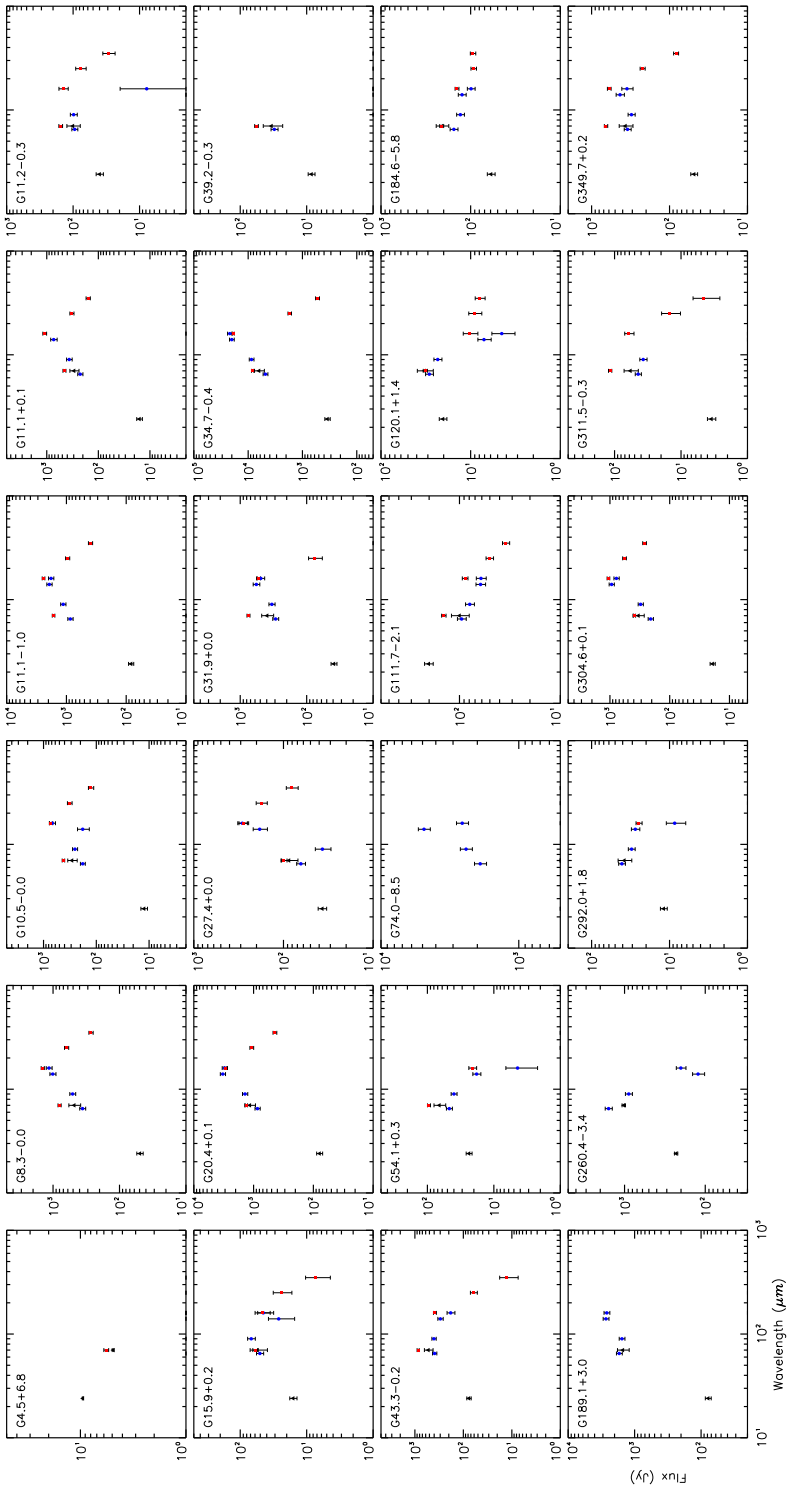

Figure 4.13 SEDs of 24 selected SNRs. Symbols represent observed data of SNRs. Blue circles and Red boxes show *AKARI* FIS (65, 90, 140, 160 μm) and *Herschel* PACS/SPIRE (70, 160, 250, and 350 μm) results from this study. Black triangles indicate *Spitzer* MIPS (24 and 70 μm) fluxes and some fluxes are taken from Pinheiro Gonçalves et al. (2011). More detailed explanations are in Table. 4.3.

tributed in narrow temperature ranges between 40 and 50 K, but the other SNRs were also located in this ratio region. From the color distributions between [F_{Her160}/ F_{Her250}] and [F_{Her250}/F_{Her350}] ratios, the young SNRs were located at about 1 in the diagram with similar tendencies of the *AKARI* result. This could be due to the fact that the flux variations of young SNRs were decreased gradually. These SNRs were also shown distinct distribution from old SNRs and other Galactic sources. The peak fluxes of the young and intermediate SNRs typically decreased with increasing wavelength after $\sim 60\ \mu m$. The spectral energy distributions (SEDs) of the detected targets were represented in Fig. 4.13, and these were more detailed and clearly defined than in previous *IRAS* studies (Arendt 1989; Saken et al. 1992). In case of the other SNRs, after reaching the peak flux between 140 and 160 μm, their fluxes were decreased steeply toward longer wavelengths. From the color-color diagrams using far-IR fluxes, several targets, especially in case of old SNRs, were not defined as a single temperature model and the dust properties are not expected to be at single temperature, so we need more detailed analysis of the fluxes from the detected SNRs.

4.3.6 Far-IR and Radio Flux Correlations

We examined the correlations between the fluxes at the far-IR and the radio bands. For the comparisons, we used the 1 GHz radio fluxes estimated from observed multi-frequency radio spectra listed in the Green's catalog of Galactic SNRs (Green 2014). Figs. 4.14 and 4.15 show the distributions of the SNRs at each wavelength and their fitting results in the logarithmic scale. From the relations, we were able to find that young SNRs were separated from the other SNRs and located at distinct position. Our results showed that the young SNRs are located at the lowest ratio region ($[F_{65,70,160\mu m}/F_{1GHz}] < 1$) with slope ranges between 0.5 and 0.8. The separations between young and old SNRs were almost same characteristics as a previous study of ratios between the *IRAS* at 60 μm and Radio at 1 GHz with values of less than

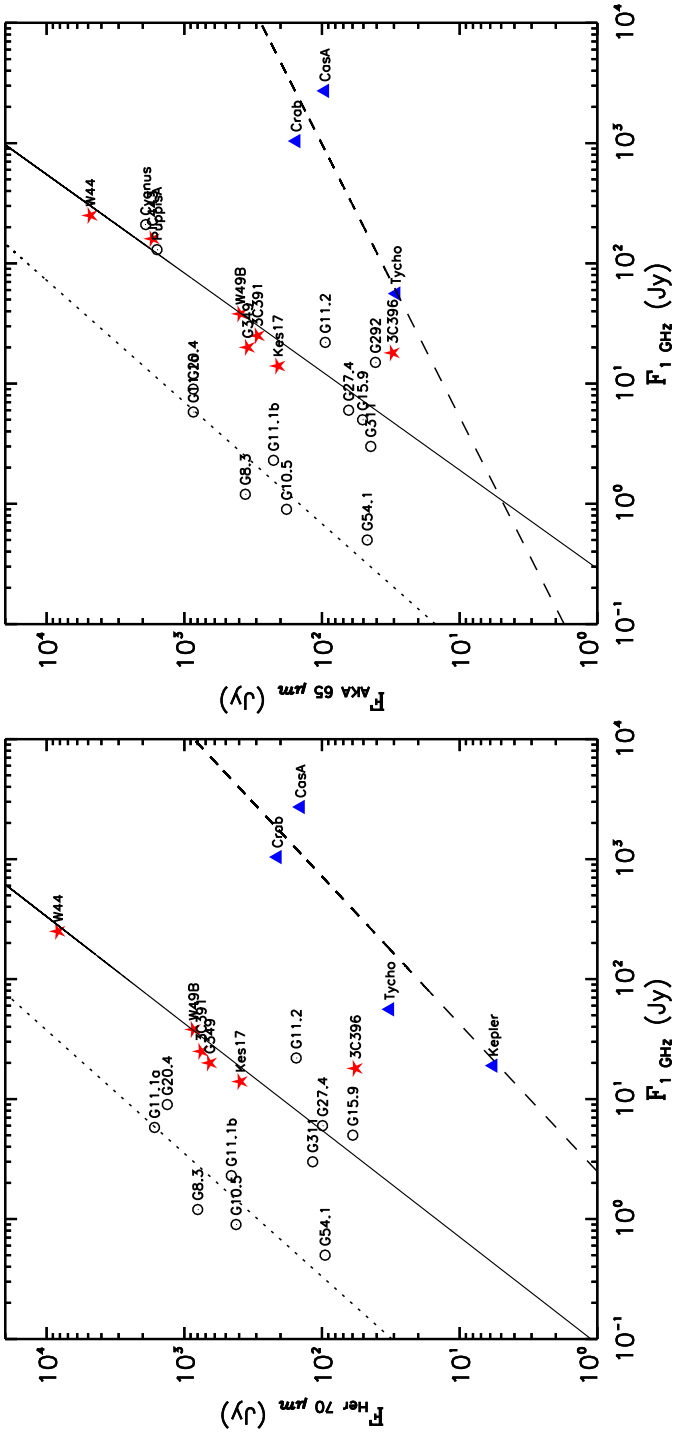

Figure 4.14 The relation of the *Herschel* 60 μm (right) and *AKARI* 65 μm (left) far-IR fluxes with 1 GHz radio fluxes. The dashed and dotted lines represent the linear fitting results of logarithmic scale in the ratio of $[F_{60,65\mu m}/F_{1GHz}]$ < 1 and > 100, respectively. The solid line shows the linear fitting result of SNRs in a ratio range between 1 and 50. The meaning of the symbols are same as those of fig. 4.2.

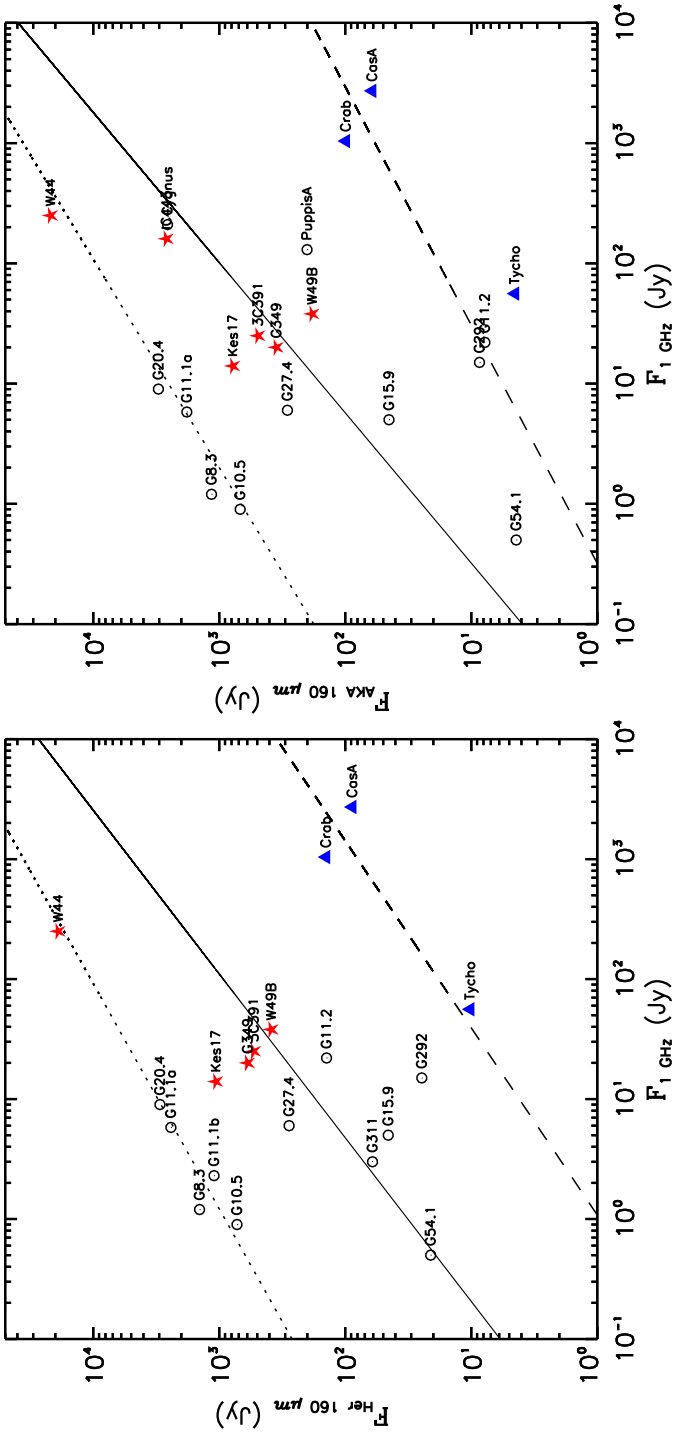

Figure 4.15 The relation of the *Herschel* 160 μm (right) and *AKARI* 160 μm (left) far-IR fluxes with 1 GHz radio fluxes. Each of the dashed and dotted lines indicate the linear fitting results in logarithmic scale from the ratio of $[F_{60,65\mu m}/F_{1GHz}] < 1$ and > 100, respectively. The solid line shows the linear fitting result of SNRs in a ratio range between 1 and 50. The meaning of the symbols are same as those of fig. 4.2.

Table 4.4. Relation of fluxes between far-IR and 1 GHz radio continuum

log F_{1GHz}									
Ratio[a]	log F_{Her70}		log F_{AKA65}		Ratio[a]	log F_{Her160}		log F_{AKA160}	
	A	B	A	B		A	B	A	B
R < 1	-0.32 ± 0.41	0.81 ± 0.17	0.68 ± 0.13	0.44 ± 0.11	R < 1	-0.02 ± 0.48	0.64 ± 0.19	0.25 ± 0.18	0.50 ± 0.09
1 < R < 50	1.17 ± 0.18	1.12 ± 0.09	0.66 ± 0.26	1.22 ± 0.13	1 < R < 100	1.50 ± 0.16	0.73 ± 0.12	1.39 ± 0.28	0.80 ± 0.17
R > 100	2.47 ± 0.10	0.97 ± 0.17	2.16 ± 0.10	0.99 ± 0.14	R > 100	2.96 ± 0.06	0.53 ± 0.07	2.87 ± 0.07	0.58 ± 0.04

Note. — Ratio ranges (R) are defined from $[F_{far-IR}/F_{1GHz}]$. Linear fitting results for each ratio ranges are shown in logarithmic scale using the equation $log\ F_{1GHz} = A + B\ log\ F_{far-IR}$, where A and B are constant and slope, respectively.

1 (Arendt 1989). In this study, we found that the rest of the SNRs were divided into two groups from the $[F_{65,70,160\mu m}/F_{1GHz}]$ relations. The known interacting SNRs with MCs and old SNRs were concentrated on the ratio ranges between 1 to 50 with linear slopes of 1.12 and 1.22. From the comparisons with 160 μm fluxes of the $Herschel$ and $AKARI$, the MC-interacting SNRs were located at the ratio range from 1 to 100 with slopes of 0.73 and 0.80 in logarithmic scale. In the ratio ranges from 1 to 50 or 100, there were also contained in old SNRs, which were not known about interacting features with their environments. Their morphological distributions were no significant differences in comparing with the interacting SNRs with MCs, but their far-IR fluxes were relatively lower. The last group is other SNRs which is located at the ratio value over 100 with slope ranges between 0.5 and 1.0. In this group, young SNRs and the interacting SNRs with MCs were not included.

From the flux comparisons of the far-IR and radio data, we could separate the three groups of the SNRs from the relations. In overall tendency, the intermediated region included the interacting SNRs with MCs tended to show steeper slope compared with the young and other SNRs. Table. 4.4 showed the summary of the linear fitting results for each ratio ranges in logarithmic scale. We will discuss a possible explanation about the distinction of interacting SNRs with MCs from the ratio between far-IR and radio relations in section 4.4.2.

4.4 Discussion

4.4.1 Far-IR Characteristics of Galactic SNRs

From our survey, we identified 49 out of 294 Galactic SNRs showing well-defined morphologies or partially bright features in the $AKARI$ and $Herschel$ far-IR bands. In the previous $IRAS$ survey, Arendt (1989) and Saken et al. (1992) found about 30 out of 160 SNRs which shows the well-defined IR morphologies. From the $Spitzer$ survey of the inner Galactic plane, 18 and 39 SNRs were identified in the IRAC and

MIPS bands, respectively (Reach et al. 2006; Pinheiro Gonçalves et al. 2011). When our result compared with the previous infrared studies, the detected SNRs were more increased than those of surveys. The high detection efficiency in far-IR bands was possible due to higher resolution data sets with better sensitivity of detector and wide coverage area of survey data.

To understand the characteristics of far-IR bright SNRs, we select 24 targets which showed well-defined far-IR morphology identified from the comparisons with radio and X-ray data. In many cases of SNRs, their morphological similarities are shown at far-IR and X-ray wavelengths. These remnants showed a bright shell structure with a good spatial correlation between far-IR and X-ray emissions. The spatial distributions of these SNRs indicated that the far-IR emissions originated from dust grains heated by electronic collisions in the same area of X-ray emitting regions (Dwek et al. 1987, 2008). On the other hand, the Crab SNR is significantly different morphology from other SNRs. This remnant show filamentary structures are almost similar distributions in far-IR and radio bands. In this case, most IR emissions are heated and boosted by central radiation by pulsar rather than collisional heating processes (Dwek & Werner 1981).

In case of SNRs interacting with MCs, their far-IR morphology was clearly different from X-ray distributions compared with other SNRs. Their distributions in far-IR and radio bands showed (partial) shell-like structures with an X-ray bright central emission region. The enhancement of far-IR emissions toward SNRs could be strong evidence for shocked dense region (Draine 1981; Lee et al. 2011). The SNR IC443 is a typical case of the interacting SNRs with MCs showing bright far-IR shells. According to the multi-wavelength studies, IC443 showed multiple shell structures interacting with the ISM (Braun & Strom 1986; Mufson et al. 1986). In CO observation, this remnant shows broad CO emission lines from the shocked regions (Snell et al. 2005; Lee et al. 2012). The bright far-IR emissions were also detected at the prominent shocked molecular region. The enhanced far-IR emission can be come from the dust emission heated by strong UV radiation of cooling post-

shock gas and the dust emission in evaporating flows of molecular clouds engulfed by hot gas (Lee et al. 2011).

From this systematic survey, we were able to consider the heating process of the dust grain comparing with the morphological distributions of the SNRs in far-IR, radio, and X-ray bands. However, more detailed studies are needed to understand the dust heating processes from individual SNRs using muti-wavelength data.

4.4.2 Far-IR and Radio Relations of Interacting SNRs with Molecular Clouds

From the comparisons between far-IR and radio fluxes, we could find the distinct distributions between young and old SNRs. The physical mechanisms between far-IR and radio emissions are not directly connected, but the relations of the far-IR and radio fluxes showed interesting distributions. From these results, a possible case for explaining the relation could be that the IR-to-radio ratios represent the evolutionary track of SNRs. From observational and statistical studies using radio supernovae, Weiler et al. (1986) derived radio light curves of radio supernovae through their models.

The type II SNe showed a decline of radio flux density ($\sim t^{-0.7}$) with time after maximum and the type I SNe showed much steeper rates of decline ($\sim t^{-1.6}$). On the other hand, IR emissions might be corresponded to the mass of the swept-up dust at fixed dust temperature, and the IR luminosity will increase steadily as $t^{1.71}$ (Chevalier 1982; Dwek et al. 1987). Therefore, the observational results of the relations between far-IR and radio fluxes might be able to explain roughly the distribution of young to old SNRs, but the results for such MC-interacting SNRs with old age (e.g. W44 and IC443) located at the ratio range between 1 and 50 or 100 are not able to explain using evolutionary procedure of the remnant.

In case of interacting SNRs with MCs, we can think that the radio enhancements in the shocked regions between the SNR and the ambient MCs. The environmental effects of these SNRs might be explained by their distinct locations in the rela-

tions. In previous study of SNR G89.0+4.7 (HB 21), unusual radio features having a V-shaped structure, bright knots, and a ring-like structure are shown at the interacting regions where the broad CO line emission were detected (Byun et al. 2006). These features could be the results from shock-cloud interaction, and their morphology was expected from the numerical simulation. Jun & Jones (1999) represented when the molecular cloud is engulfed by the SNR, a magnetic field amplification near the cloud becomes stronger than any other region, so the radio emissivity can significantly increase at the shocked region. Therefore, the old SNRs interacting with MCs could stay longer than other SNRs at the intermediate ratio region ($1 < [F_{65,70,160\mu m}/F_{1GHz}] < 100$). The relations between far-IR and radio flux densities give useful tools for identifying the young SNRs and understanding the properties of interacting SNRs with MCs, but more detailed analysis needs to be conducted to understand these relations.

4.4.3 Possible correlations between radio and far-IR bands in interacting SNRs with MCs

An interacting SNR with molecular clouds is shown with some typical evidences such as the detection of maser emission, broad line wings, and IR emissions (Reach et al. 2005). Enhanced far-IR emissions toward SNRs could be also strong evidence for a shocked dense region. The far-IR emission from the swept-up dust is the major coolant of an SNR. This far-IR bright region could be due to the radiative shocks heating from the shock front and dust emission in the vicinity of molecular clouds illuminated by radiative shock (Drain 1981; Lee et al. 2011). This interaction can be shown as spatial coincidence between far-IR and radio emissions. Huang et al. (1986) has found that far-IR point sources showed good spatial correlation with shocked CO clumps in IC 443. Also followed works have confirmed there is positional coincidence between far-IR emission and shocked CO molecular clouds near the remnant with low resolution data (e.g., Yamamoto et al. 1999; Dubner et al. 2004). While, thanks to high resolution data with the GMRT and *Herschel*, Supan et al. (2015) was able

to look at more detail features and they showed the spatially coincidence between molecular cloud or radio continuum and far-IR at small scale (see Fig 4 (a) of Supan et al. (2015)). From their studies, they found interacting region the coincidence between radio and far-IR detection at small and large scale has supported SNR nearby molecular cloud interaction. In case of SNR Kes 17, it is a typical case of interacting SNRs with MCs showing bright far-IR features at the western shell of the remnant. This SNR shows partial shell structure in radio continuum with centrally-brightened X-ray emission and detected OH maser emission which is direct evidence of interaction with MCs (Shaver& Goss 1970; Frail et al. 1996; Lee et al. 2011; Gök & Sezer 2012).

The far-IR bright SNRs are particularly interesting targets; however, every shocked gas is not correlated with far-IR emission, so it is not easy to conclude that there is tight correlation (i.e., 3 out of 7 in Huang et al. (1986); 6 out of 17 in Yamamoto et al. (1999)). Previous studies also have worked on individual targets thus it was not enough to show their connection systematically, so more data are needed to reveal the shocked evidence at far-IR bright region for understanding the interaction between the SNR and the ambient molecular gas. Moreover, if we can reveal the shocked region and define the type of shock, the process of dust destruction at the far-IR bright region will be studied from the CO molecular line observation and allow us to understand the physical and kinematical properties of interacting SNRs with MCs comparing radio and far-IR data.

4.5 Summary

We carry out a systematic study of Galactic SNRs using the *AKARI* and *Herschel* far-IR survey data. The *AKARI* Infrared Astronomical Satellite observed the whole sky using the four FIS bands covering 50 to 180 microns with $\sim$1 arcmin resolution and the *Herschel* Space Observatory provided the Galactic plane data with higher resolution ($<$ 0.5 arcmin) and better sensitivity using the four wavelength bands

at 70 to 250 microns. These data provided an unprecedented opportunity to study diffuse, extended far-IR sources such as SNRs. We have searched for far-IR counterparts to all 294 known Galactic SNRs, and investigated their far-IR properties of identified SNRs. Our primary results are as follows.

1. The *AKARI* and *Herschel* data were used to search for the associated far-IR features with SNRs comparing with radio continuum and X-ray data by visual inspection. According to our results of identification, 59 out of 294 SNRs show bright far-IR features.

2. The spatial distributions of the detected SNRs were mainly located at the Galactic longitude from -60° to 60° and latitude from –0.5° to 0.5° since we could hardly define the far-IR sources near the Galactic center and Galactic plane suffered from IR confusion along the line of sight. We expected that the detection rate in the outer Galactic region could be much higher than the inner Galaxy, because the outer SNRs suffer little IR confusion or extinction than the inner SNRs, but the results of the detection rates were not reflected in the effect of IR contamination along the sight line toward the remnants.

3. Using the estimated far-IR fluxes from the detected SNRs, the far-IR color-color diagrams and the ratio of far-IR and radio relations show distinct distributions of the young SNRs, old SNRs, and interacting SNRs with MCs. The young SNRs were clearly separated from other SNRs in the color-color diagrams. In case of interacting SNRs with MCs, these are concentrated on the ratio ranges of far-IR to radio fluxes between 1 and 50 or 100 with strong far-IR emissions.

Bibliography

Abdo, A. A., Ackermann, M., Ajello, M., et al. 2009a, ApJS, 183, 46

Abdo, A. A., Allen, B. T., Aune, T., et al. 2009b, ApJ, 700, L127

Abdo, A. A., Ackermann, M., Ajello, M., et al. 2010, ApJS, 188, 405

Abdo, A. A., Allen, B. T., Atkins, R., et al. 2012, ApJ, 750, 63

Acciari, V. A., Aliu, E., Arlen, T., et al. 2009, ApJ, 698, L133

Acciari, V. A., Aliu, E., Arlen, T., et al. 2010a, ApJ, 714, 163

Acciari, V. A., Aliu, E., Arlen, T., et al. 2010b, ApJ, 719, L69

Acciari, V. A., Aliu, E., Arlen, T., et al. 2011, ApJ, 730, L20

Ackermann, M., Ajello, M., Allafort, A., et al. 2013, ApJS, 209, 34

Albert, J., Aliu, E., Anderhub, H., et al. 2006a, ApJ, 637, L41

Albert, J., Aliu, E., Anderhub, H., et al. 2006b, ApJ, 643, L53

Albert, J., Aliu, E., Anderhub, H., et al. 2007, A&A, 474, 937

Albert, J., Aliu, E., Anderhub, H., et al. 2007, ApJ, 664, L87

Aleksić, J., Alvarez, E. A., Antonelli, L. A., et al. 2012, A&A, 540, AA69

Aleksić, J., Ansoldi, S., Antonelli, L. A., et al. 2014, A&A, 567, L8

Aliu, E. 2011, International Cosmic Ray Conference, 7, 228

Aliu, E., Archambault, S., Arlen, T., et al. 2013a, ApJ, 764, 38

Aliu, E., Archambault, S., Arlen, T., et al. 2013b, ApJ, 770, 93

Anderson, L. D., Zavagno, A., Barlow, M. J., Garcia-Lario, P., & Noriega-Crespo, A. 2011, VizieR Online Data Catalog, 353, 70001

Araya, M. 2013, MNRAS, 434, 2202

Archer, A., Barnacka, A., Beilicke, M., et al. 2014, ApJ, 790, 149

Arendt, R. G. 1989, ApJS, 70, 181

Arendt, R. G., Dwek, E., Blair, W. P., et al. 2010, ApJ, 725, 585

Blair, W. P., Ghavamian, P., Long, K. S., et al. 2007, ApJ, 662, 998

Braun, R., & Strom, R. G. 1986, A&AS, 63, 345

Byun, D.-Y., Koo, B.-C., Tatematsu, K., & Sunada, K. 2006, ApJ, 637, 283

Casandjian, J.-M., & Grenier, I. A. 2008, A&A, 489, 849

Chen, A. W., Piano, G., Tavani, M., et al. 2011, A&A, 525, AA33

Chevalier, R. A. 1982, ApJ, 258, 790

Dickel, J. R., Eilek, J. A., Jones, E. M., & Reynolds, S. P. 1989, ApJS, 70, 497

Doi, Y., Komugi, S., Kawada, M., et al. 2012, Publication of Korean Astronomical Society, 27, 111

Draine, B. T. 1981, ApJ, 245, 880

Dubner, G., Giacani, E., Reynoso, E., & Parón, S. 2004, A&A, 426, 201

Dwek, E., Arendt, R. G., Bouchet, P., et al. 2008, ApJ, 676, 1029

Dwek, E., Petre, R., Szymkowiak, A., & Rice, W. L. 1987, ApJ, 320, L27

Dwek, E., & Werner, M. W. 1981, ApJ, 248, 138

Ferrand, G., & Safi-Harb, S. 2012, Advances in Space Research, 49, 1313

Frail, D. A., Goss, W. M., Reynoso, E. M., et al. 1996, AJ, 111, 1651

Giordano, F., Naumann-Godo, M., Ballet, J., et al. 2012, ApJ, 744, L2

Gök, F., & Sezer, A. 2012, MNRAS, 423, 1215

Gomez, H. L., Krause, O., Barlow, M. J., et al. 2012, ApJ, 760, 96

Green, D. A. 2014, Bulletin of the Astronomical Society of India, 42, 47

Hartman, R. C., Bertsch, D. L., Bloom, S. D., et al. 1999, ApJS, 123, 79

Hines, D. C., Rieke, G. H., Gordon, K. D., et al. 2004, ApJS, 154, 290

Huang, Y.-L., Dickman, R. L., & Snell, R. L. 1986, ApJ, 302, L63

Jeong, I.-G., Byun, D.-Y., Koo, B.-C., et al. 2012, Ap&SS, 342, 389

Jeong, I.-G., Koo, B.-C., Cho, W.-K., et al. 2013, ApJ, 770, 105

Jiang, B., Chen, Y., Wang, J., et al. 2010, ApJ, 712, 1147

Jun, B.-I., & Jones, T. W. 1999, ApJ, 511, 774

Kawada, M., Baba, H., Barthel, P. D., et al. 2007, PASJ, 59, 389

Lee, H.-G. 2005, JKAS, 38, 385

Lee, H.-G., Moon, D.-S., Koo, B.-C., et al. 2011, ApJ, 740, 31

Lee, J.-J., Koo, B.-C., Snell, R. L., et al. 2012, ApJ, 749, 34

Molinari, S., Swinyard, B., Bally, J., et al. 2010, PASP, 122, 314

Mufson, S. L., McCollough, M. L., Dickel, J. R., et al. 1986, AJ, 92, 1349

Nolan, P. L., Abdo, A. A., Ackermann, M., et al. 2012, ApJS, 199, 31

Pinheiro Gonçalves, D., Noriega-Crespo, A., Paladini, R., Martin, P. G., & Carey, S. J. 2011, AJ, 142, 47

Pittori, C., Verrecchia, F., Chen, A. W., et al. 2009, A&A, 506, 1563

Reach, W. T., Rho, J., & Jarrett, T. H. 2005, ApJ, 618, 297

Reach, W. T., Rho, J., Tappe, A., et al. 2006, AJ, 131, 1479

Rho, J., & Petre, R. 1998, ApJ, 503, L167

Saken, J. M., Fesen, R. A., & Shull, J. M. 1992, ApJS, 81, 715

Shaver, P. A., & Goss, W. M. 1970, AuJPA, 14, 133

Snell, R. L., Hollenbach, D., Howe, J. E., et al. 2005, ApJ, 620, 758

Supan, L., Castelletti, G., Joshi, B. C., Surnis, M. P., & Supanitsky, D. 2015, A&A, 576, A81

Torres, D. F., Romero, G. E., Dame, T. M., Combi, J. A., & Butt, Y. M. 2003, Phys. Rep., 382, 303

Tóth, L. V., Marton, G., Zahorecz, S., et al. 2014, PASJ, 66, 17

VERITAS Collaboration, Aliu, E., Arlen, T., et al. 2011, Science, 334, 69

Verrecchia, F., Pittori, C., Chen, A. W., et al. 2013, A&A, 558, A137

Weiler, K. W., Sramek, R. A., Panagia, N., van der Hulst, J. M., & Salvati, M. 1986, ApJ, 301, 790

Wu, J. H. K., Wu, E. M. H., Hui, C. Y., et al. 2011, ApJ, 740, LL12

Yamamoto, F., Hasegawa, T., Morino, J., et al. 1999, Star Formation 1999, 110

Yuan, Q., Huang, X., Liu, S., & Zhang, B. 2014, ApJ, 785, LL22

Chapter 5

Summary and Conclusion

This thesis has been conducted in order to understand physical and dynamical evolution of interacting supernova remnants (SNRs) with molecular clouds (MCs) and their ambient medium. To study physical and morphological characteristics for the interacting SNRs with MCs, CO and IR studies have provided the helpful information. For detailed studies, however, a systematic study for Galactic SNRs with high resolution and wide *l*-*b* coverage in CO and Infared (IR) are needed. Recently, far-Infrared (far-IR) data of all-sky survey (*Spitzer*, *AKARI*, and *Herschel*) are available for the study of the correlation between CO and IR in SNR-MC association. In this thesis, I have studied interacting SNRs with MCs using CO and far-IR data. More specifically, I have carried out a CO survey of Galactic SNRs, found clear evidence of molecular clouds interacting with SNR 3C434.1, produced a far-IR catalog of Galactic SNRs, and studied far-IR properties of interacting SNRs with MCs.

In chapter 2, I have carried out a systematic ^{12}CO $J = 1-0$ observation of Galactic SNRs using the Seoul Radio Astronomy Observatory (SRAO) 6-m telescope. I observed 11 SNRs satisfying our selection criteria among the 35 targets in $l = 70^{\circ}$ to 190° (Green 2004): G73.9+0.9, G76.9+1.0, G84.2−0.8, G85.4+0.7, G85.9−0.6, G93.3+6.9 (DA530), 94.0+1.0 (3C434.1), 166.2+2.5 (OA184), 179.0+2.6, 180.0−1.7

(S147), and G182.4+4.3. The mapping is performed either in half-beam or full-beam sampling to cover the full extents of individual SNRs in the radio continuum. I found CO molecular clouds having spatial correlations with radio emission in 6 SNRs: G73.9+0.9, G84.2−0.8, G85.4+0.7, G93.3+6.9, G94.0+1.0, and G182.4+4.3. However, no strong evidence for the interaction, e.g., broad wings or high-velocity shocked gas, was detected for these objects. From CO survey, two SNRs are particularly interesting. In G85.4+0.7, there is a filamentary molecular cloud aligned along the south-east boundary of the remnant. This cloud extends to the nearby HII region G84.9+0.5. If the molecular cloud is associated with both HII region and the SNR, the distance to SNR would be 5−7 kpc. In 3C434.1, there is a large molecular cloud blocking the western half of the remnant where the radio continuum emission is faint. The cloud shows a very good spatial correlation with radio feature, which strongly suggests the physical association of the cloud with the SNR. This gives a distance of 3 kpc to the SNR. Such anti-correlation between a molecular cloud and radio emission was previously found in the SNR CTB109 (G109.1-1.0), and the their association is likely. Further observations are needed to confirm the interaction between molecular clouds and these SNRs.

In chapter 3, I present the results of CO study of 3C434.1 (G94.0+1.0) which gives a picture of the SNR significantly different from the previous HI studies. We performed ^{12}CO $J = 1-0$ and $J = 2-1$ line observations toward the remnant using the SRAO and KOSMA telescopes. These observations reveal a thin molecular cloud elongated along the north-south direction superimposed on the western part of the SNR. The presence of a molecular cloud around the SNR had been known from the previous low-resolution ($30'$) survey, but the relation between the two had not been investigated (Huang & Thaddeus 1986). The spatial correlation of the CO emission with the radio continuum structure together with its high ^{12}CO $J = 2-1/1-0$ line ratio strongly suggests that the cloud is interacting with the SNR. This result also indicates that the distinct radio morphology of 3C434.1 is due to the interaction with a dense, blocking cloud in the west. The systemic velocity of the cloud is -13 km/s,

which yields a new kinematic distance of 3.0 kpc to the SNR. I derived the physical parameters of the SNR based on this new distance. I examined the variation of the radio spectral index over the remnant and found that it was considerably flatter than the other region in the southwestern part, wherein the SNR was interacting with the molecular cloud. I therefore suggest that the distinct radio morphology of 3C434.1 is the remnant of a supernova explosion that occurred just outside the boundary of a relatively thin, blocking cloud in the west.

In final chapter 4, I present a complete catalog of far-IR SNRs in the Milky Way. I have searched the $AKARI$ (65, 90, 140, and 160 μm) and the $Herschel$ (70, 160, 250, and 350 μm) archival data for far-IR counterparts to all 294 known Galactic SNRs (Green 2014) comparing with radio continuum and X-ray data by visual inspection method. In the $AKARI$ and $Herschel$ data, far-IR emissions associated to 59 SNRs out of 294 are identified. Most far-IR SNRs show shell structures, and some also show clumpy or filamentary emission. I derive far-IR fluxes of the detected SNRs and carry out statistical studies of far-IR SNRs. The catalog contained general information of each SNR such as coordinate, angular size, and previous IR results together with $AKARI$ and $Herschel$ fluxes. Using the 24 selected SNRs, I examine the far-IR color-color diagrams and the ratio of far-IR and radio relations. These results show distinct distributions of the young SNRs, old SNRs, and interacting SNRs with MCs. The young SNRs are clearly separated from other SNRs in the color-color diagrams. In case of interacting SNRs with MCs, these are concentrated on the ratio ranges of far-IR to radio fluxes between 1 and 50 with strong far-IR emissions. This systematic and statistic far-IR studies using $AKARI$ and $Herschel$ data are very useful to improve our understanding of the SNR-MC interaction, but more detailed studies for understanding of the mechanism of dust heating process from interacting SNRs with MCs are required.

초 록

항성 진화의 마지막 단계중의 하나인 초신성 폭발은 은하에서 발생하는 매우 격렬한 천체 현상들 중의 하나로써, 성간 물질로의 막대한 에너지 (10^{51} erg) 를 발산하며, 중원소 및 성간 먼지를 제공하는 중요한 역할을 한다. 또한, 초신성 잔해의 진화 및 물리적인 특징은 주변 환경에 의해서 상당한 영향을 받게 되며, 초신성 잔해의 충격파가 분자운을 통과함으로 인해서 분자운을 압축하거나 가속 및 가열하며 심지어 파괴하기도 한다. 또한 충격파의 영향으로 인해 분자운은 화학적 변화를 겪을 수 있으며, 분자운에서 별의 형성을 유발하기도 한다. 본 학위 논문에서는 이러한 초신성 잔해와 분자운과의 상호작용에서 나타나는 특징들을 전파 및 적외선 연구를 통하여 알아보고자 한다.

첫 번째 장에서는 서울전파천문대의 6 미터 전파망원경을 이용하여 우리 은하 내에 알려져 있는 초신성 잔해 11개에 대해 ^{12}CO $J = 1-0$ 분자선 관측 자료를 이용한 연구 결과를 나타내었다. 본 관측 연구는 초신성 잔해 주변의 CO 분자운 서베이의 한 부분으로써 은경 70° 에서 190° 사이에 위치하고 있는 현재까지 알려진 초신성 잔해 중에서 분자운과 상호작용하는 대상을 찾아 연구하는 것을 목적으로 하고 있다. 초신성 잔해에 대한 관측은 각각의 대상들이 연속전파에서 보이는 영역 전체에 대하여 수행하였다. 이 중에서 9개의 초신성 잔해에 대해서는 60″ 간격으로 관측을 수행하였으며, 나머지 대상에 대해서는 120″ 간격으로 관측을 수행하였다. 이 결과 대부분의 초신성 잔해에서 CO 분자운이 분포하고 있음을 확인 할 수 있었으며, 그 중 6개의 초신성 잔해에서는 분자운의 분포가 연속전파의 형태와 공간적인 일치를 보이는 것을 확인 할 수 있었으나, 직접적으로 분자운과 상호작용하는 증거를 찾을 수는 없었다. 이 중에서 두 개의 대상에서 흥미로운 특징을 확인할 수 있었는데, 초신성 잔해 G85.4+0.7 의 경우는 연속전파에서 보이는 구각을 따라 필라멘트 형태의 분자운이 분포하고 있는 것을 확인하였으며, 초신성 잔해 3C434.1 에서는 대상의 서쪽 반구를 막는 듯한 형태를 보이는 거대 분자운이 분포하는 것을 확인할 수 있었다.

두 번째 장에서는 앞선 연구에서 연속전파에서 반구의 형태의 특징을 보이는 초신성 잔해 3C434.1 에 대해 후속 관측 연구를 진행하였다. 이 대상에 대해 서울전파천문대 6 미터 전파망원경을 이용하여 초신성 잔해 전체에 대해서 ^{12}CO $J = 1-0$ 분자선 관측을 수행하였고, 이 결과 초신성 잔해의 서쪽의 약한 연속전파 지역에서 거대 분자운이

분포하고 있음을 확인 할 수 있었다. 이 분자운은 초신성 잔해의 남북을 가로지르고 있으며, 초신성 잔해의 연속전파와의 공간분포가 일치하는 특징을 보여주고 있다. 본 연구에서는 이 분자운에 대해서 KOSMA 3 미터 망원경을 이용하여서 ^{12}CO $J = 2-1$ 분자선 관측을 수행하였으며, 이 분자운에 대한 ^{12}CO $J = 2-1$ 에 대한 ^{12}CO $J = 1-0$ 의 비를 통하여 그 값이 높은 지역을 찾을 수 있었다. 형태학적인 분포와 더불어 높은 비율의 값을 보이는 결과를 통하여 이 초신성 잔해는 분자운과 상호작용하고 있음을 확인할 수 있었다. 또한 이 분자운의 속도 정보를 통하여 (-13 km/s) 초신성 잔해까지의 거리를 3.0 kpc 으로 추정할 수 있었으며, 초신성 잔해에 대한 물리량 등을 정의할 수 있었다. 또한, 연속전파 자료를 이용하여 초신성 잔해에 대한 분광지수의 변화를 통하여 분자운과 상호작용하는 지역에서의 분광지수 값이 다른 지역에 비해 상대적으로 낮은 특징이 있음을 확인할 수 있었다. 이러한 관측 결과를 통하여 초신성 잔해 3C434.1은 상대적으로 얇은 분자운의 경계 밖에서 폭발한 초신성 잔해로 설명할 수 있었으며, 수치계산을 통해서도 초신성 잔해의 비대칭적인 연속전파에서의 형태는 초신성 잔해를 막고 있는 분자운과 상호작용한 결과로 나타남을 확인 할 수 있었다.

세 번째 장에서는 우리 은하내의 초신성 잔해들에 대한 원적외선 자료를 이용한 연구를 수행하였다. 좋은 분해능의 아카리 및 허셸 위성 자료로부터 이전에 연구에서 보지 못했던 초신성 잔해와 관련된 좀 더 구체적인 원적외선 구조를 밝히고자 한다. 본 연구에서는 아카리 및 허셸 자료들을 연속전파 및 X-ray 자료와의 비교를 통하여 지금까지 알려진 294개의 초신성 잔해 중에서 59개의 대상에서 관련된 원적외선 있음을 육안조사를 통하여 확인 할 수 있었다. 초신성 잔해와 연관된 원적외선의 형태는 구각의 형태를 보이거나 덩어리 및 필라멘트의 형태로 나타남을 확인 할 수 있었다. 이러한 원적외선에서 특징을 나타내는 초신성 잔해에 대해서 플럭스 값을 측정하였고 이 대상들에 대한 통계적인 연구를 수행하였다.

주요어: 초신성잔해 – 성간물질: 운동학 및 동역학 – 성간물질: 분자운 – 성간물질: 먼지, 소광 – 전파자료: 성간물질 – 적외선: 성간물질

학 번: 2006-30122